UNIVERSITY OF CALIFORNIA,
IRVINE

Augmented Wireless Telemetry and Powering to Local Area Networks

DISSERTATION

submitted in partial satisfaction of the requirements
for the degree of

DOCTOR OF PHILOSOPHY

in Electrical and Computer Engineering

by

Amirhossein Hajiaghajani

Dissertation Committee:
Assistant Professor Peter Tseng, Chair
Professor Fadi Kurdahi
Professor Michelle Khine
Professor Filippo Capolino

2023

DEDICATION

To

my beloved parents, Hadi and Farzaneh,

and my cherished wife, Fatemeh,

in recognition of their unwavering love and support.

TABLE OF CONTENTS

LIST OF FIGURES

LIST OF TABLES

LIST OF ABBREVIATIONS

BAN: Body area network

WPT: Wireless power transfer

MTM: Metamaterial

MI: Magneto-inductive

SMS: Spoof magnetic skyrmion

NFC: Nearfield communication

BLE: Bluetooth low energy

IoT: Internet of things

RF: Radio frequency

ACKNOWLEDGEMENTS

I would like to express my sincere appreciation to my PhD supervisor, Prof. Peter Tseng, for his exceptional and continuous support throughout my academic journey at UCI. Peter's guidance extended beyond the technical aspects, encompassing logistics and resource management. His understanding and support were central to the progress of my research. He taught me to think beyond the ordinary, and never stop pushing forward when there is a chance to grow.

I also extend my gratitude to my committee members, to Prof. Fadi Kurdahi for providing continued support in UCI CECS; as well as Prof. Michelle Khine and Prof. Filippo Capolino, for their support across cross-functional collaborations.

I also want to extend my thanks to my wonderful mentors, Christopher Magers, director of hardware engineering department at Masimo Corp. and Dr. Jim Weaver, the signal integrity lead at Arista Networks, Inc., along with all the incredibly talented engineers who I have had the privilege to learn from and work with. Their support has given me invaluable chances to learn and tackle practical challenges in industrial internships throughout my PhD studies.

This research was made possible through the faculty startup granted by the University of California, Irvine, and was further supported in part by the National Science Foundation under grant CBET-1928326, as well as the CAREER award ECCS-1942364 received by Prof. Tseng.

VITA

AMIRHOSSEIN HAJIAGHAJANI

Education

PhD	**University of California Irvine,** Electrical and Computer Engineering	2023
MSc	**Iran University of Science and Technology,** Electrical Engineering	2018
BSc	**Iran University of Science and Technology,** Electrical Engineering	2015

Experiences

Graduate Student Researcher, University of California, Irvine	9/2018 – 9/2023
Signal Integrity Intern, Arista Networks	6/2022 – 9/2022
Hardware Intern, Masimo	9/2021 – 6/2022
Hardware Intern, Arista Networks	6/2021 – 9/2021
Hardware Intern, Masimo	9/2019 – 6/2019
Visiting Student Researcher, EMC Lab, KAIST	2/2018 – 6/2018
Graduate Student Researcher, IUST	9/2015 – 6/2018

Highlight Publications

(Full list on Google Scholar)

1. *Amphibious Epidermal Area Networks for Uninterrupted Wireless Data and Power Transfer*
   A Hajiaghajani, P Rwei, AHA Zargari, A Escobar, F Kurdahi, M Khine, P Tseng. **Nature Communications**, 2023.

2. *Textile-integrated Metamaterials for Near-field Multibody Area Networks*
   A Hajiaghajani, AHA Zargari, M Dautta, A Jimenez, F Kurdahi, P Tseng. **Nature Electronics**, 2021.

3. *Microelectronics-Free, Augmented Telemetry from Body-Worn Passive Wireless Sensors*
   A Hajiaghajani, P Tseng. **Advanced Materials Technologies**, 2021.

4. *Selective Manipulation and Trapping of Magnetically Barcoded Materials*
   A Hajiaghajani, A Escobar, M Dautta, P Tseng. **Advanced Materials Interfaces** 6 (24), 2019

5. *Body-conformal Metamaterials for Nearfield Power transmission to Body-IoT Sensor Networks*
   A Hajiaghajani, P Tseng. **Wireless Power Week**, 2022.

6. *Paint-On Epidermal Electronics for On-Demand Sensors and Circuits*
   L Lin, M Dautta, A Hajiaghajani, A R Escobar, P Tseng, M Khine. **Advanced Electronic Materials**, 2020

7. *Ultra-Sensitive Radio Frequency Biosensor at an Exceptional Point of Degeneracy induced by time modulation*
   H Kazemi, A Hajiaghajani, M Nada, M Dautta, M Alshetaiwi, P Tseng, F Capolino. **IEEE Sensors Journal** 2020.

8. *Patterned Magnetic Fields for Remote Steering and Wireless Powering to a Swimming Microrobot*
   A Hajiaghajani, D Kim, A Abdolali, S Ahn. **IEEE/ASME Transactions on Mechatronics** 25 (1), 2019

9. *Electromagnetic Systems for The Selective Manipulation Of Magnetically-Barcoded Materials*
   P Tseng, A Hajiaghajani. **US Patent App. 17/764,753**, 2022

10. *Programmable Multiwavelength Radio Frequency Spectrometry of Chemophysical Environments through an Adaptable Network of Flexible and Environmentally Responsive, Passive Wireless Elements*
    M Dautta, A Hajiaghajani, F Ye, A R Escobar, A Jimenez, K Dia, P Tseng. **Small Science,** 2022

11. *Multiscale, Nano-to Mesostructural Engineering of Silk Biopolymer-Interlayer Biosensors for Continuous Comonitoring of Nutrients in Food*
    M Dautta, KKH Dia, A Hajiaghajani, AR Escobar, M Alshetaiwi, P Tseng. **Advanced Materials Technologies**, 2100666

12. *Single-Sided Near-Field Wireless Power Transfer by A Three-Dimensional Coil Array*
    A Hajiaghajani, S Ahn, **Micromachines** 10 (3), 2019

13. *Magnetic Field Pattern Synthesis and Its Application in Targeted Drug Delivery: Design and Implementation*
    A Hajiaghajani, A Abdolali, **Bioelectromagnetics** 39 (4), 325-338, 2018

14. *Patterning of Subwavelength Magnetic Fields Along a Line by Means of Spatial Spectrum: Design and Implementation*
    A Hajiaghajani, A Abdolali, **IEEE Magnetics Letters** 8 (1), 1-4, 2017

15. *Adaptable Setups for Magnetic Drug Targeting in Human Muscular Arteries: Design and Implementation*
    A Hajiaghajani, S Hashemi, A Abdolali, **Journal of Magnetism and Magnetic Materials** 438, 173–180, 2017

16. *Magnetic Particle Separation by an Optimized Coil: A Graphical User Interface*
    K Rouhi, A Hajiaghajani, A Abdolali, **Journal of Magnetics** 22 (2), 214-219, 2017

Peer Review Service

MDPI Energies	Since 2023
Wiley Bioelectromagnetics	Since 2022
IEEE Access	Since 2020
IEEE Microwave and Wireless Components Letter	Since 2019

ABSTRACT OF THE DISSERTATION

Augmented Wireless Telemetry and Powering to Local Area Networks

by

Amirhossein Hajiaghajani

Doctor of Philosophy in Electrical and Computer Engineering

University of California, Irvine, 2023

Assistant Professor Peter Tseng, Chair

Over recent years, the sensor development has seen remarkable progress, resulting in highly refined analog and/or digital sensors that leave little room for substantial improvements in their core functionalities. In this context, the focus of the wearable electronic community has shifted towards addressing critical challenges, such as minimizing power consumption, optimizing user comfort, and establishing seamless data flow between organic media or living bodies to computer cloud systems. This dissertation contributes significantly to this ongoing paradigm shift. We extend the capabilities of some of the most prevalent wireless power transfer and communication protocols beyond their traditional scope. This body area network (BAN) has been enabled via mechanically flexible magnetic metamaterials that are integrated into user clothing or synthesized as skin patches. These structures possess highly engineered characteristics that allow seamless user experience while monitoring a wide array of chemo-electro-mechanical stimuli in extreme conditions. Our approach delivers uninterrupted, self-powered communication vital for monitoring human status within challenging environments where conventional wireless solutions, such as Bluetooth, Wi-Fi, or cellular networks falter. Notably, this research elaborates extending the scope of these local area networks to

encompass the surrounding environment and peripheral devices beyond the human body, allowing for the smooth wireless data and power transmission across multiple human bodies and untethered smart devices.

1. INTRODUCTION

1.1. Wearable Electronics

Wearable electronics, also known as wearable technology or wearables, refers to electronic devices or technologies that are designed to be worn on the body. These devices are seamlessly integrated into clothing, accessories, or even directly attached to the human body. Wearable electronics have gained significant popularity in recent years due to their potential to enhance our lives in various domains. They offer a wide range of functionalities, including health and fitness tracking, communication, entertainment, and even augmented reality experiences. From smartwatches and fitness bands to smart glasses and embedded sensors, wearable electronics have the capacity to collect and analyze data, provide real-time feedback, and offer personalized experiences. Their portability and continuous connectivity make them an integral part of the rapidly growing field of the internet of things (IoT). As technology advances, the potential applications of wearable electronics continue to expand, holding promise for revolutionizing healthcare, sports, fashion, and many other aspects of our daily lives.

Health monitoring and activity tracking technologies rely on wearable or implantable sensors that link to different regions of the human body (or, in fact, multiple bodies). These sensors can be used to create multi-node networks that interpret information from our bodies and the objects we interact with. In order to parse biometric information in real time, such networks require secure and reliable communication links between nodes [1], [2]. The links are generally known as body area networks (BANs). The robustness of a BAN is dependent on a number of characteristics: the level of comfort (or the size/weight of the device nodes), adaptability to pre-existing clothing, compliance with commonly-used standards [3], node sampling rates, and wireless powering capabilities [4]. It also includes the ability to communicate with nearby BANs and local area networks, creating a seamless connection with a peripheral IoT without compromising security. Ideally, a BAN can offer such communication capabilities while being light weight and battery free (to minimize user burden and facilitate truly continuous monitoring) while being able to sample dynamically-placed wireless nodes at high rates relevant to our unpredictable daily lives (Fig. 1).

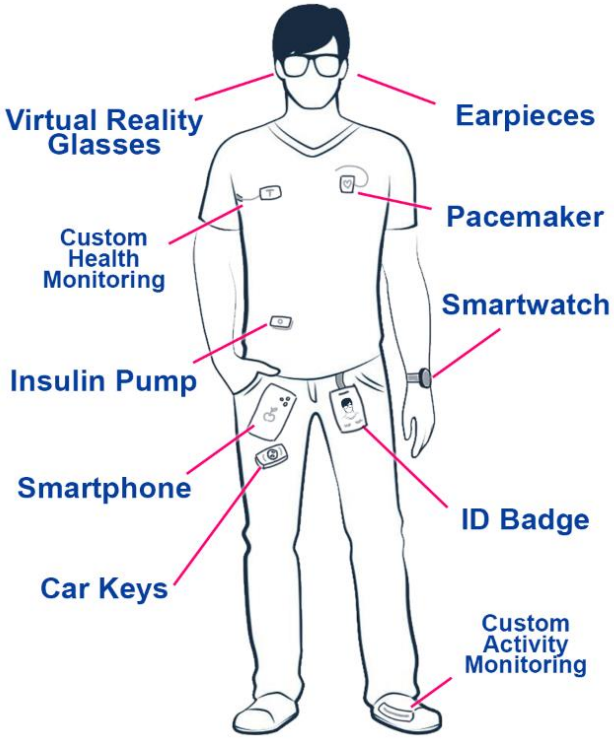

Fig. 1. Distributed wearable electronics.

1.2. Communication in Wearable Devices

BANs have traditionally been equipped with over-the-air communications such as custom radio frequency (RF) transducers [5], RF identification [6], or Bluetooth [7]. However, such radiative approaches often suffer from high power consumption and relatively low levels of security. This is because, despite coding methods, a nearby third-party receiver may listen to the communication between the reader or sensing nodes. This issue can be addressed by limiting the operational range of such communication links to ensure the target receiver/transmitters are placed spatially close enough to the body. One hardware solution to this challenge is to convert/replace the far field radiation unit (such as the planar inverted F-antenna in Bluetooth technology) with a near field antenna [8] and employ surface waves (instead of spatial radiation). This, however, requires exclusively developed Bluetooth sensors as well as a modified reader (often mobile phone) with irregular antennas, which limits wider application. In addition, Bluetooth power transfer is limited and batteries are typically required at sensing nodes to accurately sample the environment.

In wearable communication, several important factors come into play to ensure efficient and effective data transmission. Key considerations include:

a. Speed: Wearable devices often require real-time or near-real-time communication. Fast data transmission speeds enable quick response times and seamless user experiences.
b. Latency: Low latency is crucial, especially for applications like fitness tracking or augmented reality, where timely data updates are essential. Minimizing delay between data capture and its availability for processing or display enhances user satisfaction.
c. Power Consumption: Wearable devices operate on limited battery power. Efficient communication protocols and technologies help optimize power usage, prolonging battery life and reducing the need for frequent recharging.
d. Ease of Use: Wearable communication should be user-friendly and intuitive. Simple pairing processes, automatic connections, and reliable connectivity contribute to a smooth and hassle-free user experience.
e. Durability: Wearable devices are subjected to various physical activities and environmental conditions. Robust communication technologies and components that can withstand impacts, moisture, and temperature fluctuations ensure device longevity and reliability.
f. Cost: Affordability plays a significant role in the widespread adoption of wearable devices. Cost-effective communication solutions allow for wider accessibility, making wearables more accessible to a broader range of users.
g. Compatibility and Interoperability: Wearable devices often interact with other devices or platforms. Compatibility with various operating systems, communication standards, and integration with existing ecosystems enhance versatility and interoperability.
h. Security: As wearable devices handle personal and sensitive data, ensuring robust security measures for data transmission is essential. Encryption, authentication, and secure protocols protect user information and maintain privacy.
i. Scalability: Wearable technologies are evolving rapidly, with potential for expansion and integration into larger networks or ecosystems. Communication systems that can scale and adapt to growing demands and future developments provide flexibility for future enhancements.
j. Signal Strength: Reliable and strong signal strength is necessary to maintain a stable connection between wearable devices and other communication endpoints. This ensures consistent data transmission and minimizes connectivity issues or signal drops.

k. Noise Immunity: Wearable devices are often exposed to various sources of electromagnetic interference or environmental noise. Communication technologies that are resilient to noise interference help maintain clear and uninterrupted data transmission.

1.2.1. Wired data transmission

Wired data transmission involves the transfer of digital information between electronic devices using physical wires or cables. Serial protocols are commonly used in wired data transmission, including the standard serial protocol (RS-232/UART) and other variants such as RS-485 and controller area network (CAN). Two commonly used serial protocols in wired data transmission are I2C (Inter-Integrated Circuit) and SPI (Serial Peripheral Interface).

Traditional sensor area networks have been implemented by daisy-chaining a central controller hub and peripheral sensing nodes through wires to transfer power and data[9], [10]. Robustness of these systems, however, significantly declines by utilizing multiple connectors particularly in moist or underwater environments, which leads to end user discomfort in wearable applications[11]. Difficult network expansion and lack of mobility has restricted the wired platforms to controlled clinical settings[12] (see Fig. 2)

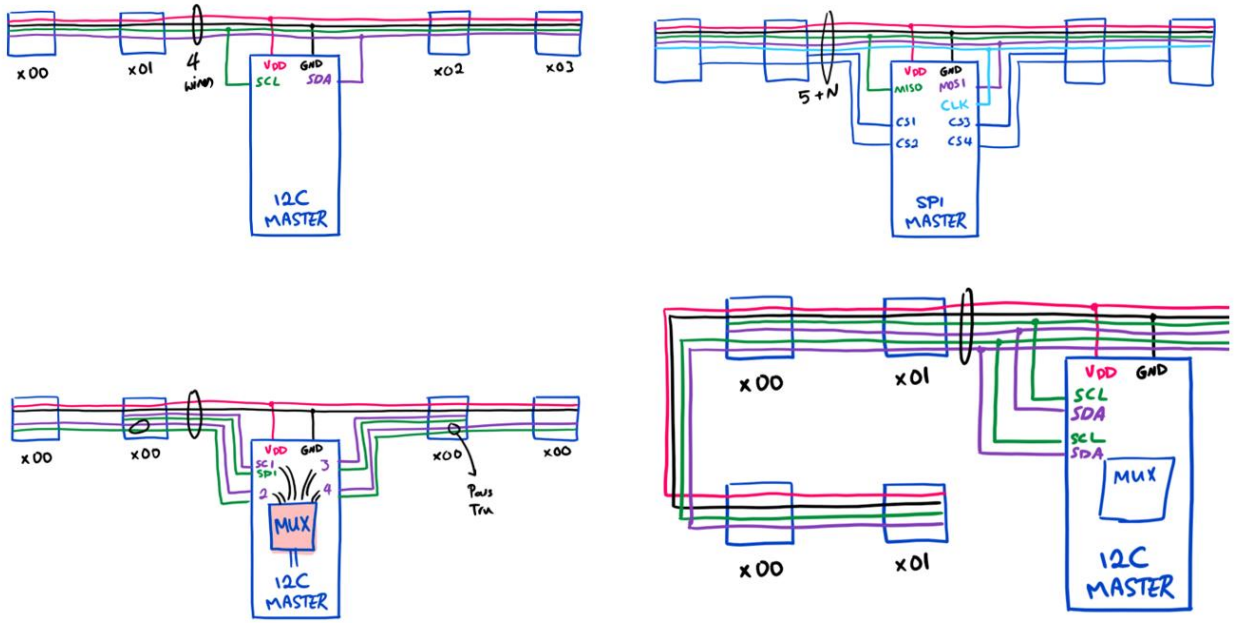

Fig. 2. Wiring architecutres for hardware integration through SPI and I2C protocols.

1.2.2. Wireless data transmission

The far field nature of electromagnetic wave propagation, however, renders these technologies inefficient in extremely humid or underwater settings due to notably low penetration depth at ultra-high frequency radio bands[8], [13], [14]. Alternative wireless solutions include extremely low or high frequency bands which possess high latency, or incompatibility with consumer electronics[15]–[18]. Here we focus on electromagnetic communication.

1.2.2.1. Cellular

Cellular communication in wearables is based on cellular network technology, which allows wearable devices to connect to cellular networks for wireless communication. Cellular networks consist of a network of base stations that provide coverage over a specific geographical area, allowing wearables to establish connections with cellular service providers.

Wearable devices with cellular capabilities contain cellular modem chips and antennas that support specific cellular network technologies, such as 3G, 4G LTE, or 5G. These devices have built-in Subscriber Identity Modules (SIM) or embedded SIM (eSIM) cards that provide identification and authentication on the cellular network.

The cellular communication process begins with the wearable device searching for available cellular networks in the area. The device registers with the cellular network by authenticating its identity using the SIM or eSIM credentials. Once registered, the wearable device is assigned a unique cellular network address.

Data transmission in cellular communication occurs through the exchange of packets between the wearable device and the cellular base stations. These base stations relay the data to the core network, which connects the wearable to other devices or services on the internet. Cellular networks provide wearables with broad coverage, enabling communication in various locations within the cellular network's range.

Cellular communication in wearables offers advantages such as wide-area coverage, mobility, and high-speed data transfer rates. It allows wearables to access internet services, make voice calls, send and receive text messages, and interact with cloud-based applications. Cellular connectivity provides wearables with the capability to operate independently without relying on local Wi-Fi networks or paired devices, offering users continuous connectivity wherever cellular coverage is available.

1.2.2.2. Wireless Fidelity (Wi-Fi)

Wi-Fi communication in wearables is based on the IEEE 802.11 wireless networking standard. It utilizes radio waves in the 2.4 GHz or 5 GHz frequency bands to establish wireless connections between devices. Wearable devices with Wi-Fi capabilities are equipped with Wi-Fi radio modules and antennas, allowing them to connect to local wireless networks and access the internet.

The Wi-Fi communication process begins with the wearable device scanning for available Wi-Fi networks in the vicinity. The device detects and lists the networks based on their Service Set Identifiers (SSIDs) and their respective signal strengths. Once the desired network is selected, the wearable device initiates the authentication and association process.

Authentication involves the exchange of security credentials, such as a password or passphrase, to verify the wearable device's identity and gain access to the network. Once authenticated, the wearable device associates itself with the chosen Wi-Fi network, establishing a secure connection with the network's access point.

Data transmission occurs over the Wi-Fi network using the TCP/IP protocol suite. The wearable device can send and receive data packets over the network, allowing for activities such as web browsing, email synchronization, file transfers, and streaming media. The data packets are encapsulated within the Wi-Fi protocol, ensuring reliable and efficient transmission.

Wi-Fi communication in wearables offers advantages such as high-speed data transfer, broad network coverage, and compatibility with existing Wi-Fi infrastructure. It enables seamless connectivity to the internet, cloud-based services, and other devices within the Wi-Fi network range. Wearables can leverage Wi-Fi capabilities for enhanced functionality, including online content access, firmware updates, and integration with smart home or IoT devices.

1.2.2.3. Bluetooth (BT, or BLE)

Bluetooth communication in wearables is based on the Bluetooth wireless technology standard. It operates in the 2.4 GHz frequency range and utilizes short-range radio waves for wireless data transmission between devices. Wearable devices with Bluetooth capabilities contain a Bluetooth radio module and antenna that allow them to establish connections with other Bluetooth-enabled devices.

Bluetooth employs a master-slave architecture, where one device acts as the master and initiates the connection, while the other device functions as the slave and responds to the master's requests. The Bluetooth communication process involves several stages, including device discovery, pairing, and data transfer.

Device discovery involves the master device scanning for nearby Bluetooth devices and identifying them based on their unique Bluetooth device addresses. Once devices are discovered, the pairing process establishes a secure connection between the wearable device and the target device. Pairing can be done using various methods, including passkey entry, numeric comparison, or Near Field Communication (NFC) for simplified pairing.

Once the devices are paired, they can exchange data wirelessly using Bluetooth profiles and protocols. Wearables can transmit and receive data packets through the Bluetooth radio waves. The data is typically encapsulated using Bluetooth protocols like the Generic Attribute Profile (GATT) or Audio/Video Remote Control Profile (AVRCP), depending on the specific use case.

Bluetooth technology offers advantages such as low power consumption, robustness against interference, and support for multiple Bluetooth devices within a network. It supports different communication modes, including classic Bluetooth for high-throughput applications and Bluetooth Low Energy (BLE) for power-efficient connectivity. Bluetooth communication in wearables enables features like hands-free calling, music streaming, data synchronization, and remote control functionality.

Based on Bluetooth technology, a surface-plasmon-like metamaterial network made out of laser-cut conductive fabrics and attached on clothing with textile adhesive has been recently introduced that enables surface-bound magnetic wave propagation at 2.4 GHz [8], [19], [20]. However, such networks must exhibit continuous conductivity across their entire length scale (otherwise significant transmission loss occurs) and require relatively complex sewing steps onto clothing. The electrical characteristics of these BANs at microwave frequencies also exhibit rather large sensitivity to the presence of tissues. Such BAN architectures with majorly continuous conductivity across the array cannot be readily reconfigured onto pre-existing clothing and suffer from difficult clothing attachment methods, thus limiting their practical utility and making network expansion difficult (user may need wireless sensing nodes in new body areas). Furthermore, the embroidered spoof surface plasmon (SPP) metamaterials are not suitable for below GHz as they would require larger dimensions at lower frequencies (at NFC). Moreover, the enhanced security enabled by redirecting transmitted energy to guided modes (instead of conventional long-range far field radiation) does not allow third-party devices to listen to the Bluetooth communication. This redirection is not often fully efficient, resulting in power leakage at microwave frequencies and ultimately challenging the signal transmission. Although custom Bluetooth antennas with nearfield emission profile are available, they are not currently used in commercial Bluetooth sensors and/or readers and may violate relevant regulation standards. Finally, in such spoof surface plasmon structures the wave propagates on and very close to the surface, and limits propagation from object to object [21] that could occur between pieces of clothing or nearby BANs.

1.2.2.4. Radio Frequency Identification (RFID)

RFID communication in wearables involves the integration of RFID technology into wearable devices, allowing them to interact with RFID tags or readers wirelessly. RFID enables the identification and tracking of objects or individuals through the use of radio waves. In wearables, RFID technology can be used for various applications such as access control, inventory management, contactless payments, and asset tracking. Wearables with RFID capabilities can communicate with RFID tags or readers by exchanging information through radio frequency signals. This allows for quick and efficient data collection, authentication, or identification without the need for physical contact or line-of-sight. RFID communication in wearables offers convenience, speed, and accuracy, enabling seamless interactions in scenarios where quick identification or tracking is required. It enhances efficiency in various industries, streamlines processes, and enhances security by providing reliable and contactless data exchange capabilities.

The use of conductive inks in printed electronics is revolutionizing the integration of information technology into everyday life and advancing IoT applications. These inks offer cost-effective, eco-friendly production and are directly applicable to materials like textiles and paper. They enable the creation of highly conductive devices, such as wireless connectivity antennas, spanning a wide frequency range from MHz to GHz, suitable for wireless data communication and energy harvesting [22], [23], [32], [24]–[31]. Simultaneously, body area sensor networks have been developed for personalized healthcare. These networks combine stretchable on-skin sensors with flexible readout circuits on textiles, addressing compatibility issues. Innovative radiofrequency identification technology increases electronic property tolerance, enabling simultaneous and continuous monitoring of pulse, breath, and body movement for healthcare purposes [6].

1.2.2.5. Near Field Communication (NFC)

Another approach to enhance the BAN security, which does not require alteration from relevant standards, is to use near field emitting devices such as NFC or Qi-based technologies. A single reader can utilize several near field emitting hot spots (that are connected by wire) to transmit signals to often battery-free wireless nodes placed around the body [33]–[36]. An advantage of NFC over the Bluetooth protocol is its plug-and-play ability to pair communication nodes to the reader seamlessly, in addition to supporting wireless power transfer (WPT). This enables pick-and-place characteristics that allow wireless sensing nodes to be switched at will—such capability reduces user burden and has significant convenience in day-to-day use.

With the near field regime, research has focused on connecting a few loop antennas (known as hubs and terminals) using embroidered conductive thread [33], [35] or metal wires [34]. In such structures, the NFC transponders can pair only if placed close to these static hot spots. The wire-linked nature of this approach also makes it unsuitable for on-demand expansion due to long wires used to connect the disparate terminals. Although wireless wearable inter-coil communication has been shown to connect two wristband-like coils [37], it suffers from a short operational range [38], [39]. Similarly, the low-frequency capacitive signaling of human skin and muscle [40] can impede powering of battery-free sensor nodes and may be easily disrupted by or interfere with immediate surroundings (particularly conductive substances).

NFC communication in wearables is based on the principle of electromagnetic induction. NFC operates at 13.56 MHz frequency and uses inductive coupling to establish a short-range wireless communication link between devices. Wearable devices with NFC capabilities contain an NFC chip and antenna, which enable them to act as both an NFC reader and an NFC tag.

In an NFC communication scenario, the wearable device can function as an initiator or a target. As an initiator, the wearable actively generates an RF field to power passive NFC tags or interact with other NFC devices. As a target, the wearable device responds to the RF field generated by an NFC initiator or reader.

NFC enables various modes of communication, including peer-to-peer mode, reader/writer mode, and card emulation mode. In peer-to-peer mode, two NFC-enabled devices can exchange data bidirectionally. Reader/writer mode allows the wearable device to interact with NFC tags, such as accessing data or initiating actions based on the tag's information. Card emulation mode enables the wearable device to simulate an NFC card, allowing it to be used for contactless payments, access control, or ticketing.

The NFC communication process involves the exchange of data packets between devices or NFC tags using protocols such as ISO/IEC 18092 and NFC Data Exchange Format (NDEF). Data transmission occurs by modulating the amplitude and frequency of the RF field. NFC operates in a short-range, typically a few centimeters, providing secure communication as physical proximity is required for successful data exchange.

NFC communication in wearables offers benefits such as fast data transfer, secure pairing, and compatibility with a wide range of NFC-enabled devices and infrastructure. It facilitates convenient and contactless interactions, making wearables suitable for applications such as mobile payments, access control systems, and seamless data exchange between devices.

1.2.2.6. Optical

Optical communication in wearables involves the utilization of light as a medium for data transmission. This technology utilizes optical signals, typically in the form of infrared light, to transfer data between wearable devices or between wearables and external devices.

Wearables equipped with optical communication capabilities incorporate components such as light-emitting diodes (LEDs), photodetectors, and optical transmitters/receivers. These components allow wearables to transmit and receive modulated light signals, enabling data transfer. In an optical communication scenario, wearables emit light signals encoded with data using LEDs. The light signals are then received by photodetectors on the receiving end, which convert the optical signals back into electrical signals for further processing.

Optical communication in wearables offers advantages such as high data transfer rates, low interference, and security. It provides a means for short-range communication between wearables or with optical readers, allowing for applications such as wireless data synchronization, proximity-based data transfer, or authentication. This technology can be found in various wearables, including smartwatches, fitness trackers, and virtual reality headsets. For example, optical heart rate monitors in fitness trackers use optical communication to measure blood flow and monitor heart rate.

Optical communication in wearables is particularly useful in scenarios where radio frequency communication may be impractical or restricted, such as in environments with electromagnetic interference or in applications that require secure and high-bandwidth data transfer.

1.2.2.7. Acoustic and Sonar

Acoustic or sonar communication in wearables involves the use of sound waves for data transmission between devices. It leverages acoustic signals or ultrasonic waves to enable wireless communication and data exchange.

Wearable devices with acoustic or sonar communication capabilities incorporate microphones, speakers, or transducers that can emit and receive sound waves. These components facilitate the transmission and reception of acoustic signals for communication purposes. In an acoustic communication scenario, wearables emit sound waves that are encoded with data. The sound waves propagate through the medium, and other devices or wearables equipped with acoustic or sonar receivers receive and decode the transmitted signals.

Acoustic or sonar communication in wearables offers advantages such as simplicity, low cost, and compatibility with existing audio infrastructure. It can be used for short-range communication between wearables or devices within the vicinity. Applications of acoustic communication in wearables include proximity-based data exchange, wearable-to-wearable communication, and localization or distance measurement.

One example of acoustic communication in wearables is the use of ultrasonic signals for gesture recognition. Wearables equipped with ultrasonic transducers can emit ultrasonic waves and detect their reflections to sense hand movements or gestures. Acoustic communication is especially suitable for scenarios where other wireless communication methods may face interference or limitations. However, it has limitations in terms of data transfer rates and distance compared to technologies like Wi-Fi or cellular communication.

The technology trend in acoustic communication, as highlighted by the provided materials, encompasses innovations in underwater communication for freedivers, wearable acoustic sensors for human-machine interaction, acoustic textiles for biomonitoring, and flexible pressure sensors with various applications. These advancements emphasize the growing importance of acoustic communication in diverse domains, including sports, healthcare, and wearable technology, with a focus on waterproofness, high fidelity, and adaptability to different scenarios [41]–[44].

1.2.3. Hybrid Communication

The hybrid communication can integrate wired and wireless protocols through pieces of wearable microelectronics (see Fig. 3)

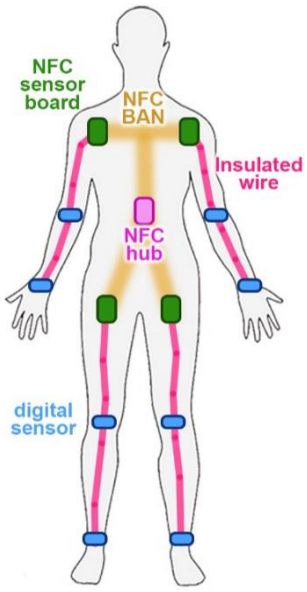

Fig. 3. A hybrid local area network may link microelectronics through various connectivity protocols.

1.3. Powering in Wearable Devices

Powering wearable electronics presents several critical considerations, including the tradeoff between the number of batteries, their biocompatibility, weight, and volume, battery lifetime, and charging cycles. In wearable devices, the choice between using passive power through WPT schemes or incorporating miniature batteries with limited lifetimes and frequent charging requirements depends on the specific application and design constraints. Passive wearables powered through WPT schemes offer the advantage of not requiring onboard batteries, reducing weight and volume, and enhancing biocompatibility, making them more comfortable and unobtrusive for users. However, they rely on external power sources and may have limitations in terms of power transfer efficiency.

On the other hand, wearables equipped with miniature batteries offer greater autonomy and independence from external power sources. Nevertheless, the inclusion of batteries adds weight and volume to the device, and the need for frequent charging cycles becomes a crucial consideration for user convenience. Balancing these factors is essential in developing wearable electronics that can provide optimal performance, comfort, and usability for users in various applications and settings.

Tradeoff between the number of batteries, their biocompatibility, weight and volume, battery lifetime and charging cycles. The wearables may be passive and directly powered through WPT schemes, or incorporate miniature batteries that come with limited lifetime and require frequent charging.

1.3.1. In-situ power generation

In-situ power generation and power harvesting are pivotal aspects of wearable electronics and sensors, offering self-sustainability and prolonged operational capabilities. These techniques harness energy from the wearer's environment, converting it into electrical power for device operation. Common methods include piezoelectric materials that generate electricity from mechanical vibrations, thermoelectric generators utilizing temperature differentials, and photovoltaic cells harvesting solar energy. Additionally, energy can be scavenged from radiofrequency signals in the environment through RF energy harvesting. The integration of these technologies enables wearables to operate continuously without the need for frequent battery replacements, expanding their applications in fields such as health monitoring, environmental sensing, and the IoT [45]–[47].

1.3.2. Wired Power Transmission

In wearable electronic devices, wired power systems are utilized to provide a reliable and continuous power source for various applications. One prominent example of a wired power system in wearable devices is the use of USB connectors for charging and data transfer. These are versatile and widely adopted connector standards that support relatively high power delivery and data rates. In the industrial setting, wearable devices such as smartwatches and activity trackers often incorporate USB ports to facilitate convenient charging and data synchronization with computers. This wired power system ensures that wearables can maintain extended battery life, allowing users to monitor health data, track activities, and receive notifications without the need for frequent battery replacements.

Traditional sensor area networks have been implemented by daisy-chaining a central controller hub and peripheral sensing nodes through wires to transfer power and data[9], [10]. Robustness of these systems, however, significantly declines by utilizing multiple connectors particularly in moist or underwater environments, which leads to end user discomfort in wearable applications[11]. Difficult network expansion and lack of mobility has restricted the wired platforms to controlled clinical settings[12].

1.3.3. Wireless Power Transmission

Importantly, wireless technologies do not support power harvesting for peripheral nodes, leaving wearable electronics reliant on batteries. Despite recent advances in wearable batteries [48], [49] and power scavenging approaches [50], the chemicals utilized in these batteries are often bio-incompatible or exhibit limited lifespan with relatively large form factors. Moreover, increased environment humidity degrades body-coupled capacitive power transfer [40], [51], [52]. These factors often impose critical constraints on sensitive biomedical wearables, especially in terms of requiring continuous power and data transfer in dynamically unpredictable environments. Among widely available wireless technologies, only radio frequency identification and notably NFC feature dedicated power transfer to battery-free peripheral electronics in immediate proximity of the controller [6], [53]. Despite these unique characteristics, utilization of electromagnetic near fields is typically impeded in BANs due to inadequate short range (about a few centimeters) to reach many different human body areas.

There have been recent advances on pushing the NFC range to relatively longer distances (about a few feet) for wearable and/or epidermal solutions, such as embroidering inductor-hubs into clothing [33] or skin patches [54] to direct electromagnetic emission on different body areas. However such inductor-hubs are difficult to integrate to clothing, restrict the wearables placement to dedicated hub location, and impose additional transmission losses [33]. To mitigate these challenges, our team introduced NFC-compliant, textile-integrated magnetic metamaterials with hub-free BAN architecture that connects wearable electronics through discrete pieces of clothing [55]. These solutions, however, utilize conductive threads that exhibit relatively large conduction loss[33], copper sheets which lack in stretchability [55], polymer-encapsulated liquid metal substances that exhibit questionable biocompatibility [54], or metallic nanofibers with difficult synthesis and microelectronic integration (utilizing cleanroom facilities) [53], [56], [57]—these are all challenging for on-skin, epidermal settings. In addition, these solutions generally function in controlled environments and can be easily disturbed in naturally diverse outdoor landscapes. A versatile multi-environment wireless network would be able to offer seamless human interaction with the wearable electronics that are increasingly utilized across health, body-monitoring, and emerging virtual/augmented reality-based technologies.

Communication through body-coupled channels is a transformative concept in wearable technology. It addresses the limitations of conventional wireless power transmission and energy harvesting methods. Unlike near-field or far-field approaches, body-coupled communication leverages the inherent electromagnetic properties of the human body or artificially introduced waves. This innovation drastically reduces power loss due to body shadowing, making it highly efficient. It enables powering devices in various locations around the body, offering self-sustainability and practicality. Whether transmitting power from a distance or scavenging ambient electromagnetic waves, body-coupled communication promises to revolutionize the capabilities of wearable electronics, ensuring they remain operational and accessible in diverse scenarios [45], [52].

1.4. Scope of This Study

We report the development of metamaterial textiles that can be added to pre-existing clothing to create drag-and-drop near field multi-BANs. We use flexible magneto-inductive elements that are tuned to the NFC band [58] and support pick-and-placement of wireless nodes along the network. Inspired by modern low-cost vinyl clothing production, our approach to integrating magneto-inductive networks on textiles eliminates the need for complicated sewing techniques and the relatively expensive conductive threads used to in such methods. This network is designed, built and expanded at will to fit user needs. The magneto-inductive elements are composed of discrete planar and flexible microelectronics-free loops, with spectral behavior that is stabilized against human body effects [3], [59], [60]. They thus create a tunable power/communication path across the human body. This is achieved by bounding the electric fields (which are easily perturbed by the effect of the human body) within the structure internally and utilizing quasi-static magnetic fields. A time-division, multiple access protocol was also implemented to interrogate multiple NFC-enabled sensors connected across the body through discrete pieces of clothing.

Our approach creates a secure on-demand BAN, whose communication link can span across different pieces of clothing, objects, or people. The battery-free and energy harvesting transponders used in the system reduce user burden, allow continuous monitoring, and minimize node size (via battery elimination and memory reduction). The approach could lead to self-sustained, zero-battery BAN ecosystems with cloud assistance [61]–[63].

2. TEXTILE-INTEGRATED METAMATERIAL CHANNELS

2.1. Introduction

Clothing-integrated sensor networks represent a pivotal frontier in wearable technology, offering a multifaceted approach to monitoring physiological data and environmental parameters. These networks, often deployed in smart garments, leverage a range of communication protocols to facilitate seamless data transmission and integration. Notably, Bluetooth Low Energy (BLE) and Zigbee protocols have gained prominence for their energy-efficient and reliable data exchange capabilities. However, these clothing-based sensor networks encounter limitations. They may face challenges related to power efficiency, especially in extended use scenarios, necessitating innovative energy harvesting and management solutions. Additionally, scalability and interference management within dense deployments remain areas of concern. Nonetheless, these networks hold immense promise, ushering in a new era of personalized healthcare, sports analytics, and environmental monitoring, where real-time data collection from integrated sensors offers invaluable insights into human well-being and the surrounding environment. As we delve deeper into this domain, addressing these limitations will be essential to fully unlock the potential of clothing-integrated sensor networks.

Electromagnetic surface wave propagation (often achieved via metamaterials) operating at low frequency bands could potentially be used to create an extendable and wireless BAN at NFC bands. Electromagnetic metamaterials typically function at relatively large frequencies (above GHz) and are fabricated in rigid forms to ensure their perfectly periodic structure.

2.2. Magneto-inductive Metamaterials

Magneto-inductive (also known as magnetic metamaterials) structures have, in particular, been shown to allow wave propagation [64]–[69], enabling a communication path bounded to an array of magnetically coupled resonators (conventionally an array of split rings). Their utility ranges from high frequency metasurfaces applications [70] to WPT [71]–[73]. Due to the magnetically coupled nature of such resonators, and unlike spoof surface plasmon structures, magneto-inductive arrays are wirelessly connected. Magneto-inductive structures with three dimensional coaxial and in-plane magnetically coupled rings also offer some degree of bent powering path [64], [71], [74], [75]. However, they have not previously had enough mechanical flexibility to support the human motion, and are difficult to synthesize and scale to large/curvy structures. Additionally, these structures have not been made compatible with common communication protocols.

2.3. Network Design and Analysis

Magneto-inductive waves propagate through an array of magnetically coupled resonant structures that possess equivalent spectral characteristics as metamaterials. The resonators can be designed in different forms depending on the network's desired characteristics. Traditionally, they are created with rigid loops whose impedance is tuned by lumped elements [76]. In our approach, the requirements of BANs impose a narrow set of constraints on the performance of the magneto-inductive waveguide, as it must exhibit high degrees of flexibility, be insensitive to bodily motion, be easy to extend, and possess a microelectronic-free design. Here, we design multiturn flexible planar coils made of metal (aluminum and/or copper) foils as resonators to be integrated into the clothing textile. The resonance characteristic of such coils, however, depends highly on the undesired parasitic capacitances between the coil and human body. This may interfere with the magneto-inductive wave propagation as the textile integrated network is not fixed on the body and the distance from the skin (d_{skin}) moves slightly during routine activities even on tightly-fitted clothing. To eliminate this effect, the coil is stacked on a ground shield layer to suppress the inductor's electric field from entering the body [77].

This approach adds considerable intrinsic capacitance to the resonator (C_R) and shifts down the resonant frequency, which reduces the loop's length and thus enhances the ohmic loss and self-inductance of the resonator (R_R and L_R, respectively). However, this ground layer is subject to inducing eddy currents due to proximity to the loop traces. To avoid significant loss of the resonator's quality factor, we add several slots on the ground layer perpendicular to the loop traces to terminate the eddy currents (see Fig. 4).

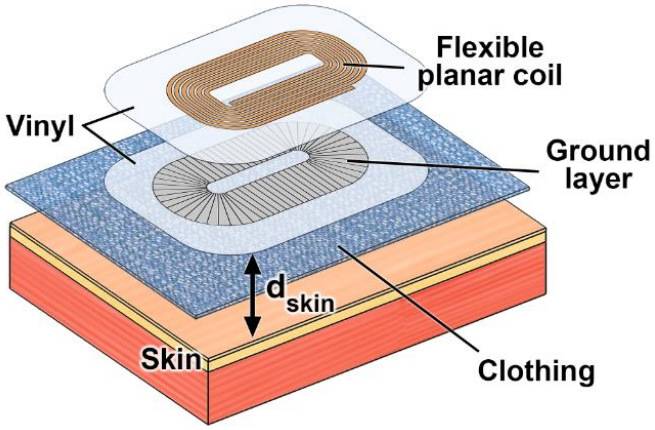

Fig. 4. Design of textile-integrated metamaterials for magneto-inductive wave propagation. Blow up schematic of the flexible, planar magnetic resonator.

This compensates for the power dissipation generated from the flow of image currents on the ground layer. Therefore, the slotted ground layer intervenes in between the loop and skin, eliminates the unpredicted spectral shift of the resonator (Fig. 5), and helps to miniaturize the loop while not significantly affecting the resonator's quality factor compared to when the loop directly put on skin (Fig. 6). As will be shown later, the magnetic field in this scenario is still allowed to flow below and above the resonator despite this ground layer.

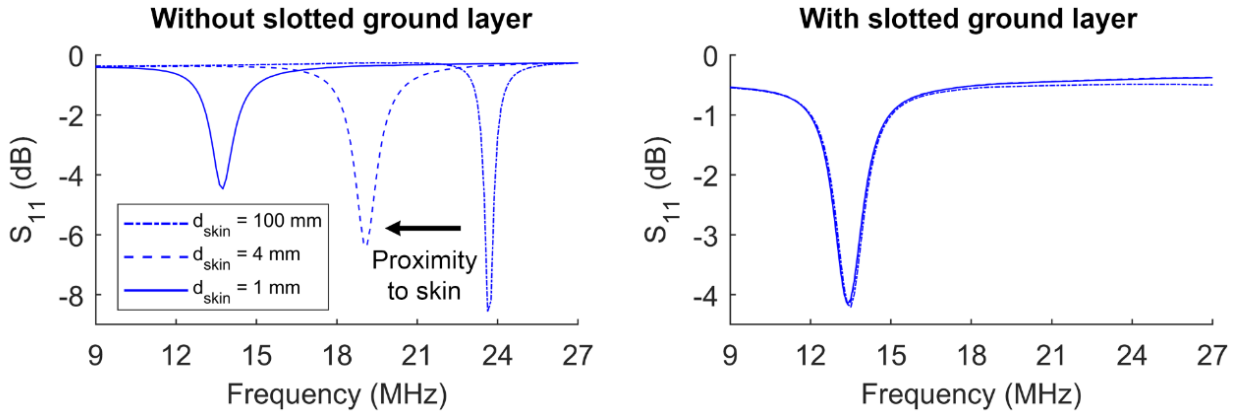

Fig. 5. The ground layer minimizes the spectral uncertainty due to the human body's parasitic effect.

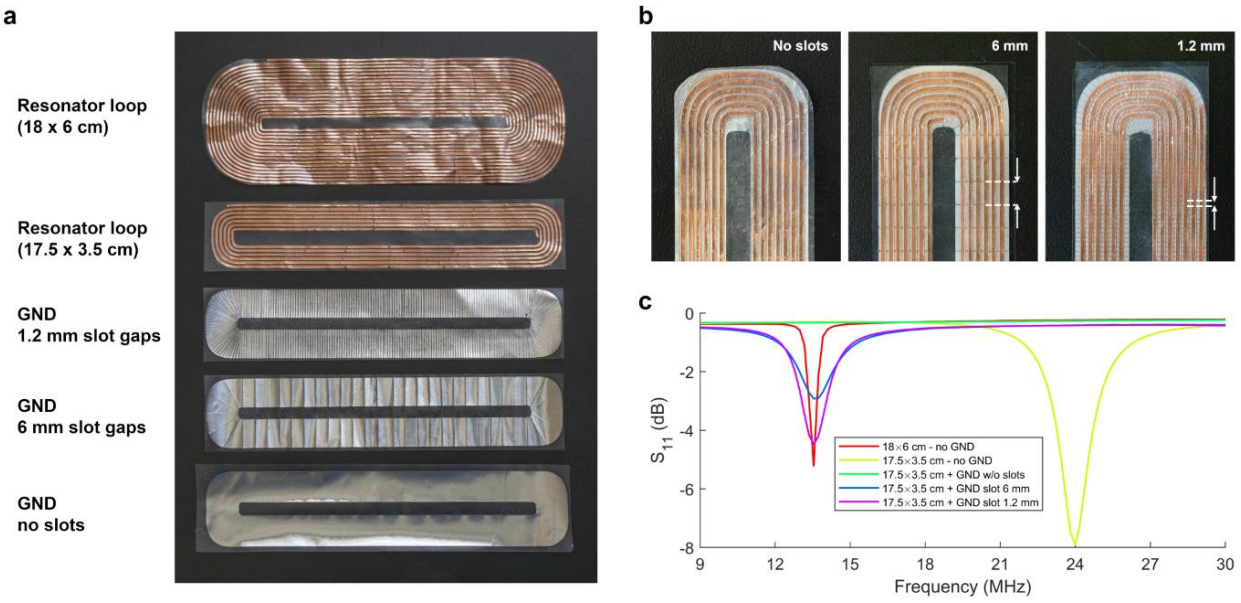

Fig. 6. Ground (GND) layer's slot effect on resonator's spectral properties. (a) A large loop designed to resonate at 13.56 MHz without human's lossy skin effect, and a small loop designed to resonate at the same frequency using the ground layers with various slot distances. (b) The smaller coil integrated with ground layers of different slot gaps. (c) The benchtop measurements of the resonators' spectral characteristics.

The magneto-inductive waves can propagate through more convoluted pathways involving arrays of magnetically coupled resonators (Fig. 7). This magnetic connection allows for more flexibility in terms of the resonators' relative placement and introduces a horizontal distance within our network between the reader and sensor nodes (in x-direction), in addition to the vertical distances (VD) between two neighbor nodes (resonator/device) on different pieces of clothing (or z-axis). This network shows propagation behavior along the coils (x-direction) and typical near field properties in other directions. Thus the nodes (including reader and multiple sensors) in the close vicinity of the coil network would be magnetically connected. The network's equivalent circuit comprised of N coupled coils plus one reader and sensor with a vertical distance in between is shown in Fig. 7.

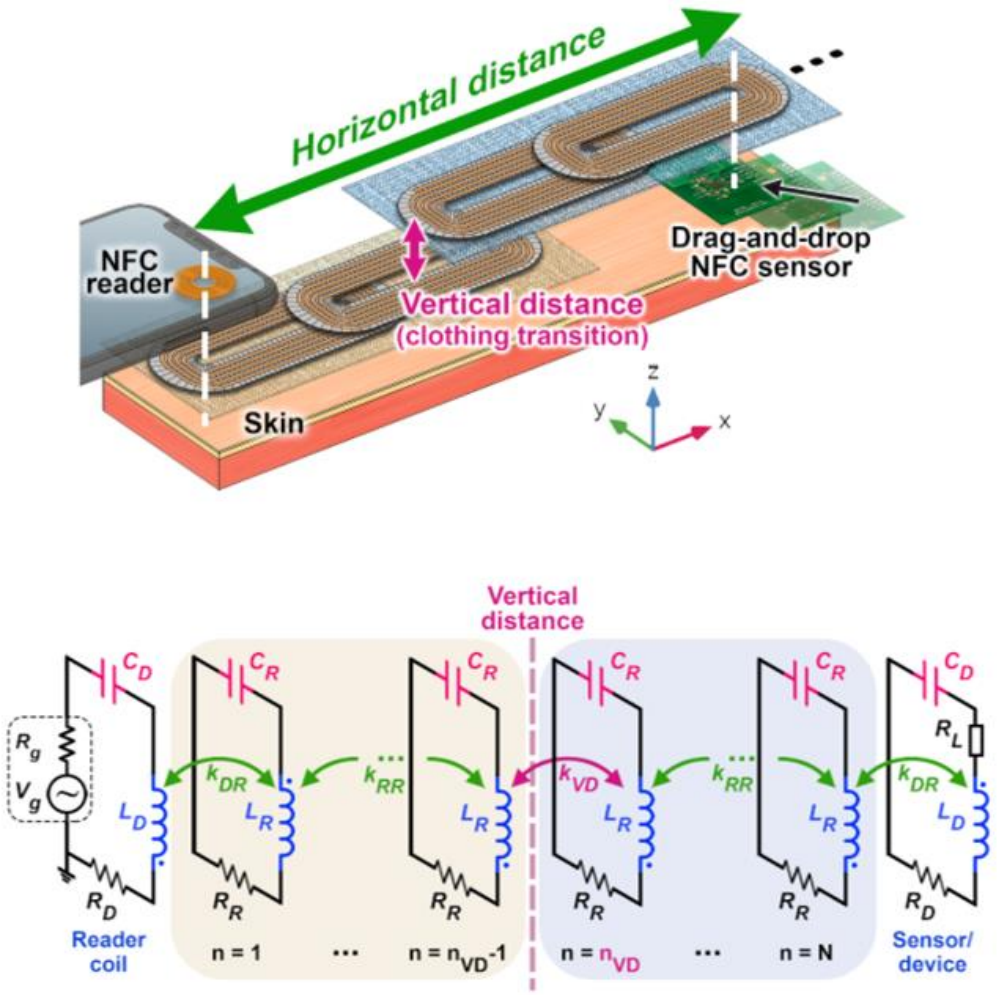

Fig. 7. The NFC sensors can be dragged and dropped across the magnetically coupled resonators with a horizontal distance (in x-direction) and a vertical distance in other directions. Equivalent circuit of the magneto-inductive metamaterial with potential object-to-object transitions.

We assume that the current flowing in the n^{th} resonator has a sinusoidal time-dependency with an angular frequency of ω. Here, the resonator-coils each with an impedance of $Z_R = R_R + j\omega L_R + \frac{1}{j\omega C_R}$, are inductively coupled to their closest neighbor resonator with the mutual coupling of $M_{RR} = k_{RR}L_R$ where M and k represent the mutual inductance and coupling factor respectively (index RR shows inter-resonator relations). The resonators form a linear array with an equal distancing of d_c between two neighbor coils. Here For simplicity, we start by assuming the vertical distance is ignorable ($k_{VD} = k_{RR}$). The current running on the n^{th} resonator (ranging from 1 to N) in a linear array can be represented by:

$$I_n = I_1 e^{j\phi_1} e^{-j\gamma(n-1)d_c} \quad (1)$$

where γ is the travelling wave's propagation constant, I_1 and ϕ_1 are the first loop's current magnitude and phase depending on the excitation (boundary conditions imposed by reader's V_g). The Kirchhoff's voltage law for the n^{th} coil follows:

$$Z_R I_n + j\omega M_{RR}(I_{n-1} + I_{n+1}) = 0 \tag{2}$$

which leads to the dispersion equation:

$$\gamma = \frac{1}{d_c} \times cos^{-1}\left(\frac{-Z_R}{2j\omega M_{RR}}\right) \tag{3}$$

This structure supports forward and backward traveling waves and thus form a standing wave along the resonators array. To match the standing wave's spatial harmonics with the array's geometry, we define $\gamma_m = 4\gamma/m$ where $m\ (>1)$ indicates the number of coils between two spatially equal-phase planes along the standing wave. This enables analyzing the propagation characteristics per unit of resonator (instead of length) and would be ultimately helpful to identify the resonator number on which the standing wave's peak places. The per-resonator expression of the spatial harmonics facilitates the network's design for the end user to plan the number of resonators on each piece of clothing and thus optimize the BAN (see Fig. 8).

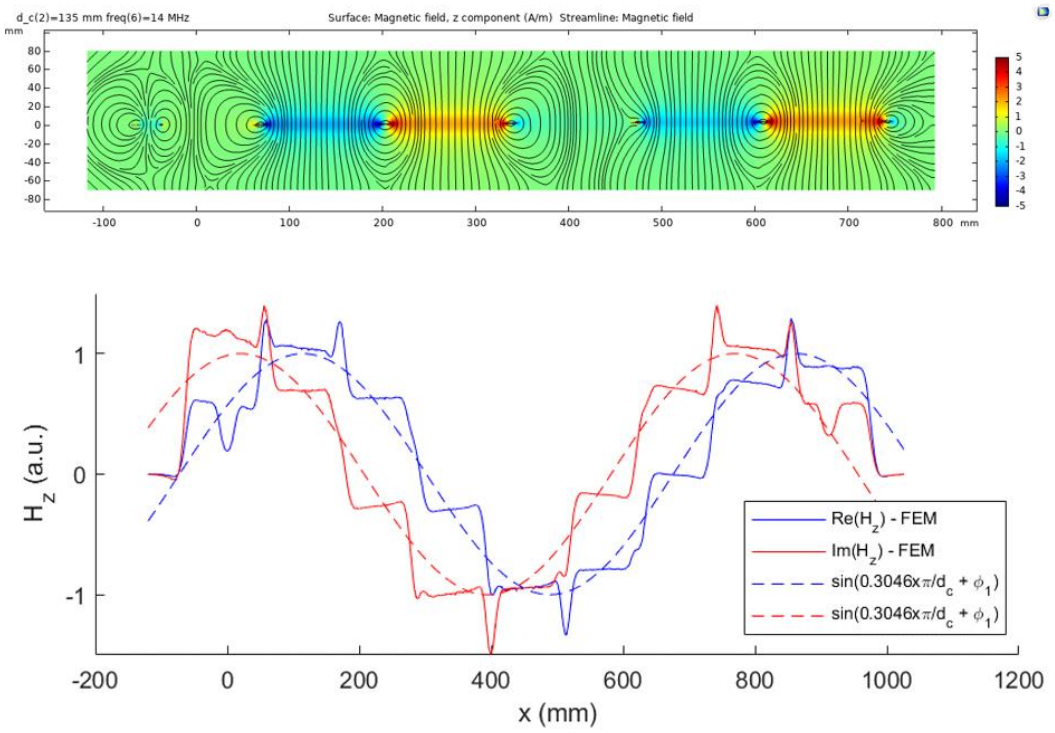

Fig. 8. FEM Simulation of electric field norm in immediate proximity of the array surface. Perpendicular magnetic field to the surface of discrete MI arrays.

Here, $\gamma_m = \beta - j\alpha$ is the harmonic propagation constant (β as the phase and α as attenuation constants) and is calculated for our typical resonator properties and shown in Fig. 9.

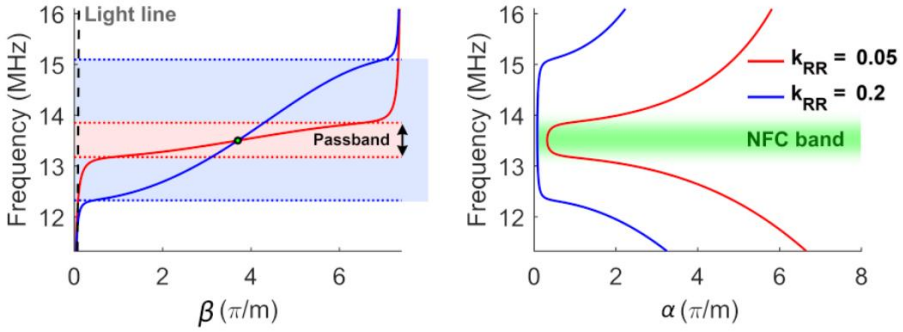

Fig. 9. The dispersion diagram for the array of resonators for various magnetic coupling coefficients. The lower and higher cutoff frequencies (magneto-inductive wave passband) are marked by dotted lines and specify the bandwidth. The light line (with a large slope of the light velocity in free space) is shown by dashed line.

The propagation constant profile $\beta(\omega)$ may possess different values depending on the coil geometry (reflected in Z_R), coupling factor, and harmonic modes (m, which is not necessarily an integer). Dispersion profiles for various modes and electrical properties are compared in Fig. 10**,** Fig. 11, and Fig. 12.

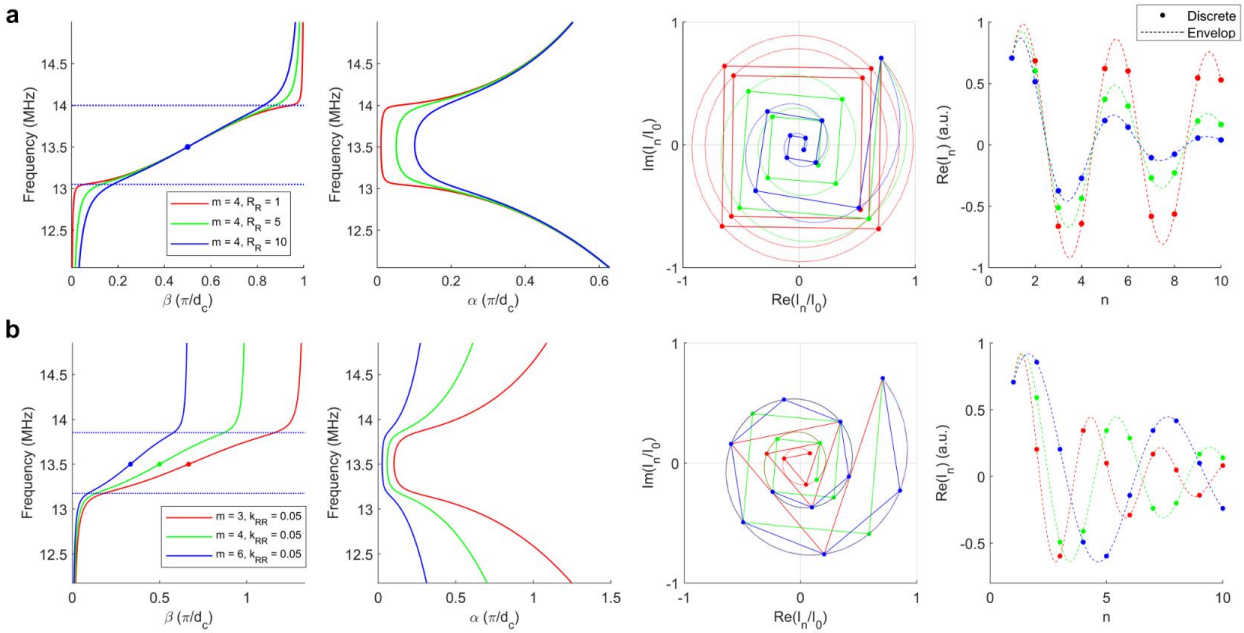

Fig. 10. Effect of resonator's electrical properties on the wave propagation. (a) Larger ohmic loss increases the attenuation (plots generated for K_{err}=0.07). (b) Comparison of various standing wave modes which depend on the network's boundary condition and/or number of elements including resonators, reader, and sensors (plots generated for R_R=3).

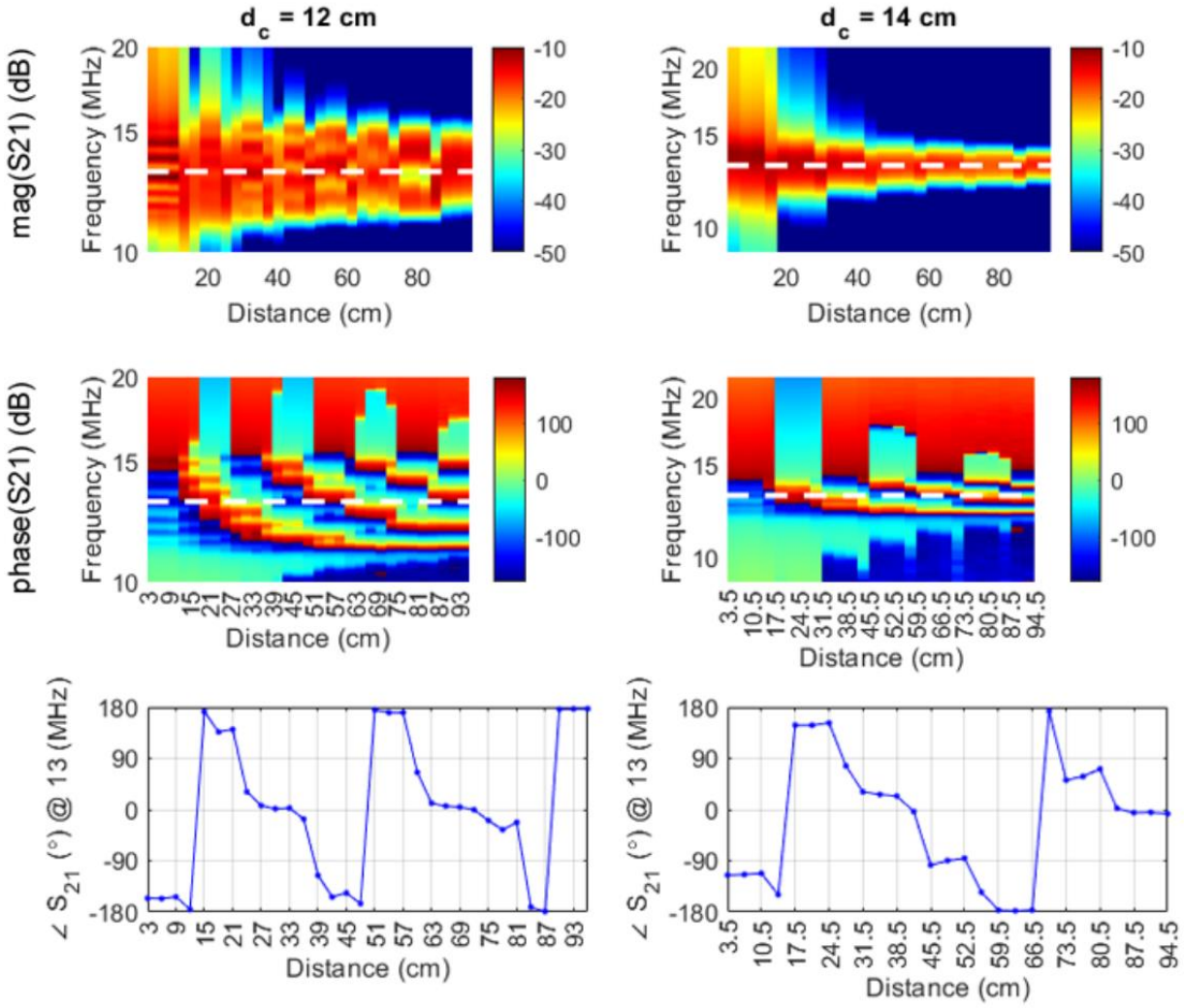

Fig. 11. Measured transmission magnitude and phase characteristics of an MI linear array.

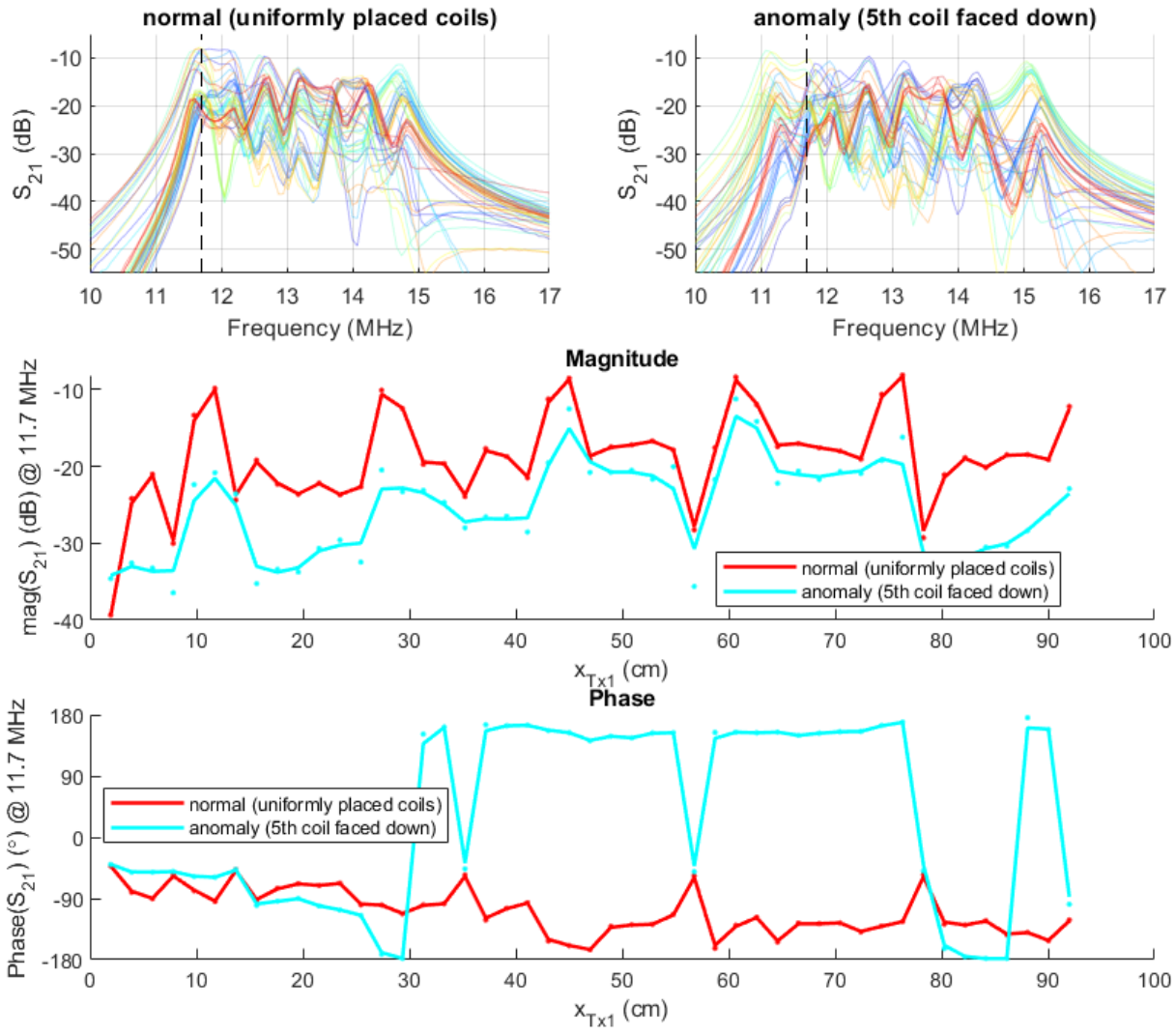

Fig. 12. Rotating a coil (at 30cm) results in transmission profile phase shift of 180 degrees.

We designed and tuned the coils to resonate at NFC's standard frequency (13.56 MHz) as shown in Fig. 13. To afford enough bandwidth for the amplitude shift keying utilized in NFC protocols, the auxiliary carriers (distanced 848 kHz from the main carrier at 13.56 MHz) must be covered by the metamaterial's passband.

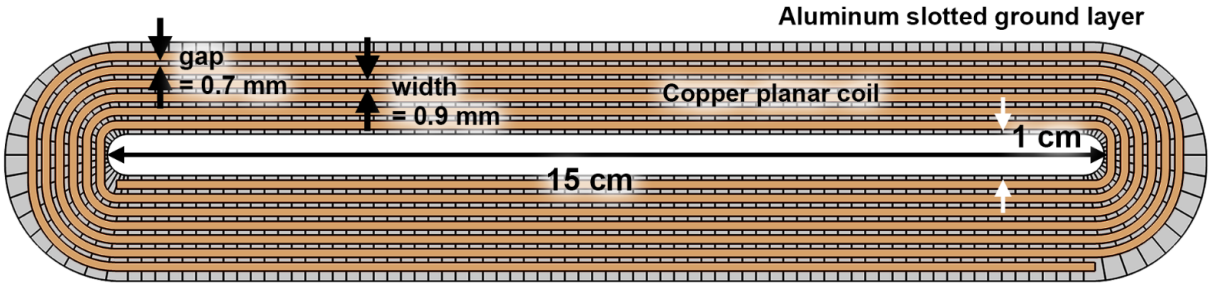

Fig. 13. Coil geometry and the background partial ground.

As shown in Fig. 9, this may be tuned by the inter-resonator coupling (k_{RR}) or equivalently the neighbor coil distancing (d_c). The passband calculations obtained from the dispersion diagrams show that a k_{RR} value of 0.1 is capable of providing sufficient bandwidth for successful long-term communication under varying mechanical distress. This is approximately equivalent to less than 20% neighbor coil overlap (3.2 cm for our typical rectangular loop that possesses a length of 17 cm).

Unlike traditional BANs that utilize coils connected by wire, here, the inter-resonator magnetic coupling enables complex network architectures with user-friendly extensions such as inline or fork connections (Fig. 14). When integrated into clothing, it allows for the BAN's complex signal paths to span across multiple layers of disconnected clothing (e.g. from pants to shirts), distinguishing itself from other textile-BANs that rely on a wire- or conductive thread-based connection.

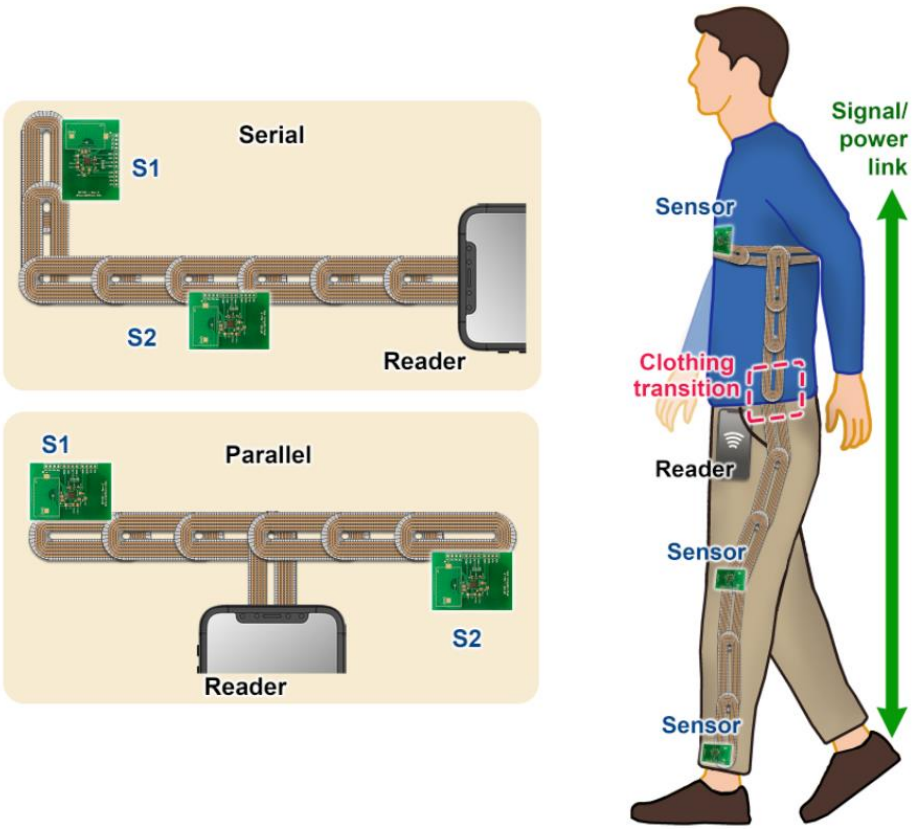

Fig. 14. The reader and multiple sensors can be utilized in an in-line serial or T-shaped parallel array of resonators to form various signal paths around the body. The metamaterial network is easily streamlined into separate clothing pieces, enabling high flexibility necessary for daily routines and significant horizontal range extension. The nodes may be placed anywhere close to (within a few centimeters of) any point of the network.

The VD's effect can be evaluated using the circuit theory to calculate the efficiency of the network (see Fig. 15 for deriving the equivalent circuit of the resonator chain).

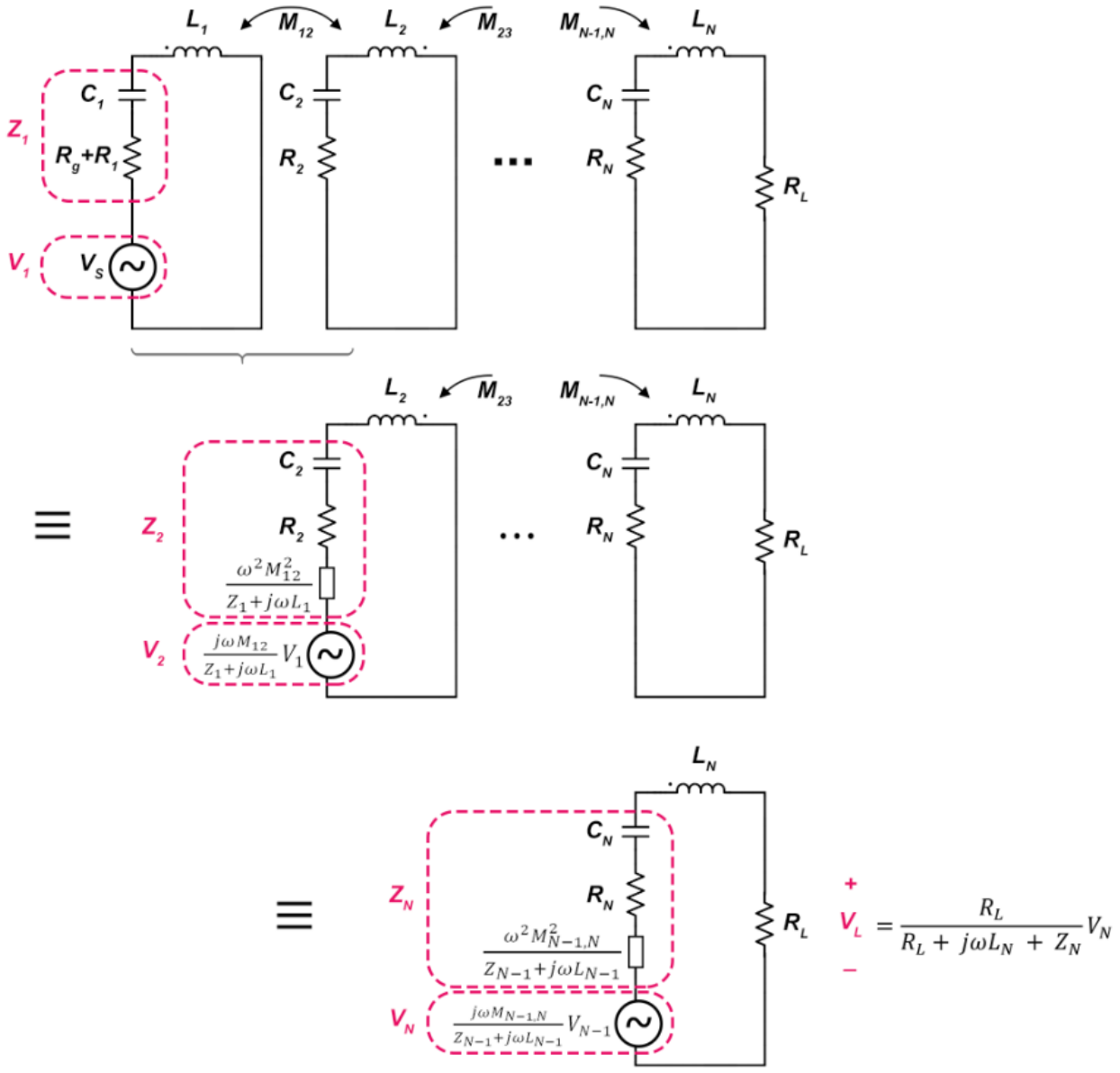

Fig. 15. Deriving the equivalent circuit of the coil array using Thevenin's equivalent circuit. The mutual inductances may take different values depending on if there is a vertical distance along the chain.

First, the transmission (S_{21}) profile of a network (with N=11) without VD is shown in Fig. 16 where the reader (Tx) and sensor (Rx) at the ends of the inline resonator chain are connected to the first and second ports, respectively. For large enough k_{RR} values, the peak S_{21} (originally centered at 13.56 MHz) splits into N resonances, correlating to the metamaterial passband. This aligns with what is referred to as the strong coupling of magnetic resonances in the literature. Adding a VD with the coupling factor of k_{VD} at the 6th resonator (middle of the chain) affects the transmission at the central frequency (Fig. 16).

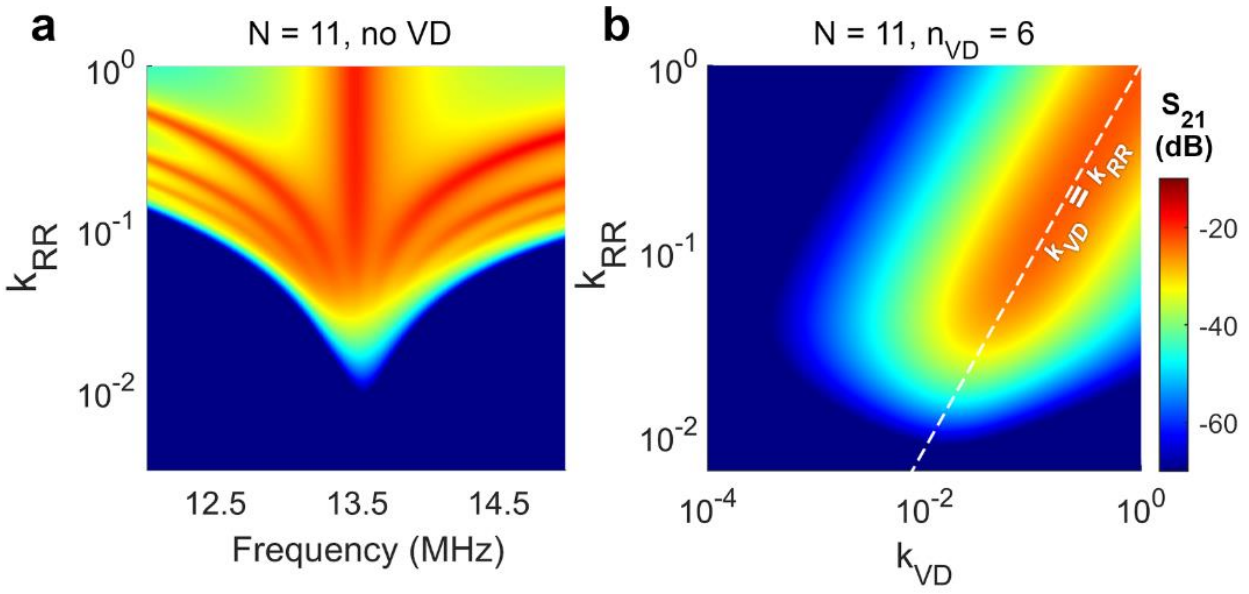

Fig. 16. Wave propagation along complex pathways of magnetic metamaterials. (a) The transmission profile of an inline network of resonators for varying inter-coil coupling (coil distancing). (b) The transmission profile for inter-coil (horizontal) coupling versus a coupling anomaly generated by a vertical distance (VD) in the middle of the network.

It is shown, however, that the network demonstrates peak transmission performance when $k_{VD} = k_{RR}$. To operate close to this constraint, one may compensate for the low k_{VD} (due to the z-axis distance) by increasing the coil overlap (along the x-axis). The S_{21} profile comparison for various VD placements, and modulating VD compensation is shown in Fig. 17.

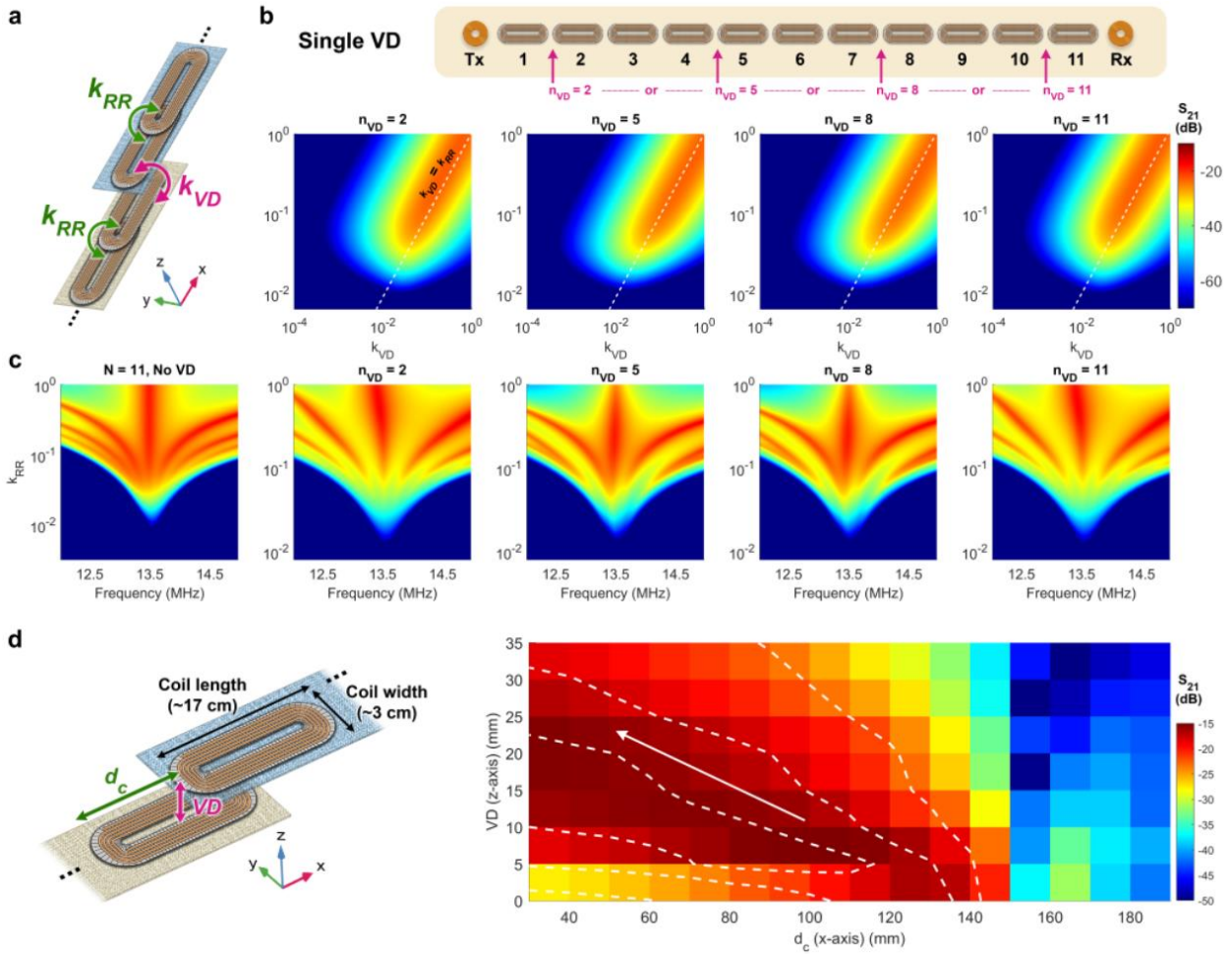

Fig. 17. Supplementary Fig. 5. Effect of a single vertical discontinuity (VD) made by clothing transition. (a) The coupling anomaly along the network. (b) The transmission coefficient (S_{21}) versus inter-relay and vertically distanced coupling factors. (c) Coupling factor profile versus frequency for an inline network of 11 elements. (d) Benchtop transmission measurement (at 13.56 MHz) showing the VD (in z-axis) can be compensated by reducing the neighbor coil distancing (increasing overlap in x-axis) to maintain the same level of transmission (contours are shown by dashed lines). Cellulose sheets were used as a variable z-axis spacer to mimic the intervening clothing.

Due to the reciprocal nature of the magneto-inductive array, various (single or multiple) VD placements along an inline network may possess similar transmission profiles (Fig. 18). This ultimately simplifies spectral optimization and minimizes design rules by enabling planning of resonator placements prior to integration into the clothing.

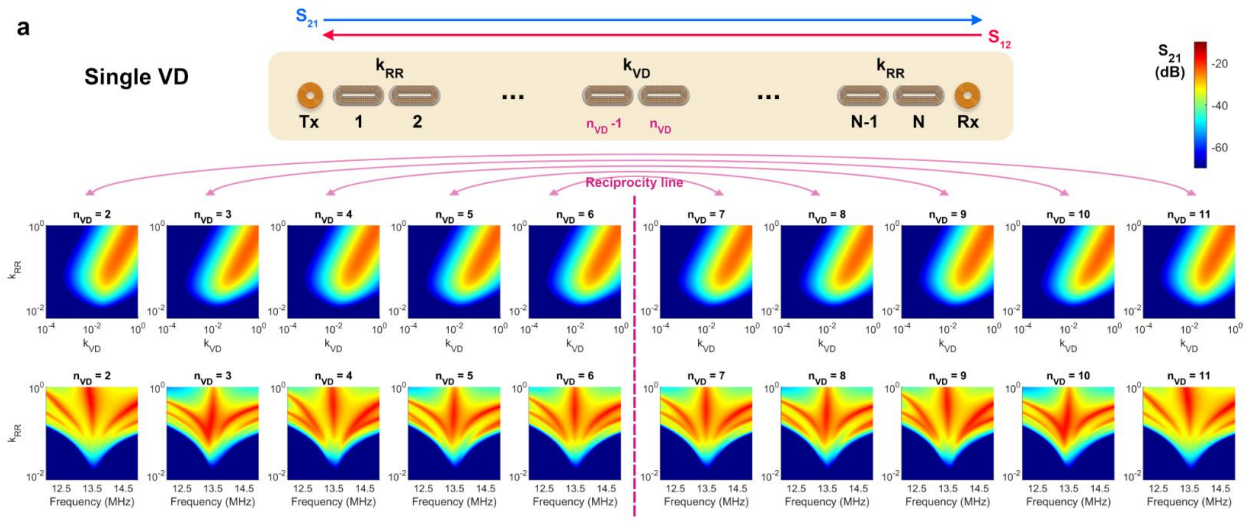

Fig. 18. System reciprocity for single and two vertical discontinuities. Due to the inline network's theoretical reciprocity, certain coupling profiles such as n_{VD} =(2,11) and (5,8) with similar VD placements from either end of the linear array are identical (here N=11).

According to the benchtop measurement of the inline array of resonators (Fig. 19) with a fixed Tx and a moving Rx, larger k_{RR} (or smaller d_c) results in enhanced horizontal range, but meanwhile, S_{21} peak splits (as in Fig. 16) and ends up with non-monotonic S_{21} fluctuations along the network.

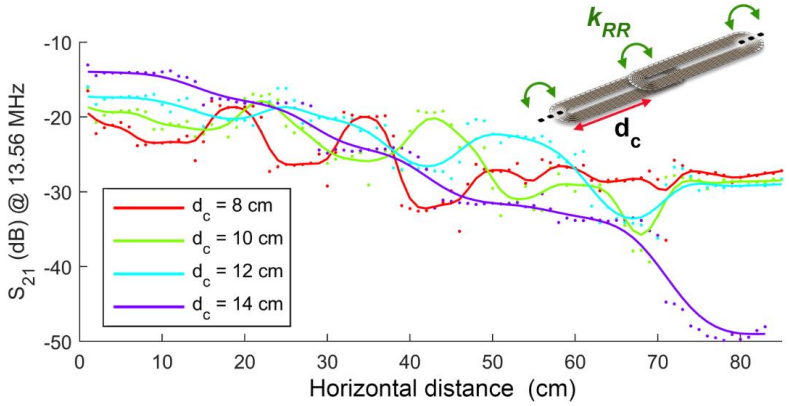

Fig. 19. The experimentally measured $|S_{21}|$ over an inline array of resonators for various coil distancings (without VD), demonstrating the artificially-created standing wave along the magneto-inductive waveguide.

The fluctuations agree well with the envelop of the I_n profile (shown in Fig. 20) and shows standing wave formation. In addition, the wideband spectrum of the transmission (depicted in Fig. 20) demonstrates the ability to optimize the metamaterial's bandwidth. Additionally, small d_c requires a larger number of coils per unit of length, eventually increasing the loss at the coil transitions. Although long coils decrease the number of transitions, on the other hand, it reduces the number of turns in each coil (to maintain the same resonance frequency) and lowers L_R and k_{RR}, which is not ideal.

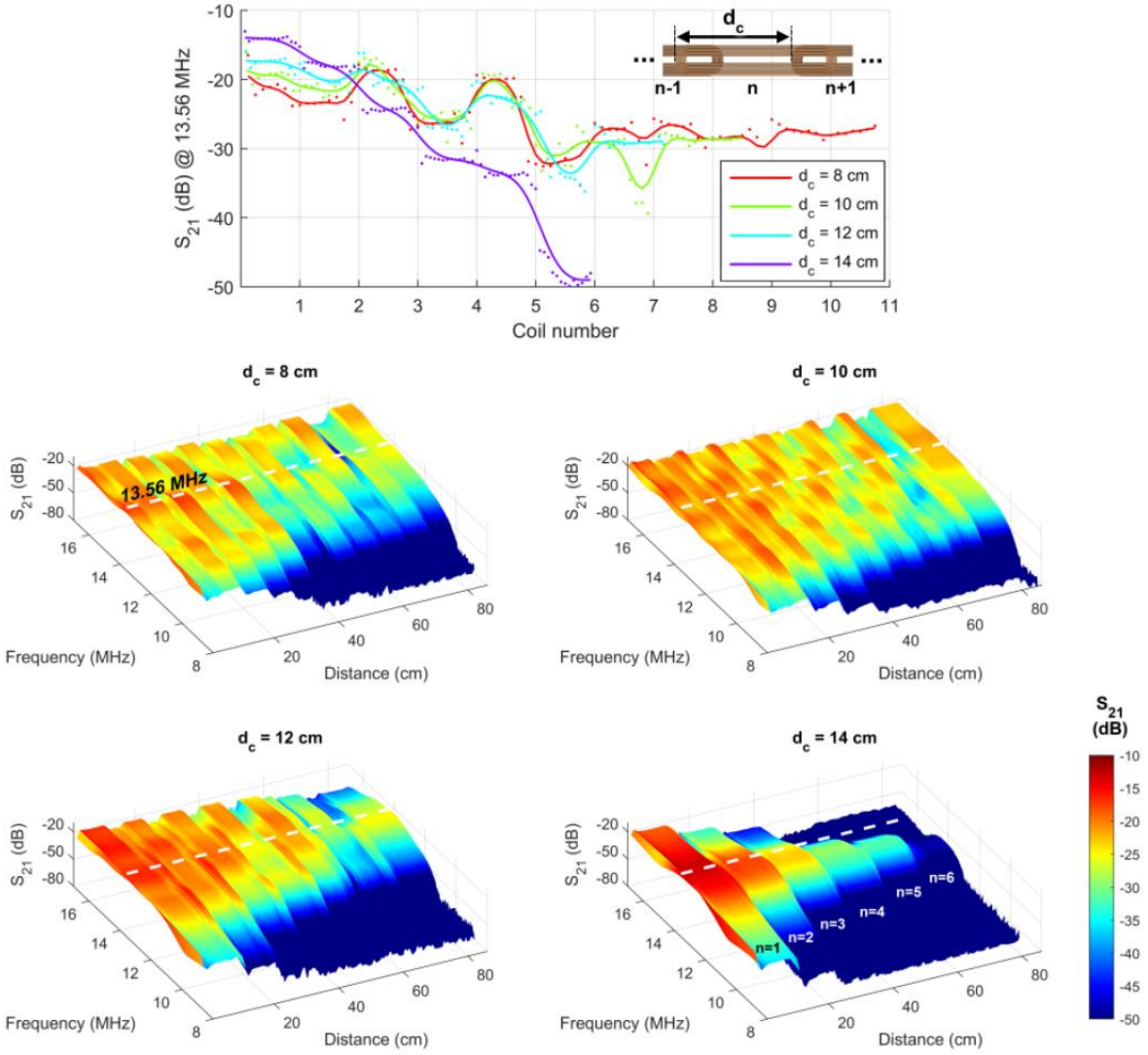

Fig. 20. The ex vivo transmission per element and versus Tx/Rx distance obtained from an I-shaped network.

The magnetic field profile simulation in an inline array (with a test VD in the middle) is implemented by the finite element method (Fig. 21) and demonstrates the standing wave formation and the feasibility of our method for clothing transitions.

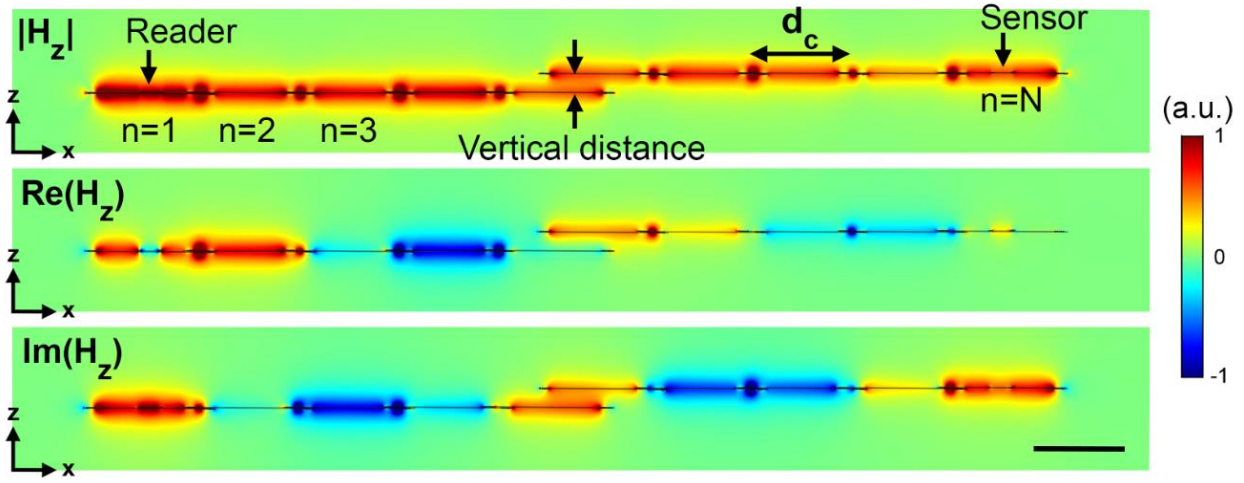

Fig. 21. Side view of the magnetic field's distribution showing the standing wave (at $\beta d_c \approx \pi/2$) along the inline resonator path with 2 cm of vertical distance in between (scalebar 10 cm).

Powerfully, the approach of magnetically coupled resonators offers in-plane coil rotation (in addition to bending), enabling the creation of various pathway styles including a meandered 'S-shaped' network (Fig. 22). This allows the magneto-inductive waveguide/network to pass through various points on the human body for sensing purposes. The open-ended network may be generalized to a closed-loop and allows for reduction of the total number of resonators in the BAN, although it may enforce additional boundary conditions on the network's dispersion and suppress some modes. This concept can be robustly expanded where a pathway branches off from the main signal path (see Fig. 22).

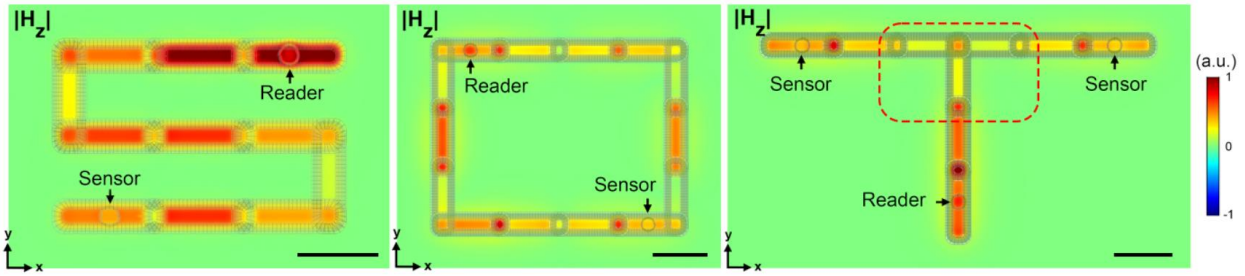

Fig. 22. Top view of the magnetic field of a meandered S-shaped, circular, and branched T-shaped pathways.

Each of the branches can be analyzed separately by considering that their first element's current is identical to the main pathway's last element. The experimental transmission profiles of closed-loop and branched network architectures (operating as an magneto-inductive power divider) are quantitatively compared to the straight, undivided pathway. This, in addition to the electrical measurements and simulation of various resonators are illustrated in Fig. 23.

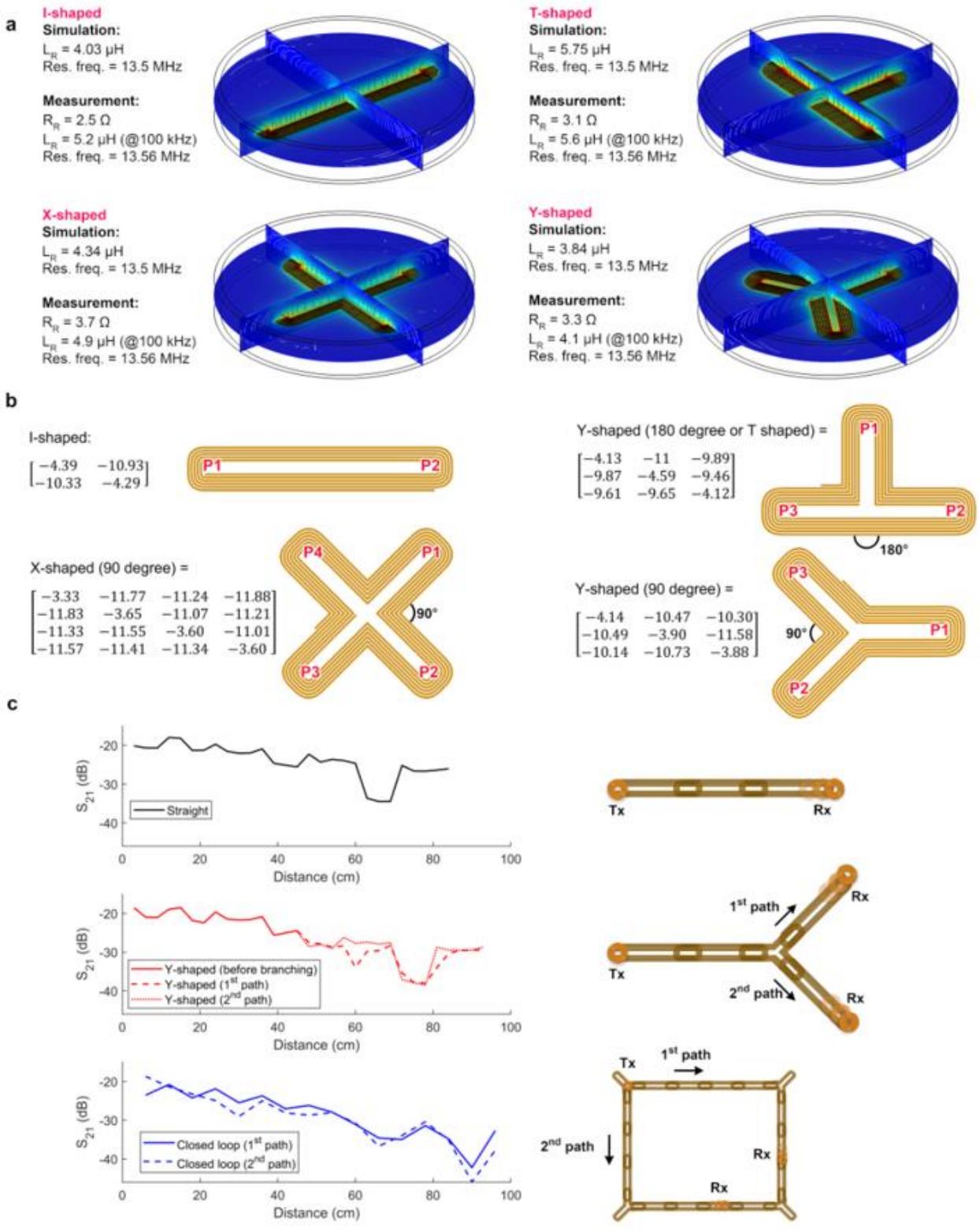
a
I-shaped
Simulation:
L_R = 4.03 μH
Res. freq. = 13.5 MHz
Measurement:
R_R = 2.5 Ω
L_R = 5.2 μH (@100 kHz)
Res. freq. = 13.56 MHz
T-shaped
Simulation:
L_R = 5.75 μH
Res. freq. = 13.5 MHz
Measurement:
R_R = 3.1 Ω
L_R = 5.6 μH (@100 kHz)
Res. freq. = 13.56 MHz
X-shaped
Simulation:
L_R = 4.34 μH
Res. freq. = 13.5 MHz
Measurement:
R_R = 3.7 Ω
L_R = 4.9 μH (@100 kHz)
Res. freq. = 13.56 MHz
Y-shaped
Simulation:
L_R = 3.84 μH
Res. freq. = 13.5 MHz
Measurement:
R_R = 3.3 Ω
L_R = 4.1 μH (@100 kHz)
Res. freq. = 13.56 MHz
b
I-shaped:
[−4.39 −10.93; −10.33 −4.29]
P1
P2
X-shaped (90 degree) =
[−3.33 −11.77 −11.24 −11.88; −11.83 −3.65 −11.07 −11.21; −11.33 −11.55 −3.60 −11.01; −11.57 −11.41 −11.34 −3.60]
P4
P1
90°
P3
P2
Y-shaped (180 degree or T shaped) =
[−4.13 −11 −9.89; −9.87 −4.59 −9.46; −9.61 −9.65 −4.12]
P1
P3
P2
180°
Y-shaped (90 degree) =
[−4.14 −10.47 −10.30; −10.49 −3.90 −11.58; −10.14 −10.73 −3.88]
P3
90°
P1
P2
c
S_{21} (dB)
Straight
Distance (cm)
Y-shaped (before branching)
Y-shaped (1st path)
Y-shaped (2nd path)
Closed loop (1st path)
Closed loop (2nd path)
Tx
Rx
1st path
2nd path

Fig. 23. Benchtop measured and simulated spectral characteristics of the magneto-inductive elements all resonating at 13.56 MHz with various architectures. (a) Electrical characterization by FEM simulation and measurements for various grounded resonators along with the magnetic field intensity profile. Due to the distributed and fringing capacitances, the equivalent capacitance of each structure can be calculated from the self-inductance and resonance frequency (coils resonate at 13.56 MHz). Measurement values were substituted in the circuit model. (b) Experimentally measured S-parameter matrixes (at 13.56 MHz) for resonators as waveguides and/or power splitters (ground layer is not shown). (c) Experimentally measured transmission profile comparison for straight, branched, and closed-loop architectures. The S-parameters here include the loss caused by the reader loop antenna's mutual coupling with the resonator ports (each reader antenna imposes about 2 dB of loss), thus the actual transmissions (S_{ij}) are larger about 4 dB (we did not compensate for this to ensure the VNA's calibration accuracy).

The magnetic profiles are simulated for various modes (induced by variant coil distancings) and shown in Fig. 24.

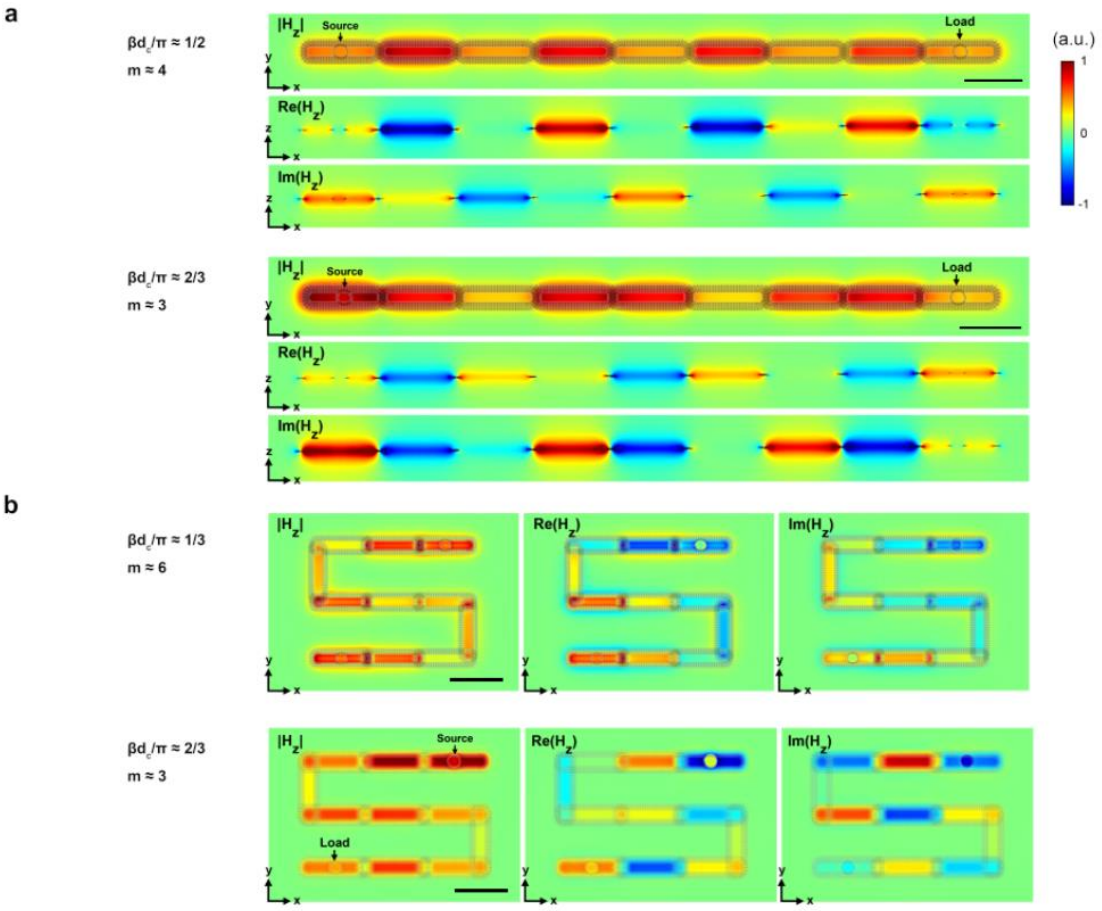

Fig. 24. Magnetic field profiles were obtained by finite element simulations for various standing wave propagation modes. (a) Inline and (b) meandered architectures. Here, m represents the number of coils inducing a phase shift of 2π on the standing wave (scalebar 10 cm). These profiles show the magnetic field flowing on top and underneath the coils despite utilizing the ground layer (as it only suppresses the electric field between the coil and skin), meaning that the reader and/or sensors may be placed on top of or underneath the clothing where the network is integrated. This has some interesting downstream benefits, as this effectively reduces the amount of RF energy that would be absorbed by the body (living systems interact primarily with electric and not magnetic fields). This means that in principle these networks can support the transmission of exceptionally high power (well-beyond the body-safe power range of NFC) close to the human body while minimizing its absorption of electric field energy.

To reduce the number of resonant elements, enhance the transmission, and achieve higher mechanical flexibility at the network's branched sections, we merged the intersection coils (e.g. three coils at the T-shaped junction) into one multi-ended coil. This noticeably reduces the system loss (created in majority by inter-resonators' coupling loss). The reader/network mutual coupling and resonator's ohmic loss, however, yet exist but in lower orders compared to the interconnection attenuations (Fig. 25).

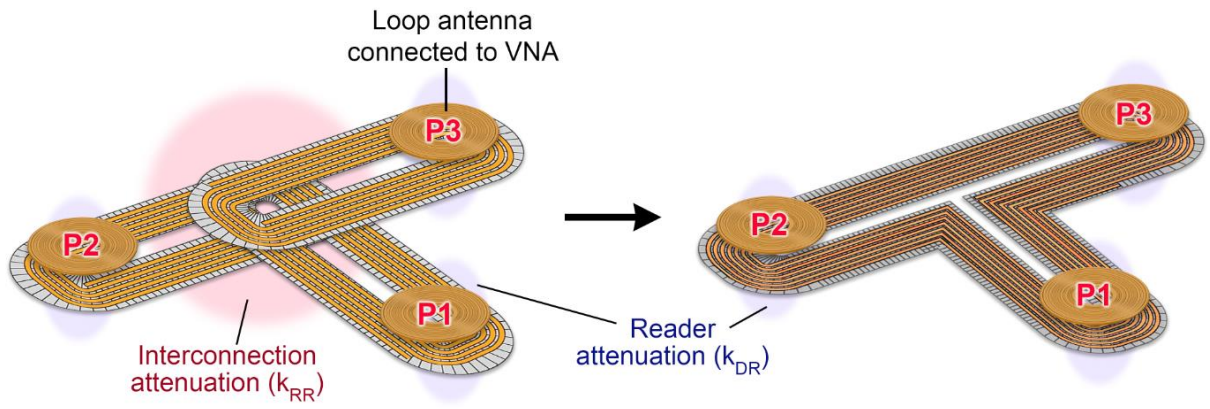

Fig. 25. Multiple coils sharing the intersection can be merged into one piece to lower the system loss by reducing the number of interconnections, thus enhancing the transmission profile.

2.4. Clothing Integration and Multi-sensor Studies

An ideally-functional BAN should be adaptable to pre-existing clothing and readily expand to desired body areas based on the user's needs. These should possess a mix-and-match feature in terms of positioning of the network and multiple sensors. Additionally, their functionality should not be limited to only a few hot spots on which the reader/sensor can be placed. Conventional textile-BANs, however, usually use conductive thread sewed on the clothing and are not particularly affordable or easy to fabricate. In addition these textile networks usually suffer from the inability to cross different pieces of clothing due to their wired nature. Inspired by modern low-cost, vinyl heat-transfer designs, we address such needs by proposing a facile and versatile technique of integrating metamaterial railways.

2.4.1. Resonator fabrication

The grounded resonators were fabricated by stacking a copper sheet (20 μm thick) on a transparent self-adhesive vinyl film substrate. Similarly, we used aluminum foil (14 μm thick) for the ground layer. The metal/vinyl layers were stacked on the adhesive cutting mat and cut by using Silhouette Cameo 3 (Silhouette America Inc., Lindon, Utah, USA). The complement pattern of the metal foil was etched after cutting. Then the top aluminum surface of the ground stack was coated with general purpose adhesive spray. The coil (copper/vinyl stack) was then aligned and placed on top of the coated surface of the ground layer (aluminum/vinyl stack) after one minute. The final stack (copper/vinyl/aluminum/vinyl) was then immediately covered by inflammable clothing and heat pressed under 260°F for 45 s and let cool afterward. The adhesive coating should be uniform and controlled to avoid resonance frequency shifts. The resonance behavior of the grounded coils was then measured (and tuned if necessary) with a VNA (E5063A, Keysight) linked to a loop antenna via an SMA connector to ensure all elements resonate at 13.56 MHz to achieve the maximum transmission (a frequency mistuning of about 0.3 MHz was found to be tolerable). The tuning was performed by etching the copper trace (lower loop length results in lower L_R and C_R which increases the resonance). Optionally, an additional transparent vinyl may be placed on top of the resonator (adhesive facing copper) to seal the resonator and enhance mechanical and waterproof properties. The ground layer should be of the same shape as the resonating loop and cover its entire area. We added a 1 mm margin to suppress the fringing electric fields (from the resonator to the body) as well. The ground layer’s gap distances should be as small as a millimeter to eliminate the eddy currents efficiently.

The coil trace and slotted ground layer were cut out of copper and aluminum foils, respectively (Fig. 26). The copper coils minimize the network attenuation and ohmic loss per resonator as compared to aluminum (1.5 Ω versus 3 Ω for the design shown in Fig. 13), which in addition to increasing the resonator's quality factor, enhances the network's tolerance for misalignments and possible resonator mistuning. After etching, the layers were first stacked, then placed on the clothing, and finally fixed by heat pressing (Fig. 26). This simple resonator fabrication allows for unique/specialized network designs. For example, wider coils may be utilized to increase the textile area covered by the nearfield propagation through the network. In addition to transparent vinyl, colored opaque vinyl can be used to conceal the BAN and integrate with special vinyl designs, thus embedding NFC transfer capabilities underneath customizable clothing designs (Fig. 26).

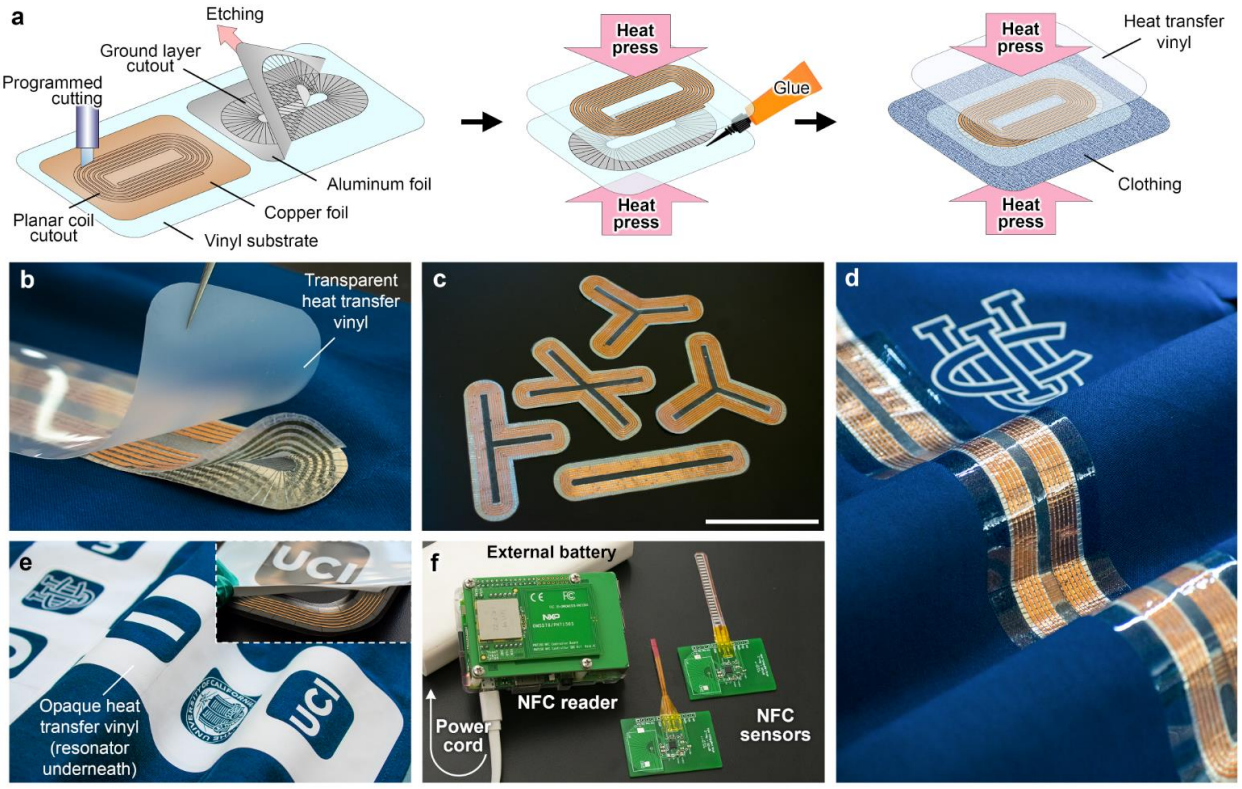

Fig. 26. Textile-integrated magnetoinductive pathway. (a) The resonator fabrication steps and (b) the blow up image of the resonator stack. (c) Various designs of flexible resonators for optimal signal transmission and power division (scalebar 10 cm). (d) Wearable modular network integrated into the clothing and covered by transparent heat transfer vinyl as a mechanical fixture. (e) The resonators can be designed to cover wider nearfield areas (in this case using a square element), and embedded underneath colored special vinyl designs. This allows network customizability both for function and style. (f) Battery-free NFC transponders integrated with strain and temperature sensors transferring respective sensor status to an NFC reader.

The fabrication process is available in Methods. Numerous shirt- and pants-integrated network architectures with transparent and colored vinyl designs are fabricated and shown in Fig. 27, which allow the network architectures to integrate smoothly alongside traditional vinyl t-shirt designs.

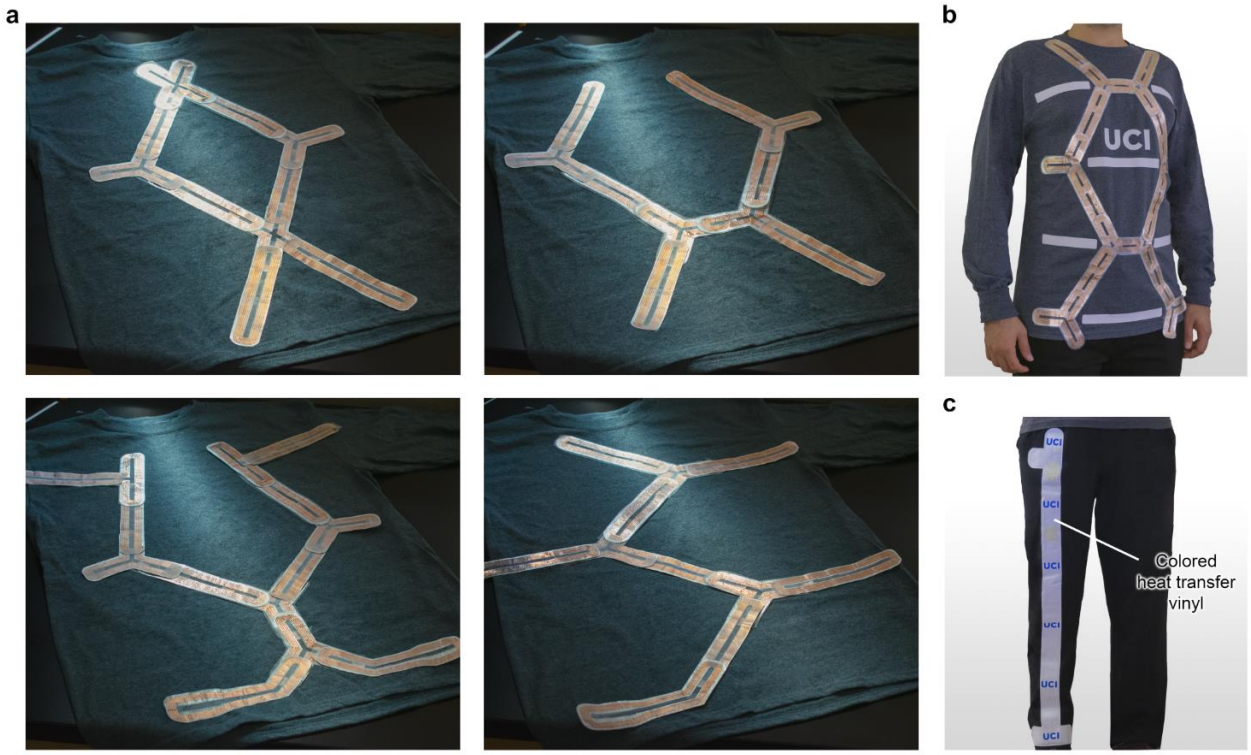

Fig. 27. Flexibility of clothing integrated designs. (a) Various shirt networks enabled by complex parallel and closed-loop metamaterial paths. The colored vinyl design may be utilized to (b) appear next to or (c) conceal the network underneath.

After designing the resonator such that it resonates at 13.56 MHz, we measured the electrical characteristics (impedance) of the identical resonators and substituted them in our model to find the approximate k_{RR} value based on the dispersion diagrams. For our rectangular coil geometry, the $k_{RR} = 0.1$ maps onto 3.2 cm of neighbor loop overlap (or $d_c = 12$ cm). One may redesign the loop resonator to match a particular clothing shape or application, resulting in a different k_{RR}, and thus d_c.

2.4.2. Clothing Integration

After locating and placing the resonators on top of the clothing, a heat transfer vinyl (transparent or opaque depending on the design preference) was cut and put on top, and then heat pressed under 300°F for 1 min and let cool afterward. Cotton clothing is often suggested by vinyl manufacturers due to its tolerance to high temperatures (Fig. 28).

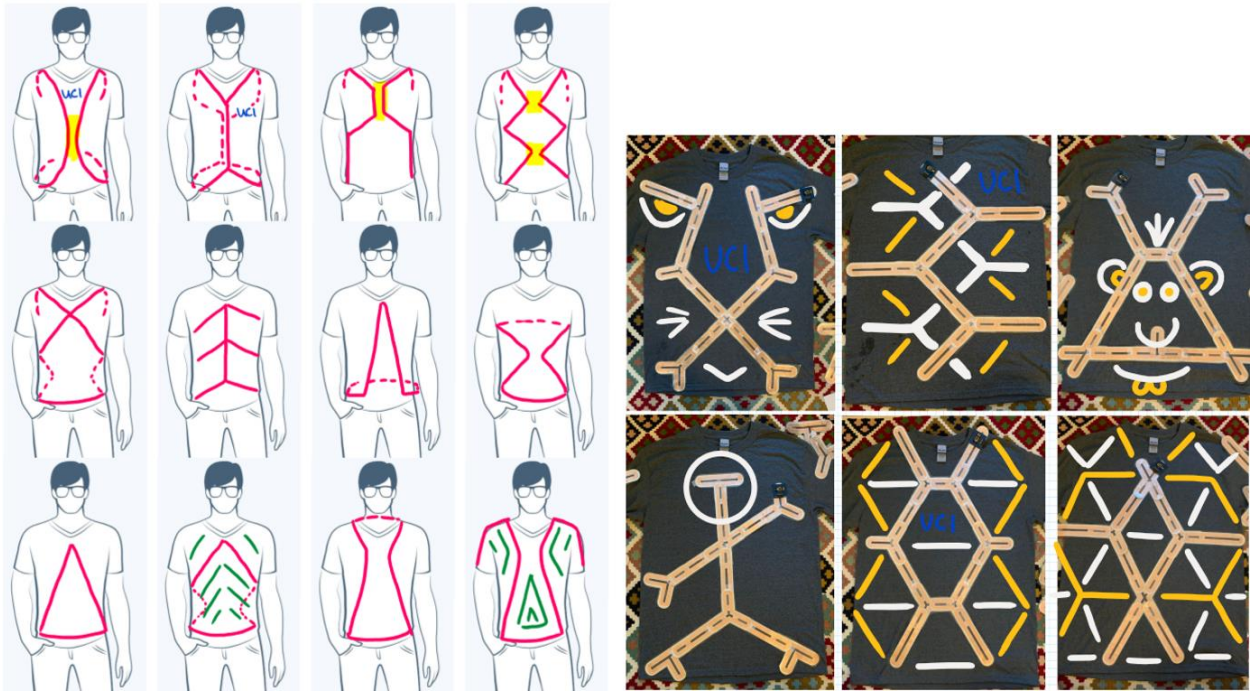

Fig. 28. Various potential MI BAN architectures on clothing.

Since the pants network passes over the pocket, the NFC reader could be placed in the pocket for appropriate excitation, similar to mobile devices routinely placed in pockets. For basic human daily activity pattern measurement, we placed two strain sensors at the abdomen area and knee (for bending and pacing recognition) and a temperature sensor above the hip (recording near-body temperature), with sensing nodes located in the vicinity of the network. The standalone reader (placed on the pants pocket) was powered up via a wired external battery, and sensor data was streamed wirelessly to the online cloud. Here, the co-location of sensors does not matter as long as they are within the reader's sensitivity range (equivalent to the transmission above approximately -35 dB here).

2.4.3. Mechanical Performance

The versatility of our network was evaluated by various readers and sensors (including off-the-shelf chips and an optimized board design) shown in Fig. 29, that can be placed close (roughly within the vertical distance of 3 cm) to any point of the resonator chain. Our sensor board is based on a commercially available NFC transponder chip integrating an analog to digital unit that connects to a wide range of analog sensors, such as strain and temperature sensors (Fig. 29). Multiple NFC transponder access and readout were implemented by both an NFC-enabled mobile phone and programmed hardware.

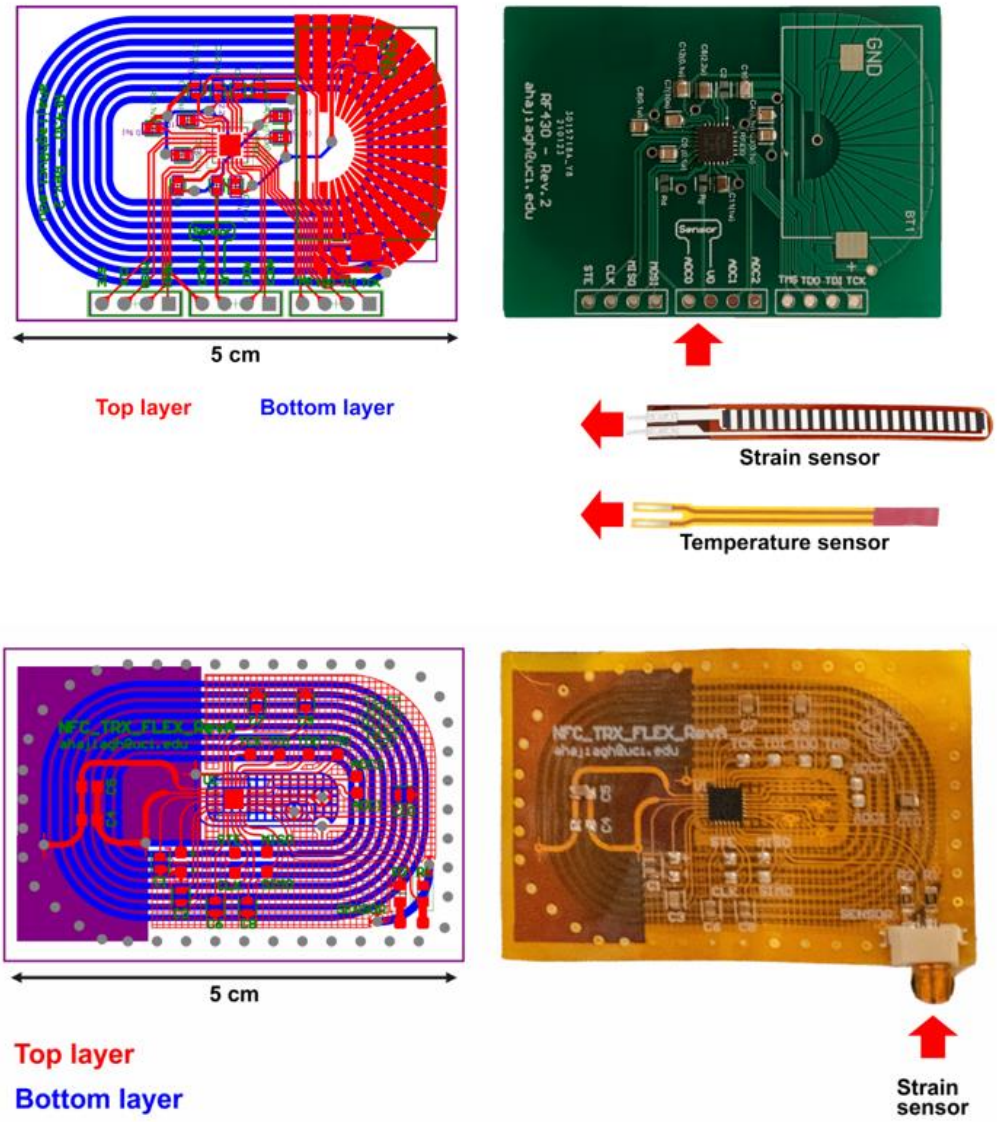

Fig. 29. The rigid and flexible board designs of the NFC transponder. The loop antenna on the bottom layer is designed to attain a maximal coupling factor to the resonator's design. The optional battery was unused in this study.

The flexibility of resonator elements exhibiting complex designs is improved by employing thin aluminum, copper, and vinyl coatings. Each fabricated resonator element has an overall thickness of about 300 µm and does not impede routine clothing movements. The spectral stability of a resonator array (80 cm long and integrated into cotton clothing) was examined by measuring the transmission (S_{21}) along the two ends of the network under various levels of bending and axial twisting. This shows a steady transmission with a minimum bandwidth of 16%. The functionality of the BAN is tested under more severe mechanical deformations such as multiple full (360°) bendings and random creasings. The repeatable stability of the BAN was examined under mechanical distress by creasing at random locations along the network (followed by immediate unwrapping and repeating several times) and is shown in Fig. 30.

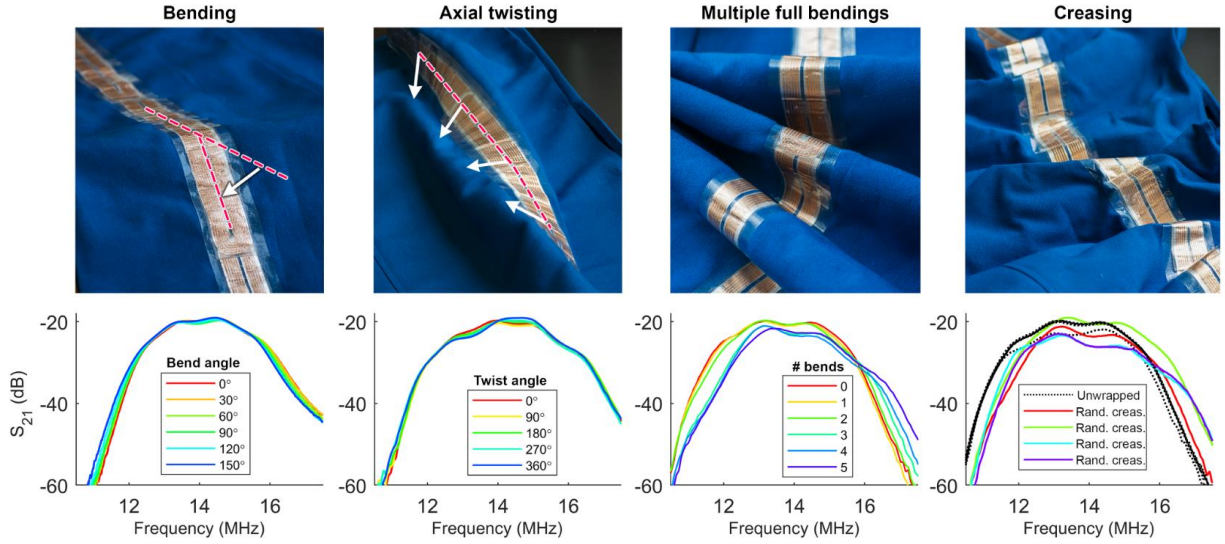

Fig. 30. Flexible, drag-and-drop NFC networks on textiles. Spectral stability of the clothing integrated pathway under mechanical deformations such as bending, axial twisting (per meter length), multiple 360° bendings, and repeated creasing/unwrapping. The 80 cm-long deformed inline network passes the transmission and bandwidth requirements enforced by NFC protocols.

2.4.4. Readout and Control Mechanism

We implemented our sensor ecosystem using ISO15693 sensor transponder RF430FRL152H, Texas Instruments (TI) with unique identifications (UID), and designed a miniature board containing NFC loop antennas (to couple better with our resonators) and analog sensor biasing resistors to minimize the analog to digital (ADC) gain error. The chips were then programmed over-the-air to announce the ADC output (known as the sensor value) upon the reader's interrogation command under ISO15693. The programming was performed using TI's GUI to interface between the TRF7970A, TI (mounted on MSP430G2553, TI), and the transponder chip. We used off-the-shelf strain (Short Flex Sensor, Adafruit Industries LLC) and temperature (CTTS-203856-S02, Amphenol Advanced Sensors) sensors embedded in our transponders. The sampling rate (32 Hz) here is significantly higher in comparison to prior NFC multiplexing techniques (8 Hz) for a single sensor [33]. The strain sensor (here used under 30% strain, enough to measure knee/ankle bending during activities) showed less than 200 ms latency, which allowed a sampling rate of 5.6 Hz/sensor. The sampling rates for activity measurement (5.6 Hz/sensor) were set based on the PRR (above 95% for at least 5 sensors) and the Nyquist sampling theorem (that the sampling rate must be over twice as fast as the activity's highest frequency component, which was estimated to be less than 2.5 cycles/steps per second). The PRR studies (in Fig. 31) were run for 10 min (for each number of sensor and each sampling rate) to ensure the PRR values reflect the steady-state of the network.

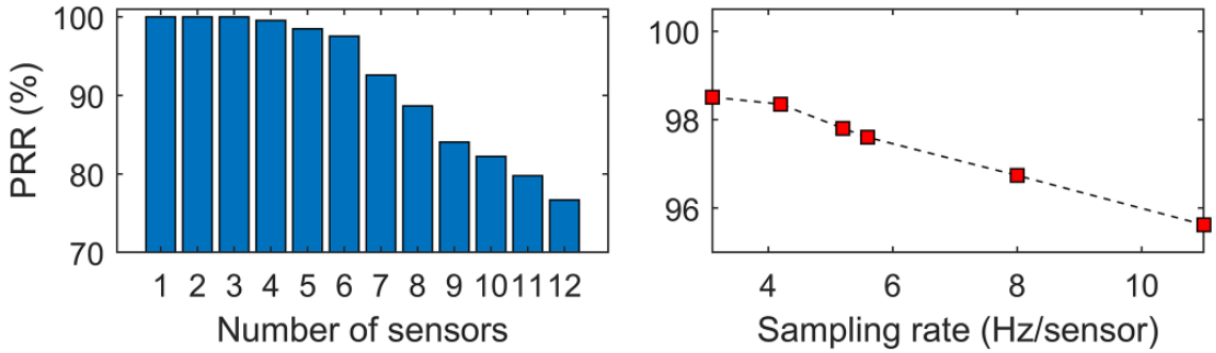

Fig. 31. The averaged NFC PRR measured for various numbers of sensor-transponders along the network with a refresh rate of 5.6 Hz per sensor (and distributed over 1 m of a network). The PRR for 6 NFC transponders with various sampling rates.

Here, we utilized a software-based time domain multiple access (TDMA) to realize switching between sensing nodes. The controlled surface propagation of magneto-inductive waves eliminates the need for multiple nearfield antennas (connected by wire), [78], [79] or complex antenna switching schemes (needing active microelectronics). This allows conventional NFC-enabled smartphones to operate as compatible readers. The network's wireless efficiency was examined by measuring the NFC packet reception ratio (PRR), defined as the ratio of the number of packets successfully received by the reader to the total number of transmitted packets. Each packet consists of sensor information from all transponders along the network during one refresh. We note that in practice, however, strain sensor latency and hysteresis limit its performance at higher frequencies (see Methods). In addition, the TDMA approach allows up to 12 sensors to be connected along the network. There is a tradeoff between the sampling rate, number of sensors, and packet loss. The PRR is measured for varying numbers of sensors in reach of the reader (with a sample rate of 5.6 Hz per sensor), as well as for various sampling rates (with 6 sensors) in an inline network of an overall length of 100 cm (Fig. 31).

The ability to continuously monitor wireless NFC-enabled devices all-along the magneto-inductive resonator railway offers useful applications in unique scenarios such as moving joints within actuators/ robotics (which cannot be powered through NFC's regular range), or within highly traceable terminals within gates wherein multiple objects may locomote along a local pathlength (where traditional radiofrequency identification would again fail). To validate the drag-and-drop feature of the BAN, we power and probe sensors moving along the network (1 m length) at different velocities and various numbers of sensors within reach. The surface-bound magnetic profile of the planar magneto-inductive array allows for relatively fast sensor dragging with a reliable PRR of above 95% (Fig. 32).

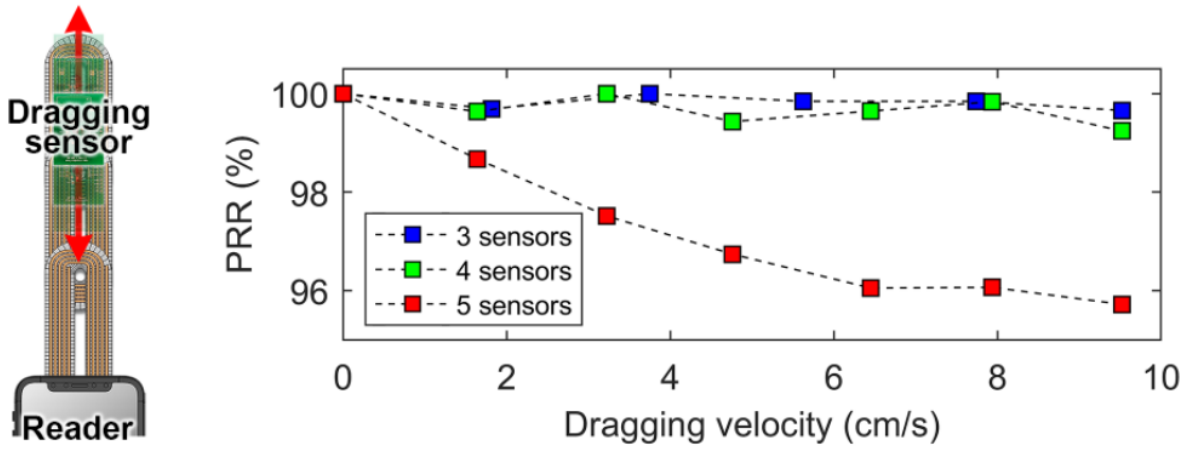

Fig. 32. Packet loss for a moving sensor dragged under various velocities along 1 m of the magneto-inductive network for different numbers of sensors under a sampling rate of 9 Hz/sensor.

To evaluate the worst-case transmission scenario, any packet with at least one failed sensor data (even if all other sensor data is delivered successfully) is counted as lost. Our software-based TDMA (integrated into an NFC pathway ecosystem with sensing nodes 1 m away from the central reader) reached a maximum refresh rate of 32 Hz for one sensor while exhibiting a PRR of above 98%. This approach allows for a wide array of sensor types for frequent monitoring (to maintain the same PRR with a larger number of sensors, the sampling rate should be lowered accordingly). We utilized NXP PN7150 NFC controller shield mounted on Raspberry Pi to perform the sensor readout, which broadcasts the reading command along the BAN. To avoid collision among the transponders receiving this command, the multiple access was implemented with round-robin scheduling to enable time division between the NFC transponders discovered at the time and looped until receiving the termination command. For sensors with higher readout priority or sampling rate, the rate-monotonic scheduling might be beneficial.

The BAN's versatility test was performed using STEVAL-SMARTAG1 NFC transponders. Among the embedded pressure, temperature, humidity, and accelerometer sensors, we utilized the latter to detect running while placing the transponder on the ankle. The readout was performed with ST NFC Sensor application on an Android device.

2.4.5. Network Architecture

The upper body part of our studied BAN was designed in a zigzag shape, passing over the abdomen and chest area, while offering the ability to extend the network to the back of the body (potentially interacting with NFC-enabled seats). Similarly, we designed an inline array starting from the hip, passing over the knee, and ending by the ankle. The shirt's network ending was designed to overlap with that of the pants within a vertical distance, thus enabling wireless signaling across different pieces of clothing (Fig. 33).

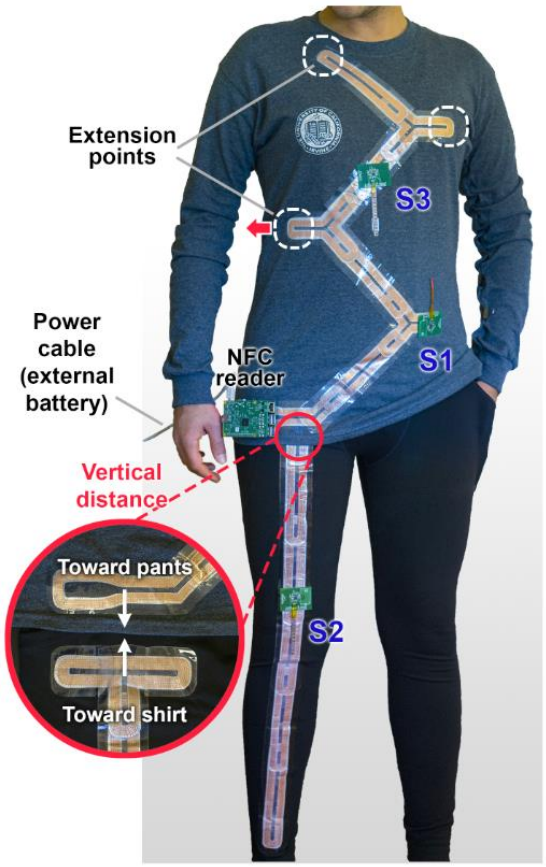

Fig. 33. In vivo multi-transponder and multi-BAN communication by textile-integrated waveguides. The shirt and pants on top and underneath the pants/shirt terminals. The NFC reader receives information from multiple sensors and is connected to an external battery.

For detailed sensor placements see Methods. The multipoint sensor readout was performed while standing, walking, squatting, and waist-bending at different temperature zones simulated indoors. All sensor values were timestamped, transmitted, and recorded by the reader at a sampling rate of 5.6 Hz/sensor (equivalent to an overall rate of 17 Hz for all sensors operating together). To minimize the resistive strain and temperature sensor's hysteresis effect and random noises, we applied a data processing algorithm for each sensor value (processing flowchart shown in Fig. 34).

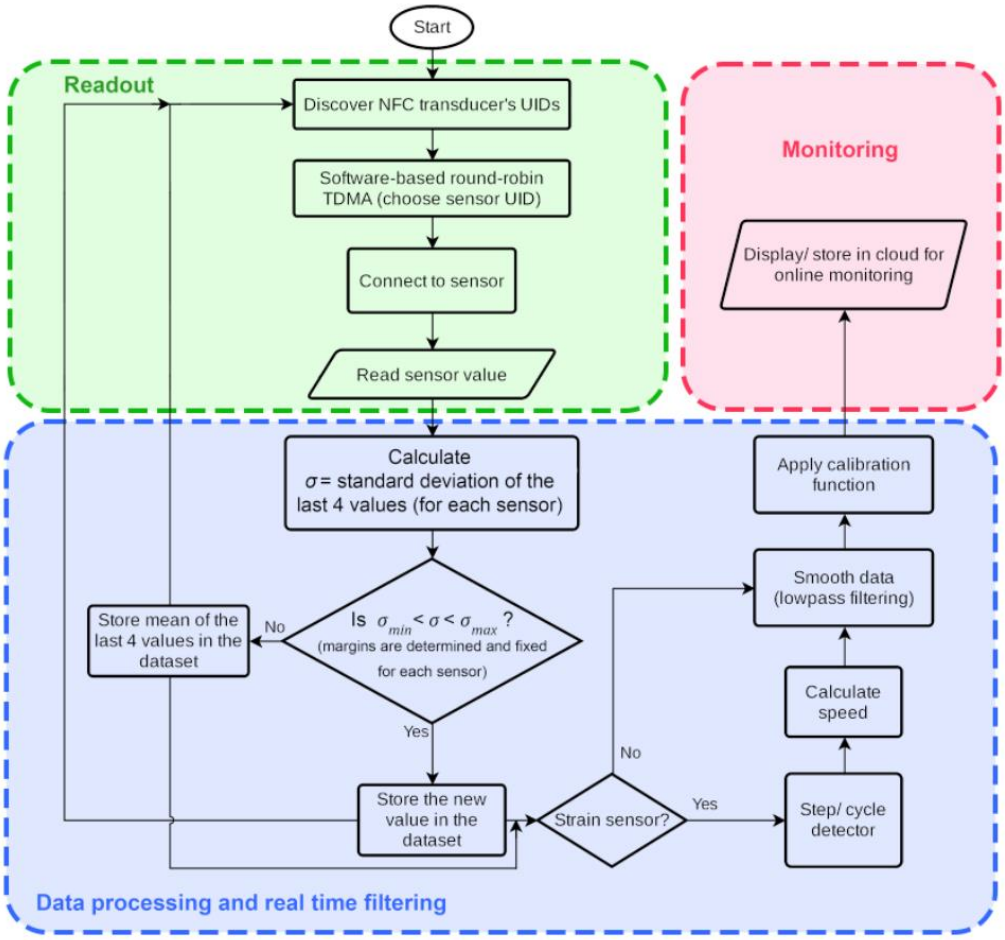

Fig. 34. Flowchart for software based TDMA and sensor data processing. The sensor value storage decision (based on the standard deviation) allows for holding the sensor values close to the previously logged data, ultimately rejecting artifacts caused by the analog sensor noise in real time and without inducing considerable latency. The SD margin and calibration function is unique to each sensor type and does not change throughout the monitoring process.

This strategy was implemented in real time and a few seconds after the start of recording (see Methods for filtering details). This approach effectively achieved steady data with minimal noise fluctuations. The sensors' raw and filtered samples during a short-term exercise (walking for 8 steps, 6 bends, and 7 squats, each in two different temperature zone) are depicted in Fig. 35.

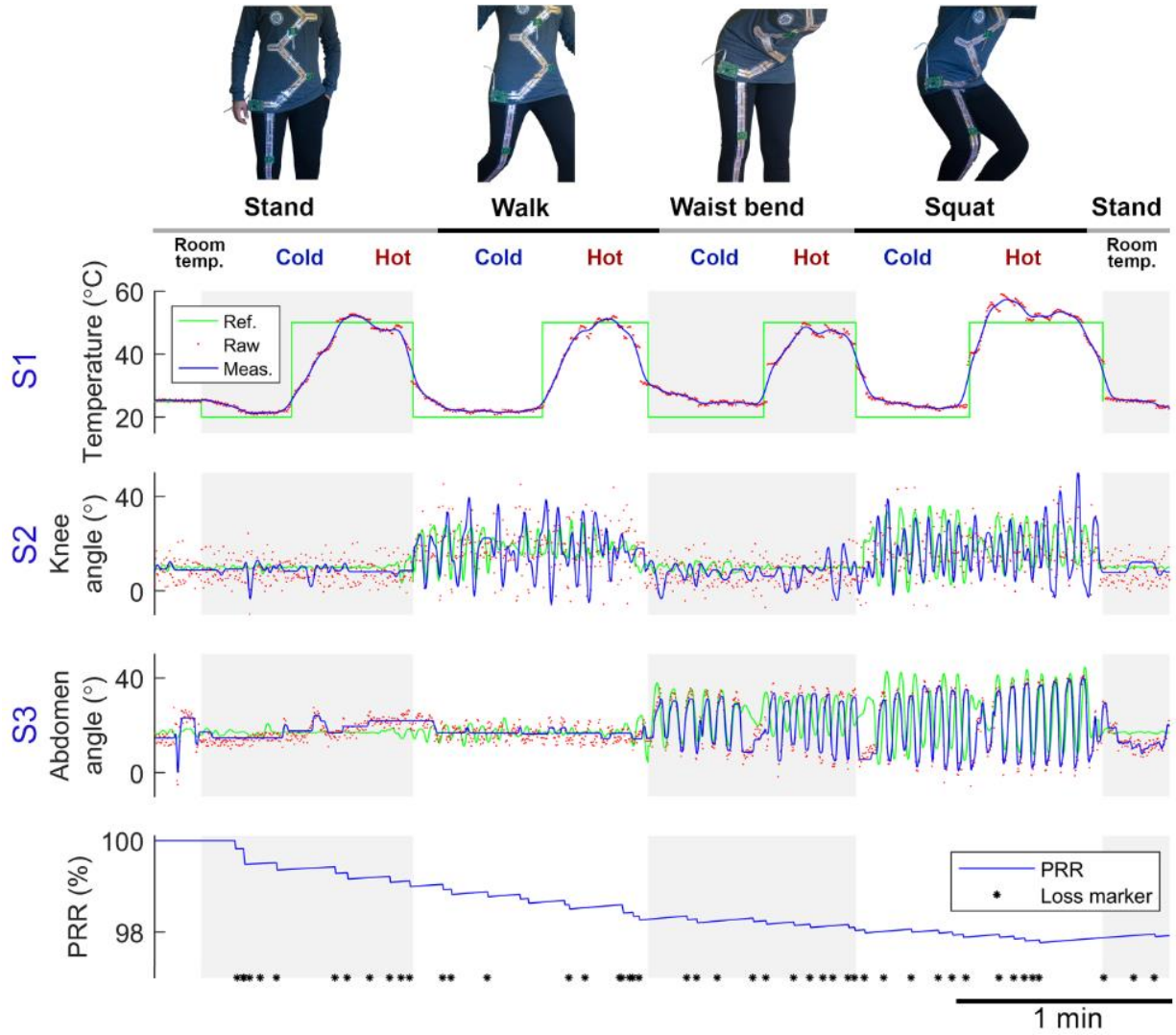

Fig. 35. Real time short-term and low-speed monitoring of human activity realized by time division-based multiple sensor readout within the BAN with a sampling rate of 5.6 Hz/sensor (dots and solid lines show raw and filtered data, respectively).

The cold/hot temperature zones correspond to locally different but close indoor spots generated by a fan/heater (the temperature profile sampled by an infrared thermometer). For applications with conservative power consumption, low sampling rate versions of the exercises are performed as well (Fig. 36).

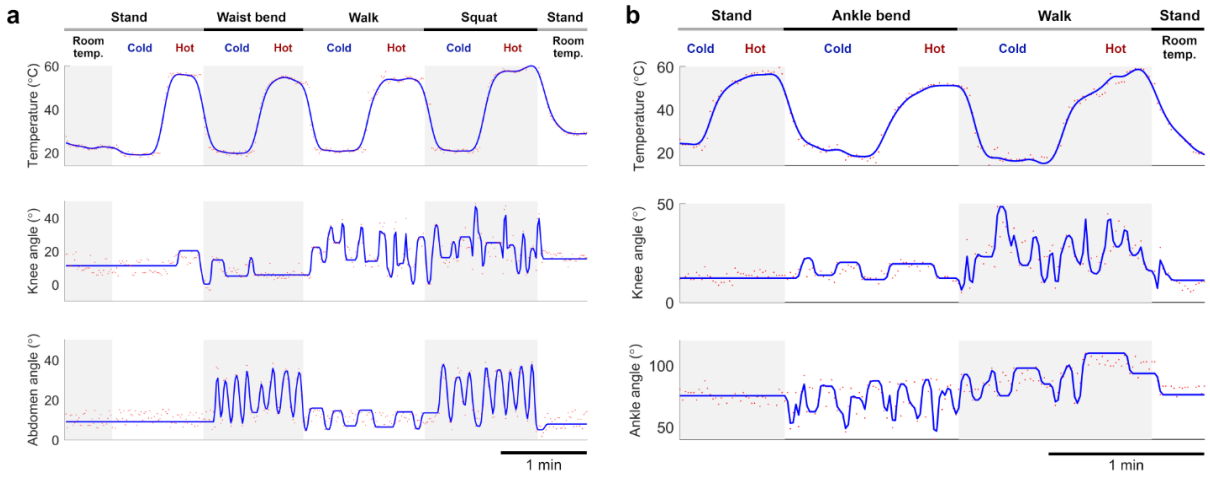

Fig. 36. Additional in vivo tests of the network's versatility at various sampling rates and for off-the-shelf NFC sensor/smartphone. (a) Full body (temperature sensor on the belly, and strain sensors on knee and ankle) and (b) lower body (temperature sensor on the hip, and strain sensors on knee and abdomen) movement detection at a low sampling rate (1 Hz/sensor or 3 Hz overall).

2.4.6. Textile-integrated System Validation

To validate the behavior of the magneto-inductive BAN under longer-term function during more strenuous exercise, we relocated the temperature sensor along the BAN to near the underarm and fixed the sensor's probe on the skin (through a hole on the shirt to capture core temperature correlate as well). We used a conditional peak detector algorithm to extract step and pace from knee and ankle angle information (Fig. 37).

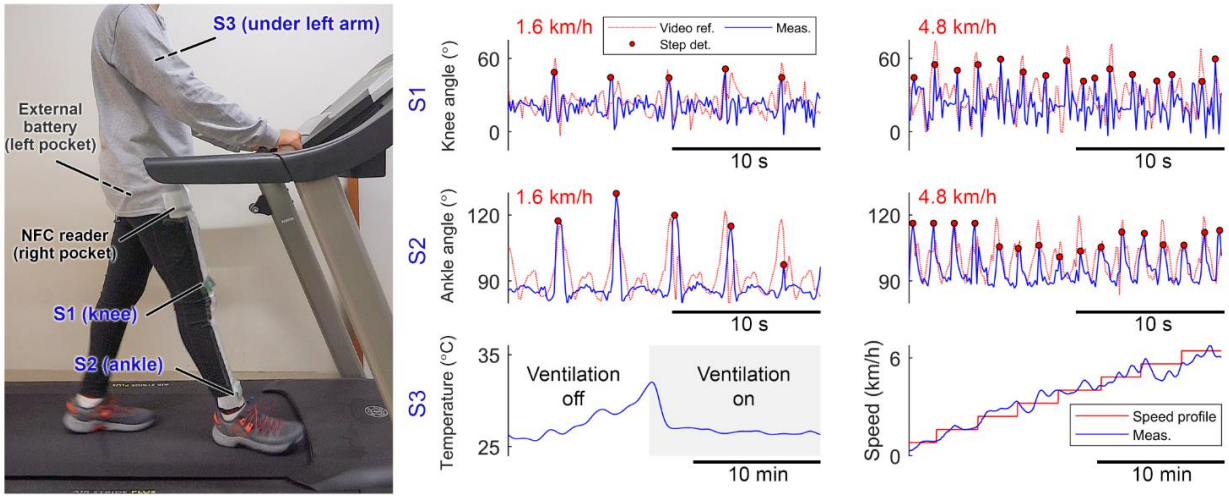

Fig. 37. High speed, long-term indoor walk/running activity measurement. The test was performed under a gradually increasing velocity profile for 25 min and BAN was integrated into clothing with colored vinyl. Monitoring of sensors during indoor running under various velocity profiles with a sampling rate of 10 Hz/sensor. Steps are detected and marked by circular markers.

The network's PRR was recorded during the activity and is shown in Fig. 38**.**

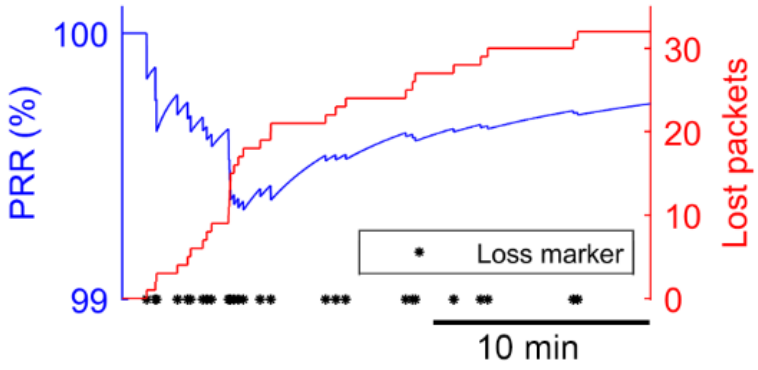

Fig. 38. The long-term packet loss monitoring during indoor running.

The long-term functionality is tested for the lower body part of the network with knee and ankle angles and a temperature sensor (fixed on the skin to capture skin's surface temperature) during indoor cycling (Fig. 39). Due to the compatibility of the magneto-inductive BAN with the NFC standard, the network operates for a wide range of commercially available NFC-enabled devices (such as smartphones and sensors), with either real time or buffered, and offline or cloud-based ecosystems. A sample off-the-shelf NFC ecosystem is integrated into our BAN and tested in Fig. 39.

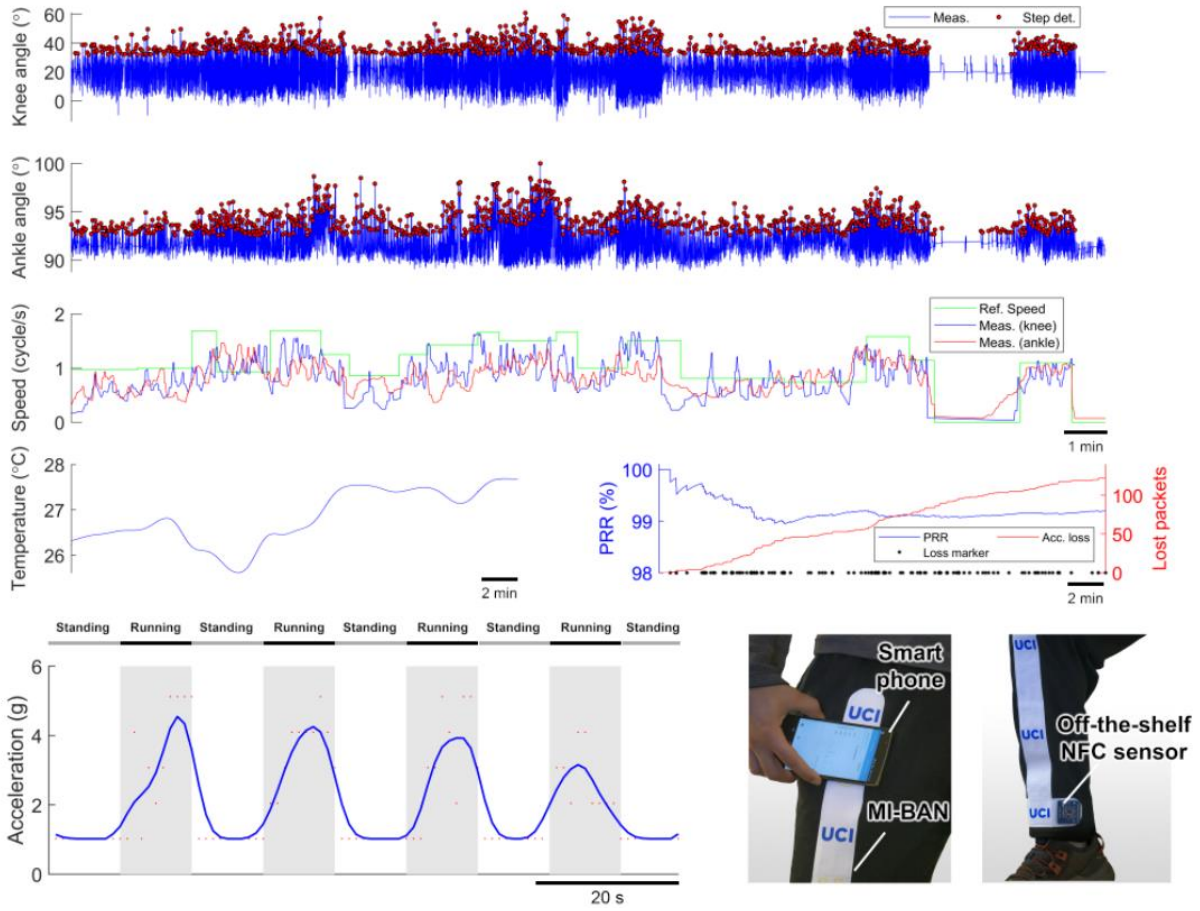

Fig. 39. Lower body cycling detection at a higher sampling rate (5.6 Hz/sensor). Test of network's compatibility with off-the-shelf sensor and compatible Android application (dots and solid lines show raw and filtered data, respectively).

Interestingly, the surface propagation characteristics of the magneto-inductive structures enable seamless body-to-body communication with no need for terminals. The link readily establishes by putting any point of the two contributing BANs close enough (similar to the vertical distance between different pieces of clothing as shown in Fig. 40). The external NFC may similarly be generalized to nearby local networks integrated into, for example, driver seats or gateways for monitoring and authentication purposes.

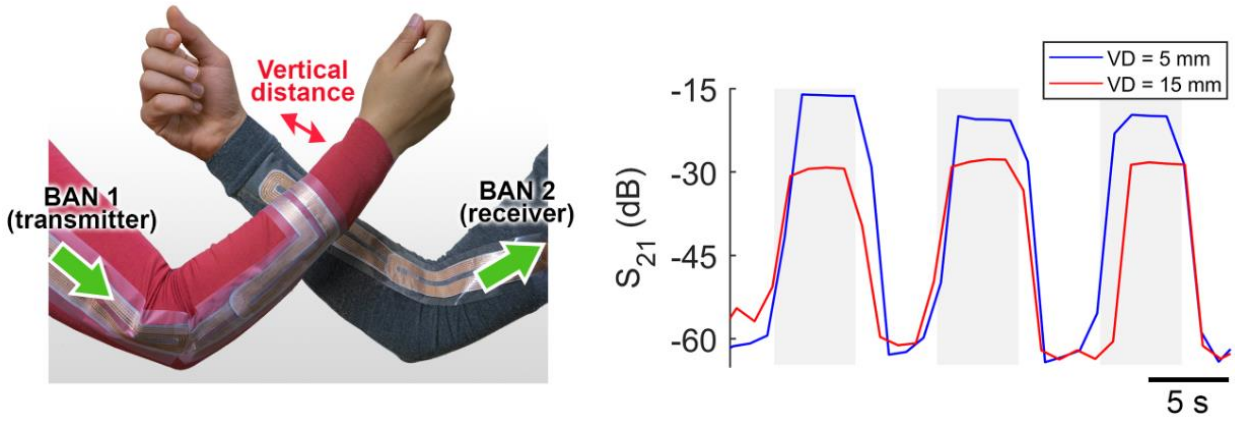

Fig. 40. Body-to-body communication enabled by NFC's plug-and-play characteristics and its measured transmission during dragging the hands close and far over time (comprising an action of a "digital high-five") for various VD values.

Due to the vinyl sealing of the network, it demonstrates a good spectral stability versus wetting. To mimic human sweating (or light raindrops), we added incremental volumes of salty water (30 mL total, with NaCl concentration of 200 mg/L) on top of the network (covering about 90 cm^2 of the resonators), resulting in 3% frequency shift and maintaining steady network transmission. Additionally, the textile survived 20 minutes of handwashing in cold water with stable measured transmission over various washing phases (Fig. 41).

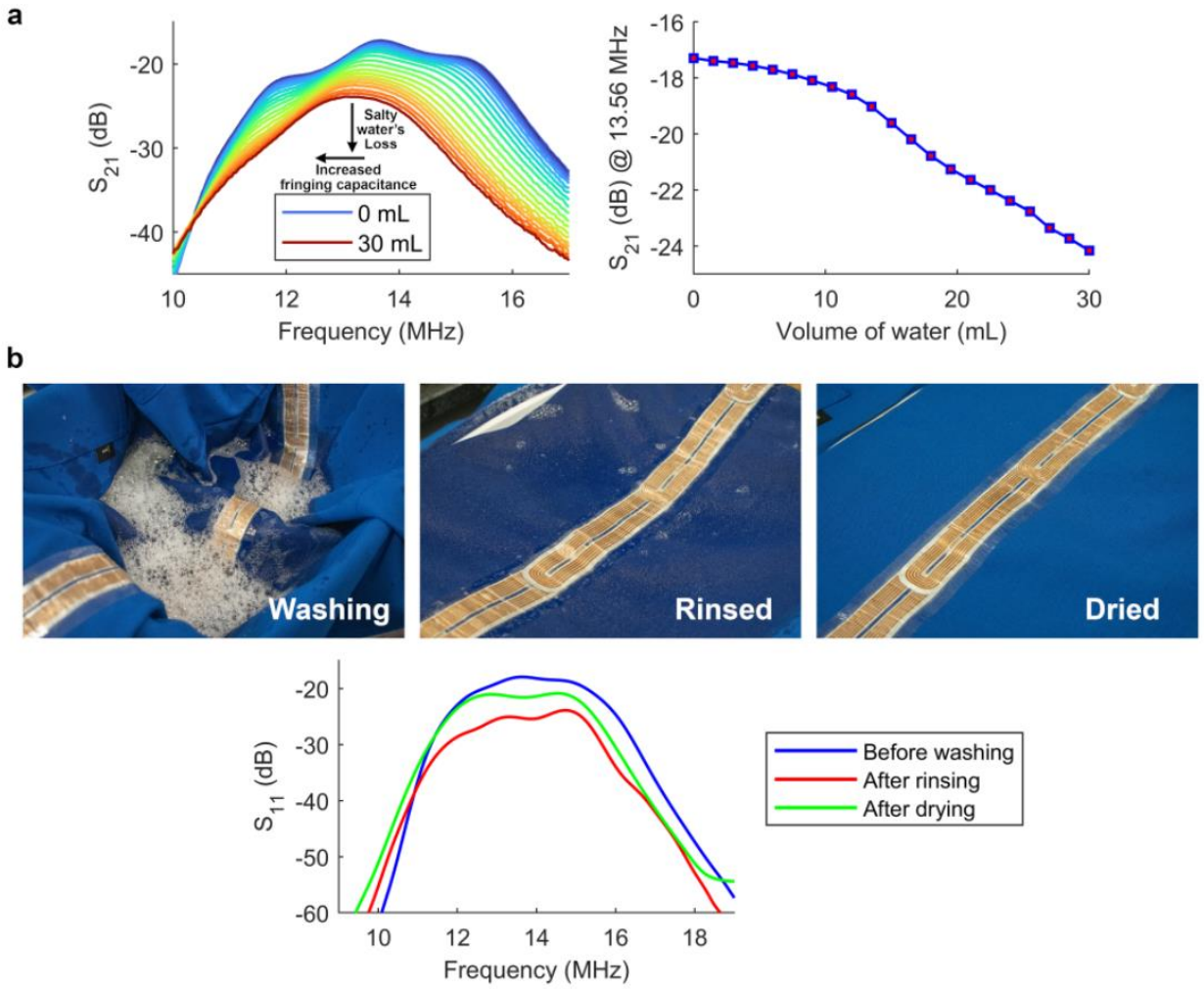

Fig. 41. Spectral stability versus wetting and washing. (a) The frequency and magnitude shifts are caused by the high permittivity (increasing the fringing capacitance of the resonators) and the loss of the added water. Incremental doses (150 µL) of a stock NaCl solution (200 mg/L) were added to mimic the electrical conductivity of human sweat or raindrops. (b) Robustness of the magneto-inductive BAN's spectral characteristics during different phases of washing. The handwashing test was performed with cold water (room temperature) and a total time of 20 minutes.

The magneto-inductive BAN can be synthesized on-demand and at a low cost for personalized wearable networks. This ecosystem can be utilized in various clinical, athletic, and daily routines to facilitate real-time healthcare and status monitoring. For instance, integration into hospital patient uniforms could allow for seamless patient monitoring where sensors are dragged-and-dropped across clothing. Professional sports clubs or federations may develop highly customized networks that may be both integrated with their branding and optimized to serve specific needs in athletic training and monitoring. The vinyl-based elements enable users to freely create and readily arrange the network without special equipment, and can be targeted for either local or long-range monitoring along the body. Sensing nodes may be swapped or rotated seamlessly to facilitate plug-and-play measurement of a variety of relevant parameters.

Table 1. Comparison of recent battery-free over-the-air BAN technologies.

Technology	**Magneto-inductive metamaterials (this study)**	**Spoof surface plasmon metamaterials** [8]	**Coils connected by wire** [33]	**Qi powered** [34]	**RFID** [6]
Standard	NFC	Bluetooth	NFC	Qi	Specialized
Frequency	13.56 MHz	2.5 GHz	13.56 MHz	142 kHz	>10 MHz
Propagation security	Bound to surface	Bound to surface (for full radiative to guided mode redirection)	Bound to surface	Bound to surface	Prone to third party listening
Operational range	Radius of ~ 1 m (drag-and-drop available)	Radius of ~ 1 m (drag-and-drop available)	Equal to wire length (drag-and-drop unavailable)	Equal to wire length (drag-and-drop unavailable)	Up to 25 mm at 13.56 MHz (lower range for higher frequencies)
Clothing integration difficulty (for the end-user)	Easy (inexpensive vinyl resonators heat transferred on pre-existing clothing)	Easy (relatively expensive conductive fabric and adhesive)	Difficult (embroidered rails not available on pre-existing clothing)	Easy (cheap wires attached on clothing)	Not applicable
Sensitivity to body proximity	Insensitive (low loss integrated ground layer)	Sensitive (relatively higher at microwave band)	Sensitive (potentially reducible by appropriate grounding)	Sensitive	Sensitive
Multi-clothing (vertical distance) communication	Up to 30 mm, no need for terminals (low loss associated with discontinuities)	Up to 10 mm, no need for terminals (relatively higher loss associated with discontinuities)	Up to ~ 30 mm, needs terminals	Up to ~ 10 mm, needs terminals	Not applicable
On-demand extension	Available (no need for electrical/ mechanical connection)	Unavailable (considerable loss upon discontinuity made by attachments)	Unavailable (conductive thread sewing needed)	Unavailable	Unavailable
Reader/sensor (or multi-BAN) placement	Anywhere along the BAN	Anywhere along the BAN	Only on the BAN's hub/terminals	Only on the BAN's hub/terminals	Only on the sensor
Versatility	Compatible with standard	Compatible with standard	Compatible with standard	Compatible with standard	Specialized reader/sensor communication

The indoor walk/run was performed under varying speed profiles and a locally-controlled ventilation system nearby and sensors were probed at a sampling rate of 5.6 Hz/sensor. The knee and ankle angles obtained from the BAN-based measurement were compared with a reference video processing toolbox (video motion-capture) to validate measured actions. The running test was repeated three times (each 25 min) under room temperature, in which the ventilation was turned on in the middle of the experiment. Here, the core body temperature correlate increased during more strenuous activity, and expectedly reduced (to room temperature) when ventilation was initiated.

The video tracking of human activity tests subject was performed using OpenCV library implemented by Python programming. The measured temperatures were verified with an infrared thermometer. The in-vivo exercise tests were run by a male human (172 cm tall and 62 kg).

The real time filtering operates based on the standard deviation (SD) of the last 4 samples (independently for each sensor) and decides to filter or pass the incoming data depending on the fluctuations. The minimum and maximum bounds of the acceptable SD are found by the strength of the random noise and extreme fluctuations (such as dropped packet or analog sensor overflow), respectively. Any sensor values between these boundaries are passed, or otherwise the mean value of the last 4 samples (including the new sample) is stored to hold the acceptable data. The thresholds vary based on the sensor's noise characteristics and obtained by calibration, and were not altered through the experiments.

2.4.7. Sensor compatibility

The sensor boards designed here have the option to incorporate a wide range of analog or digital sensors. We explored maximizing the compatibility by utilizing FPC connectors and compatible custom made laser graphene induced strain sensors for enhanced reliability and sensitivity (Fig. 42).

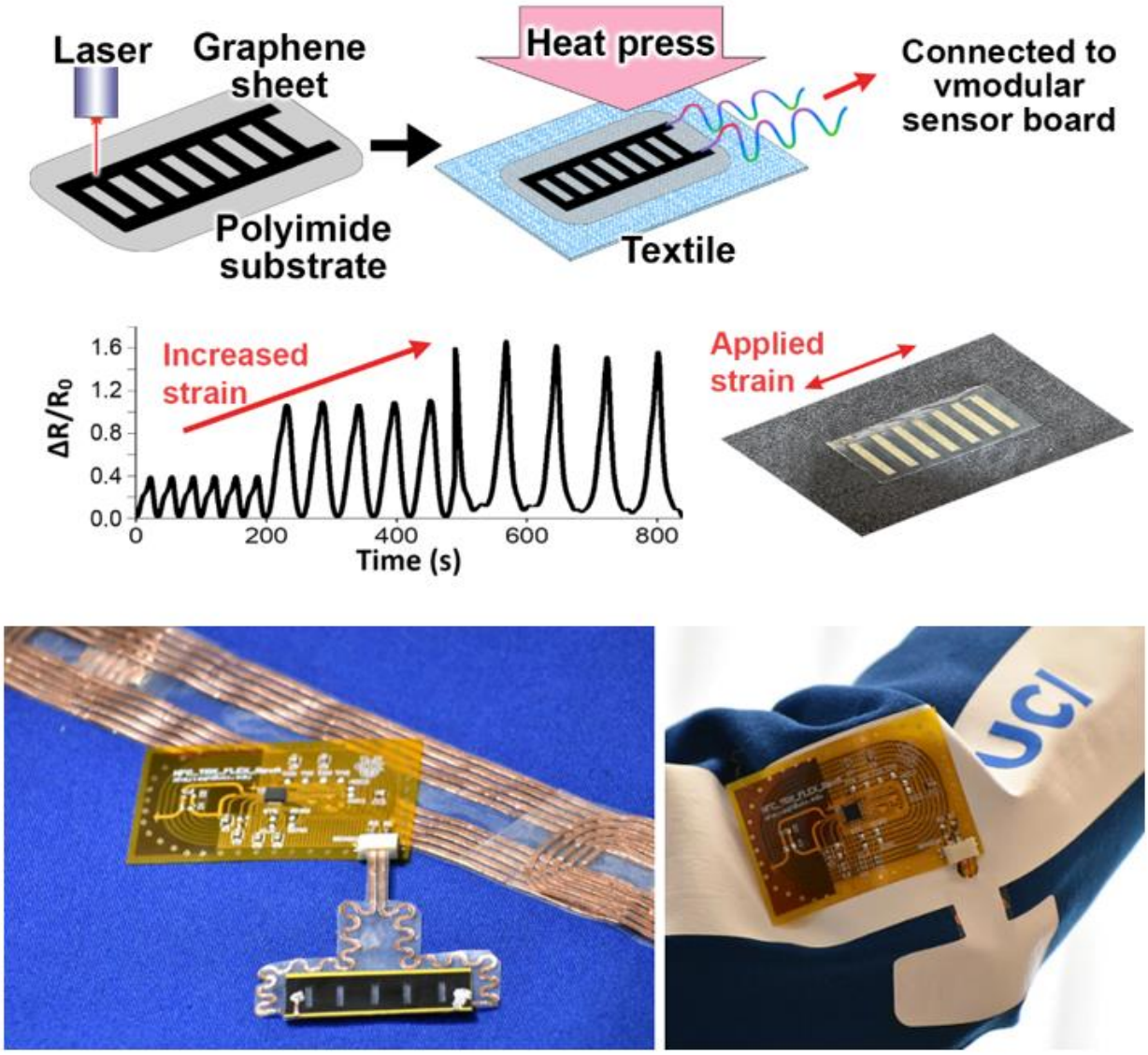

Fig. 42. Integration of sensor boards to custom-made sensors.

2.4.8. Integration with Virtual and Augmented Reality Models

The human motion data captured by the proposed MI BAN can be seamlessly integrated with virtual/augmented reality technologies to enable real time feedback for workout training and physical therapy assistance (Fig. 43)

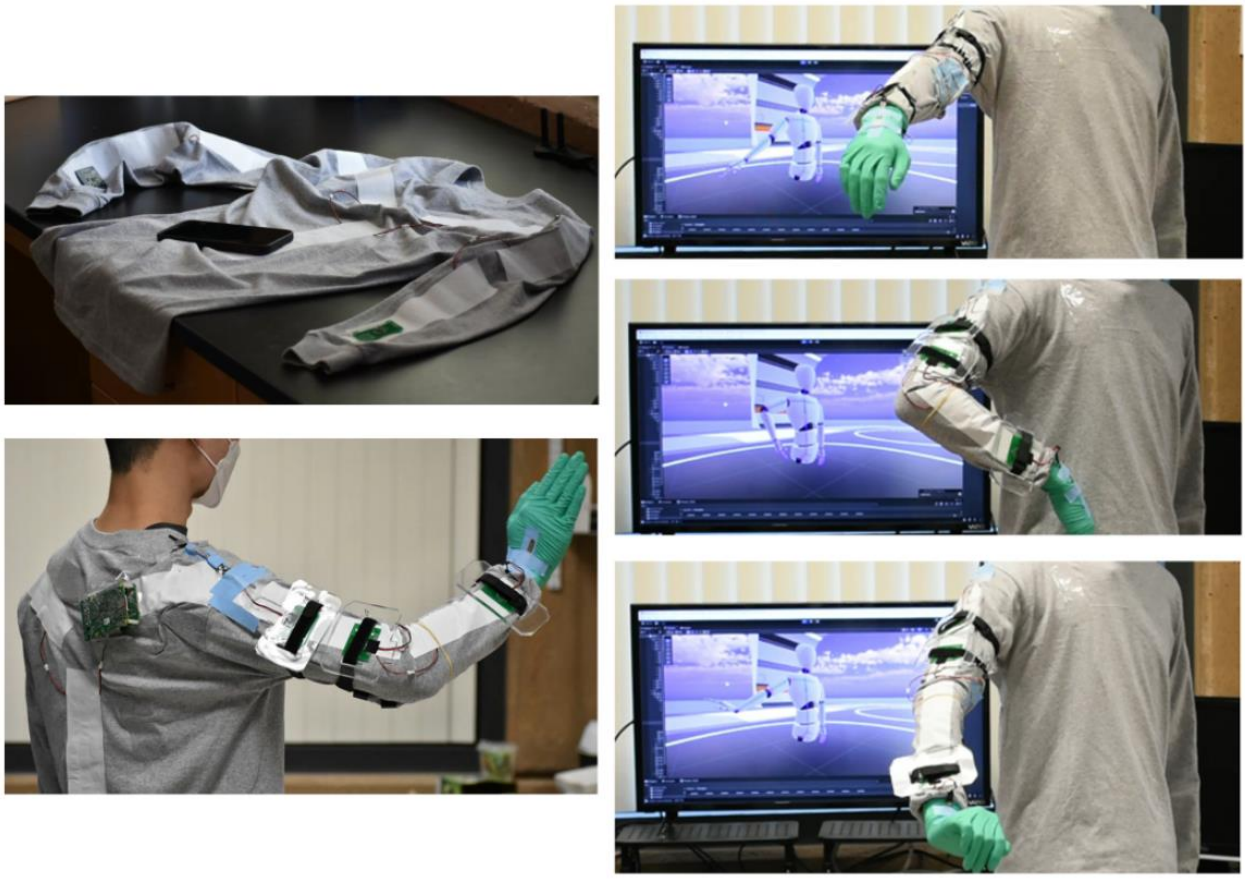

Fig. 43. MI BAN integrated with integrated with virtual/augmented reality technologies.

2.4.9. Two-dimensional MI mats

The efficacy of magnetoinductive waveguides within a single dimension, compliant with NFC protocol, has been established. In this context, we present a comprehensive demonstration showcasing the capability of magnetoinductive waveguides to propagate sub-wavelength magnetic waves across distinct surface topologies (Fig. 44). This encompasses a meandered one-dimensional linear array configuration, along with an two-dimensional lattice-shaped magnetoinductive array (Fig. 45). Furthermore, we introduce a novel nested array of magnetoinductive resonators, augmenting the repertoire of architectural possibilities (Fig. 46). An additional proposition encompasses a hybrid approach that adeptly amalgamates the three aforementioned strategies, thereby offering a versatile toolkit for tailored waveguide design ().

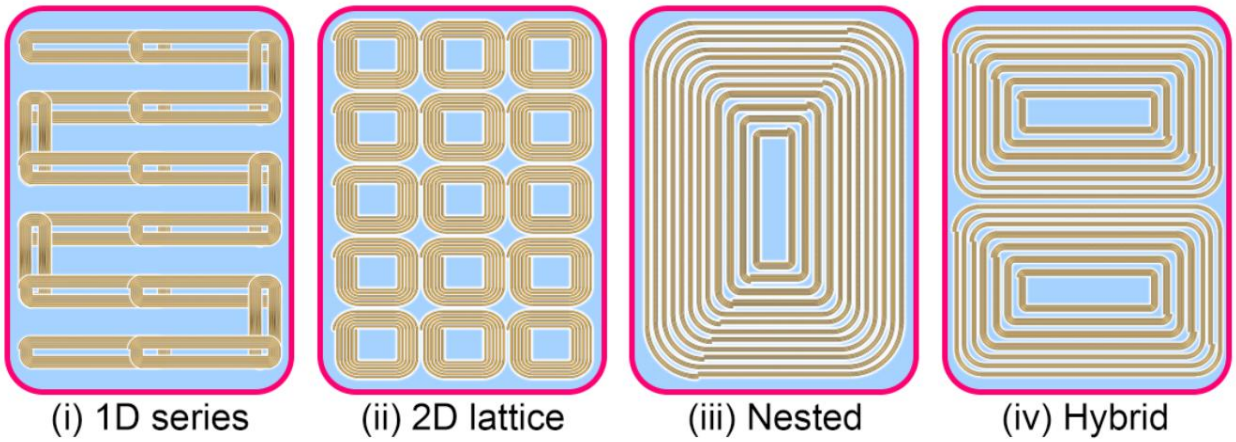

Fig. 44. Various MI architectures to cover a targeted surface area.

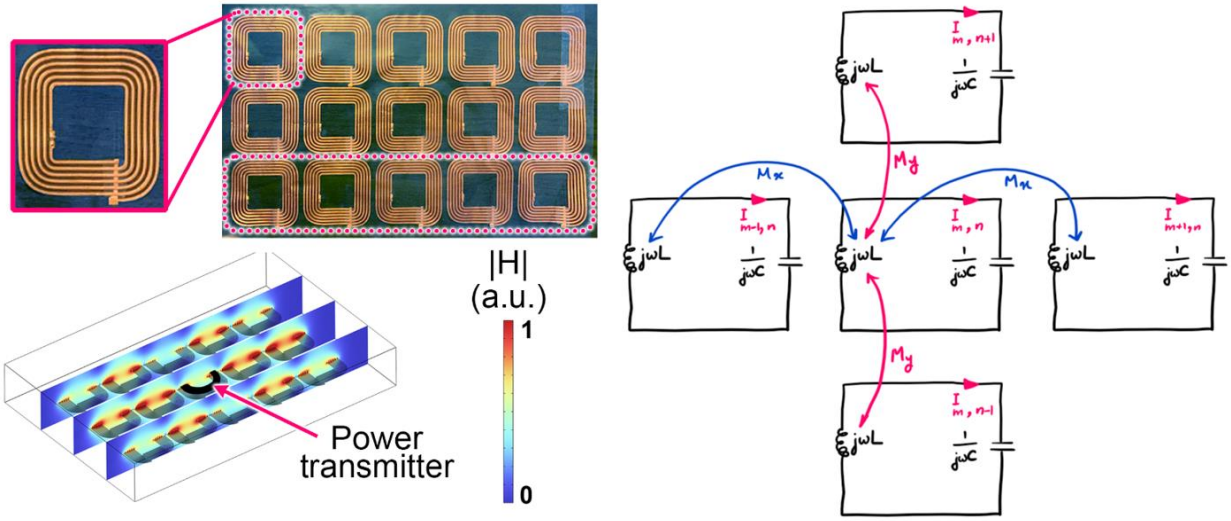

Fig. 45. 2D lattice network can be used to cover a surface to enable NFC connectivity across a relatively larger real state.

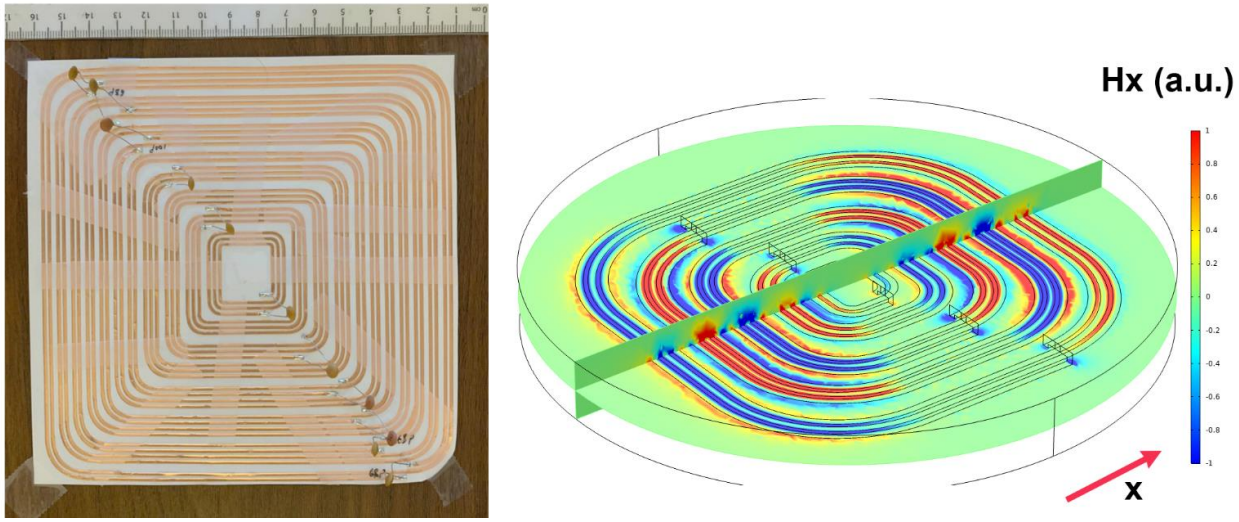

Fig. 46. Nested MI arrays are conceptually similar to conventional MI structures as they resonate at the same frequency, however their geometry and architecture is inherently different than a series chain of identical resonators.

The transmission profile of 2D lattice and proposed nested MI arrays are compared in Fig. 47.

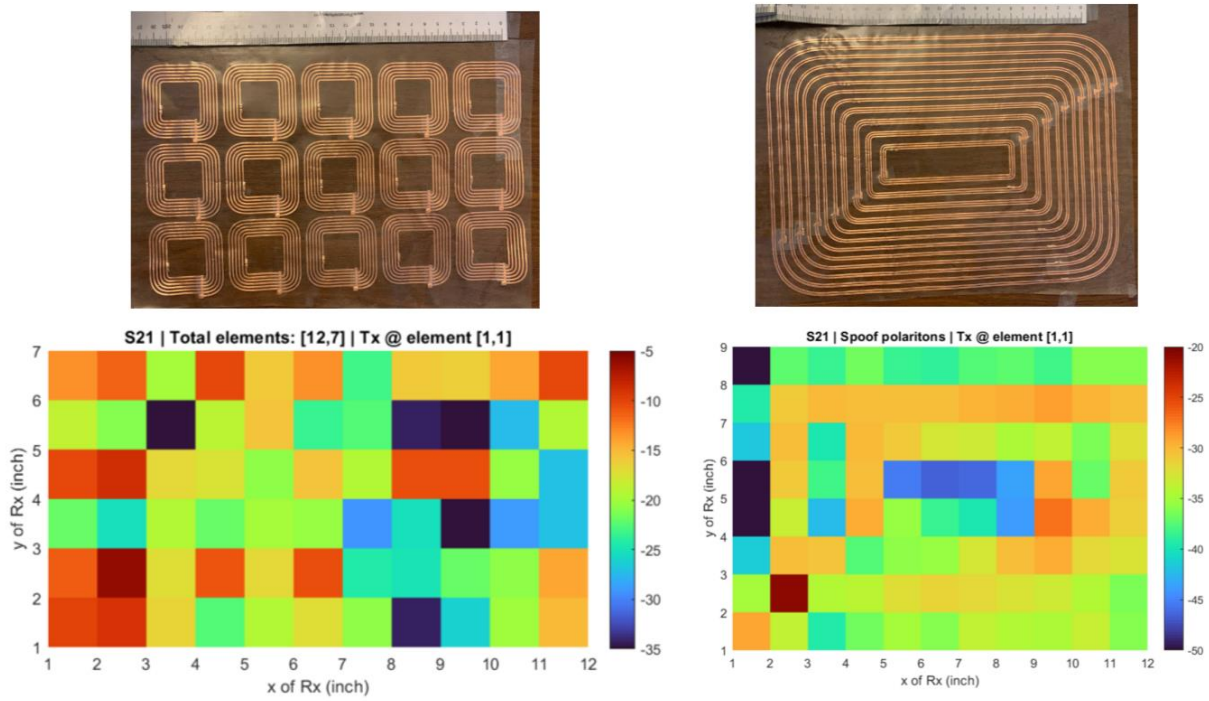

Fig. 47. Transmission profile comparison among 2D lattice and nested MI arrays for extended surface coverage.

The hybrid approach can be readily developed to be utilized as NFC-compliant charging mats to facilitate human interface with compatible battery-free peripherals (Fig. 48).

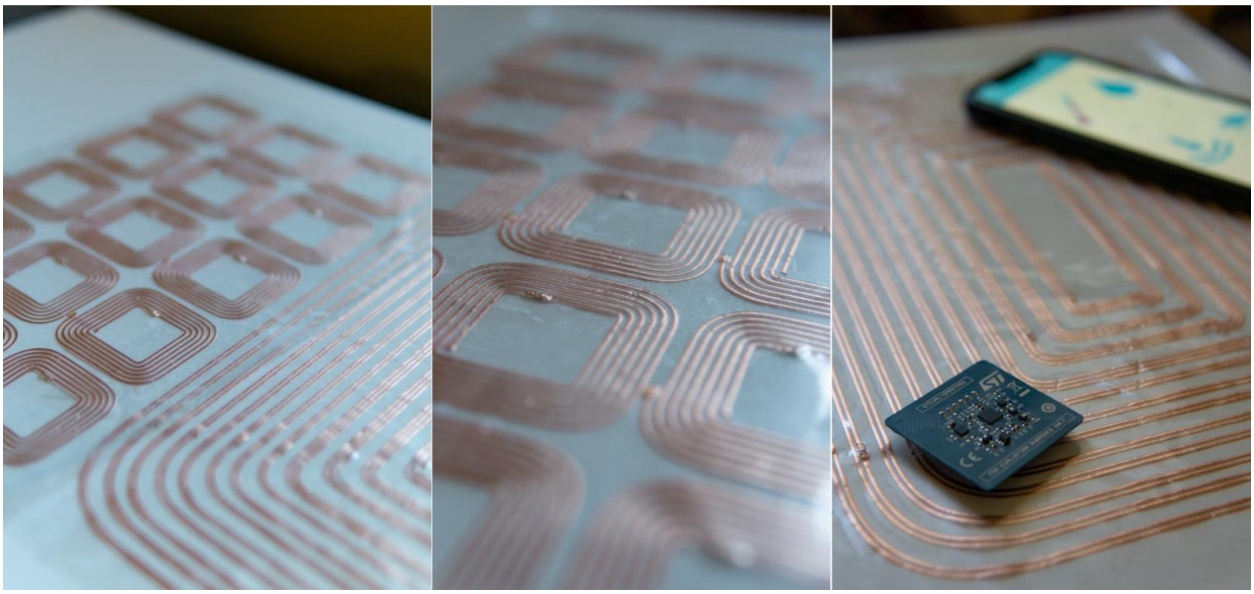

Fig. 48. Hybrid MI link across a surface area.

3. SKIN PATCH METAMATERIAL CHANNELS

3.1. Introduction

Here, we report waterborne, biocompatible epidermal skin patches to enable wireless power and data transfer on the human skin and across various body areas within a very diverse environmental setting spanning from dry indoors to underwater outdoors. This BAN is based on a chain of magnetically coupled resonators that exhibits artificial nearfield wave propagation across the resonator array known as the magneto-inductive (MI) metamaterials. Our maximally bio-friendly strategy introduces a new metamaterial geometry and paint-on-skin silver flake-based ink to achieve balance between electrical conductivity, mechanical stretchability and flexibility. The higher conductivity and mechanical stability with nontoxic polymer binders is achieved by shifting from solvent-based to waterborne paint, in addition to utilizing silver over carbon flakes[80], [81]. These epidermal patches are readily transferred onto the skin and link through NFC compatible battery-free electronics by enabling nearfield electromagnetic wave propagation across the metamaterial to different body areas. Easy fabrication approach and biocompatible nature of the introduced ink establishes an on-demand yet seamless communication between untethered battery-free sensors and an active controller (such as water-resistant smartwatches with growing battery capacities) and span through nearby people and objects to facilitate human interaction with cloud-assisted electronics.

3.2. Multi-environment Network Design

MI metamaterials are suitable candidates for near field electromagnetic (EM) waveguide applications, as they allow propagation across a chain of magnetically coupled resonant structures within a particular passband[82], [83]. Additionally, these metamaterials demonstrate highly engineered mechanical and spectral EM properties, allowing for efficient power transfer and data reception[55]. Due to insensitivity of the magnetic interconnections between the resonators to electrical permittivity of the surrounding environment, the MI metamaterials exhibit a notable degree of spectral immunity to changes in the background media (Fig. 49).

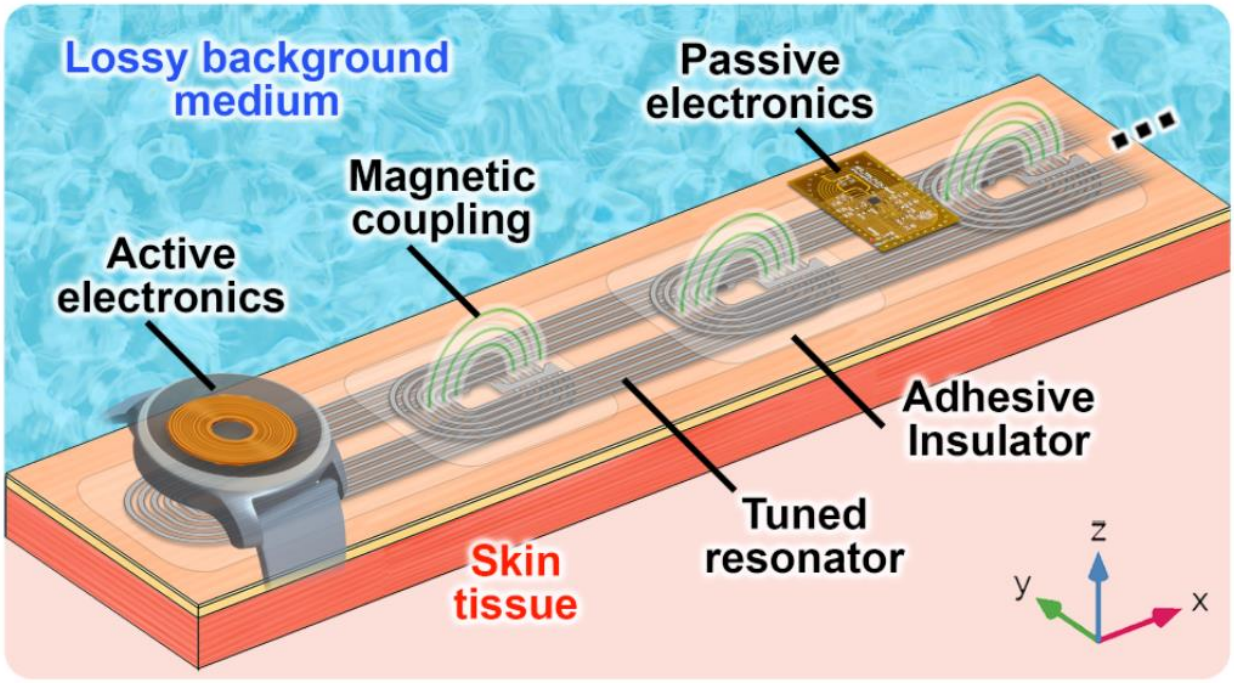

Fig. 49. MI waveguides for multi-environment wireless body area networks. Fig. 49Schematic of MI wave propagation across magnetically-coupled epidermal skin patches exposed to lossy unpredicted environments.

Here, we demonstrate epidermal MI metamaterial networks to realize a BAN that is directly placed on the skin and functions seamlessly and regardless of the user's choice of clothing. Our network is formed by arrays of magnetically coupled resonators that consist of a multiturn planar loop with a self-inductance and ohmic resistance of L and R, respectively. The resonance properties of this building block are determined by the effective capacitance which consists of the structural stray and a discrete tuning component (C). The stray capacitance forms in between the multiturn loops through the background environment ($\mathrm{C_B}$) and skin ($\mathrm{C_S}$), and relates to the coil's real estate. The lossy dielectric characteristic in background and skin media is represented by $\mathrm{G_B}$ and $\mathrm{G_S}$, respectively. This lossy behavior, however, can be controlled through encapsulating the loop traces within a thin non-conductive insulator to block the fringing electric currents, and is modeled by an equivalent insulating resistance ($\mathrm{R_{INS}}$) series with the stray components (Fig. 50).

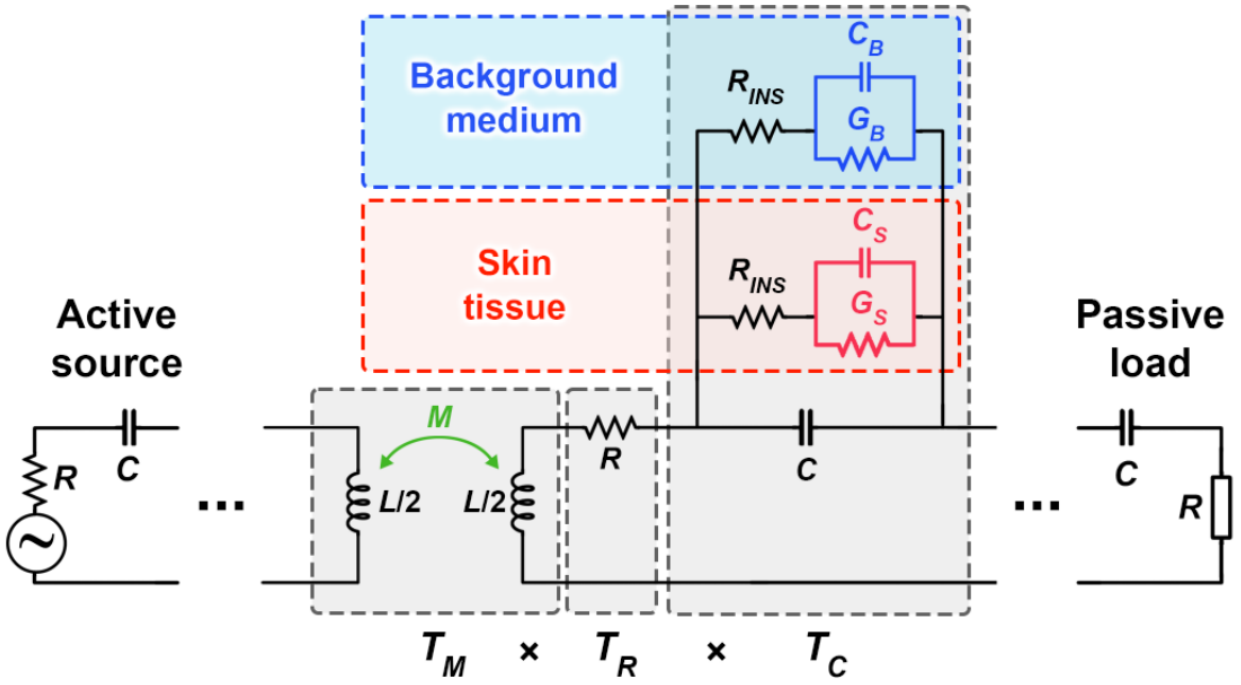

Fig. 50. Equivalent circuit of the resonator chain incorporating the background medium and insulator characteristics effect.

Due to the parasitic nature of the stray electric fields, we incorporate a lumped surface mount capacitor to dominate the stray capacitance (larger in an order of magnitude) to achieve a steady resonance insensitive to skin proximity. This allows to tune the multiturn loop resonance into the NFC band's frequency of 13.56 MHz. This MI array can be excited through a magnetically coupled external source, to enable flowing sinusoidal time-dependent electric currents with an angular frequency of ω in the n^{th} loop resonator (ranging from 1 to N). The encapsulated magnetically coupled resonator-coils are inductively coupled to the closest neighbor resonator with the mutual coupling of $M = k \times L$ where M and k represent the mutual inductance and coupling factor, respectively. Here, neighbor coils are positioned with small overlap (distance of d_c) to realize a sufficient magnetic coupling. Traditionally, the dispersion characteristics of MI metamaterials have been calculated through the resonator impedance, followed by calculating the n^{th} inductor current in a linear array represented by:

$$I_n = I_1 e^{j\phi_1} e^{-j\gamma(n-1)d_c} \quad (4)$$

where ϕ_1 and $I_1$are determined by the boundary and excitation conditions. Here, we utilize a new approach to systematically derive the dispersion profiles of complex resonator structures via breaking the complex equivalent circuit of each resonator (unit cell) into sub-models whose transfer (known as ABCD) matrix model are simply cascaded:

$$T_{cell} = \begin{bmatrix} A_{cell} & B_{cell} \\ C_{cell} & D_{cell} \end{bmatrix} = T_M \times T_R \times T_C \tag{5}$$

The resonator's sub-models transfer matrices here include T_M, T_R, and T_C that respectively represent the mutual inductive coupling, multiturn loop Ohmic (DC) resistance, and tuning capacitor within the lossy environment. The dispersion characteristics of the array of insulated coils is therefore extracted by deriving the eigenvalues of the unit cell's transfer matrix [84] with regard to geometrical distance between neighbor cells:

$$\gamma = \frac{1}{d_c} \times \cosh^{-1}\left(\frac{A_{cell}+D_{cell}}{2}\right) \tag{6}$$

Here, $\gamma = \beta + j\alpha$ is the propagation constant (β as the phase and α as attenuation constants). The propagation constant of the proposed encapsulated MI metamaterial in free space and lossy background media (at the NFC band) is analytically modeled and compared with that of the conventional far-field propagation (at Bluetooth and Wi-Fi band)[85]. Interestingly, the magnetic nature of the coupling in the MI metamaterials offers significantly lower sensitivity to the lossy surrounding environment represented by the electric conductivity of σ_B (Fig. 51).

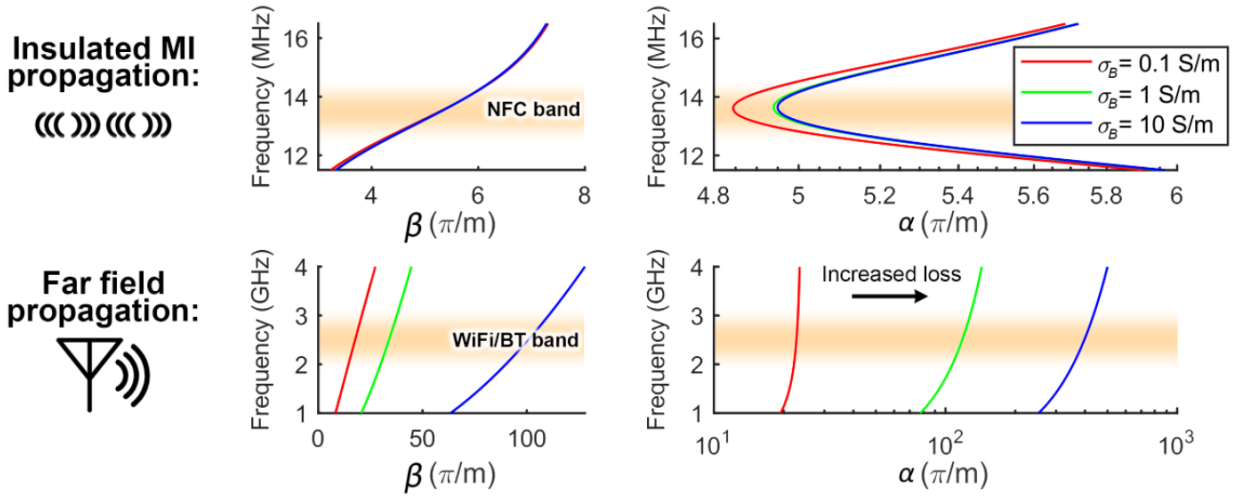

Fig. 51. Dispersion diagrams of nearfield MI against far field propagations. In contrast to conventional far field propagation, MI propagation exhibits little to no sensitivity to lossy background media.

The bandwidth and attenuation at the passband which is directly correlated with the metamaterial transmission profile can be engineered by adjusting the coupling factor and equivalent encapsulation insulation (Fig. 52).

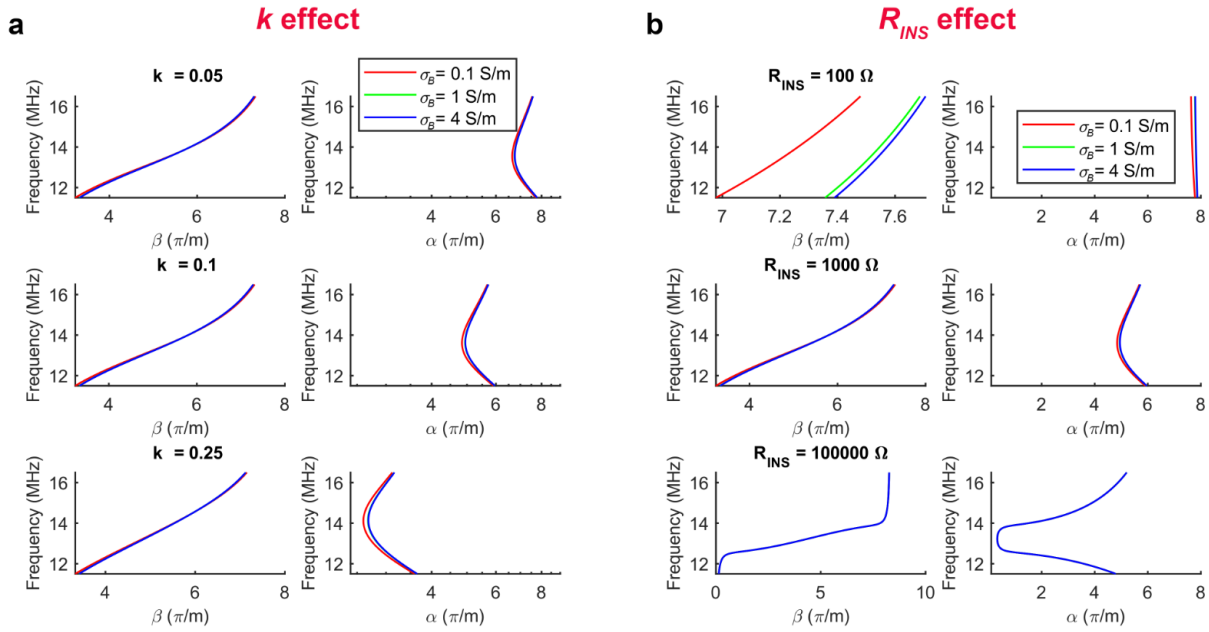

Fig. 52. Comparison of dispersion diagrams for variable background media conductivity (σ_B), mutual coupling factor (k), and insulator's effective resistance (R_{INS}) which depends on the area exposed to lossy medium in addition to the insulator's conductivity.

The low-loss propagation characteristics of this structure demonstrated at the tuned pass band allows untethered links within lossy environments, ultimately enabling an amphibious wireless power and signal transmission (Fig. 53).

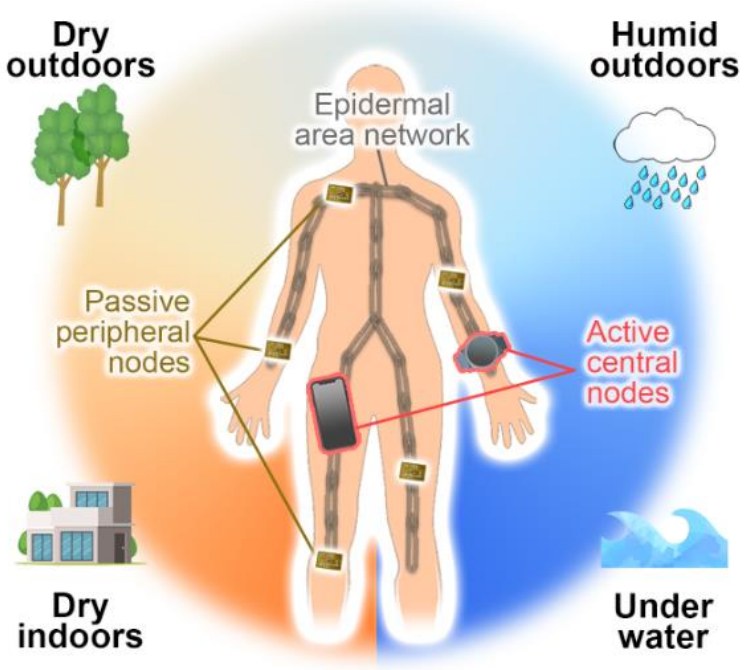

Fig. 53. This makes MI-BAN a suitable candidate for multi-environment area networks, spanning consumer wireless communication and powering from lossless dry to lossy underwater environments.

These discrete resonators, however, have been traditionally linked by magnetic coupling. To demonstrate maximal mechanical stretchability across the MI metamaterial pathway, we introduce conducted-coupling of neighboring coils through a serpentine structure with a trace geometry that is optimized for frequently bending joints (Fig. 54).

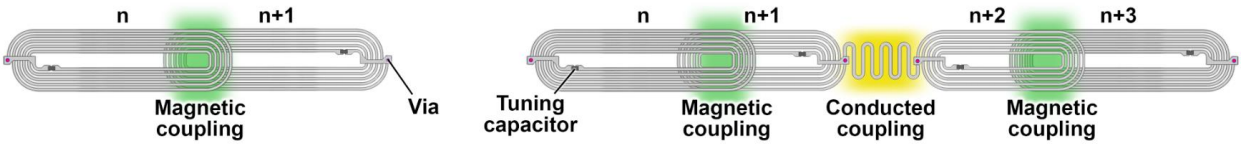

Fig. 54. Rectangular resonators can be connected through wireless magnetic or wired conducted coupling (with serpentine structure) to enable maximal mechanical stretchability at frequently bending joints.

The dispersion properties of these resonators are systematically analyzed by dividing the structure into sub-geometries and compared in Fig. 55.

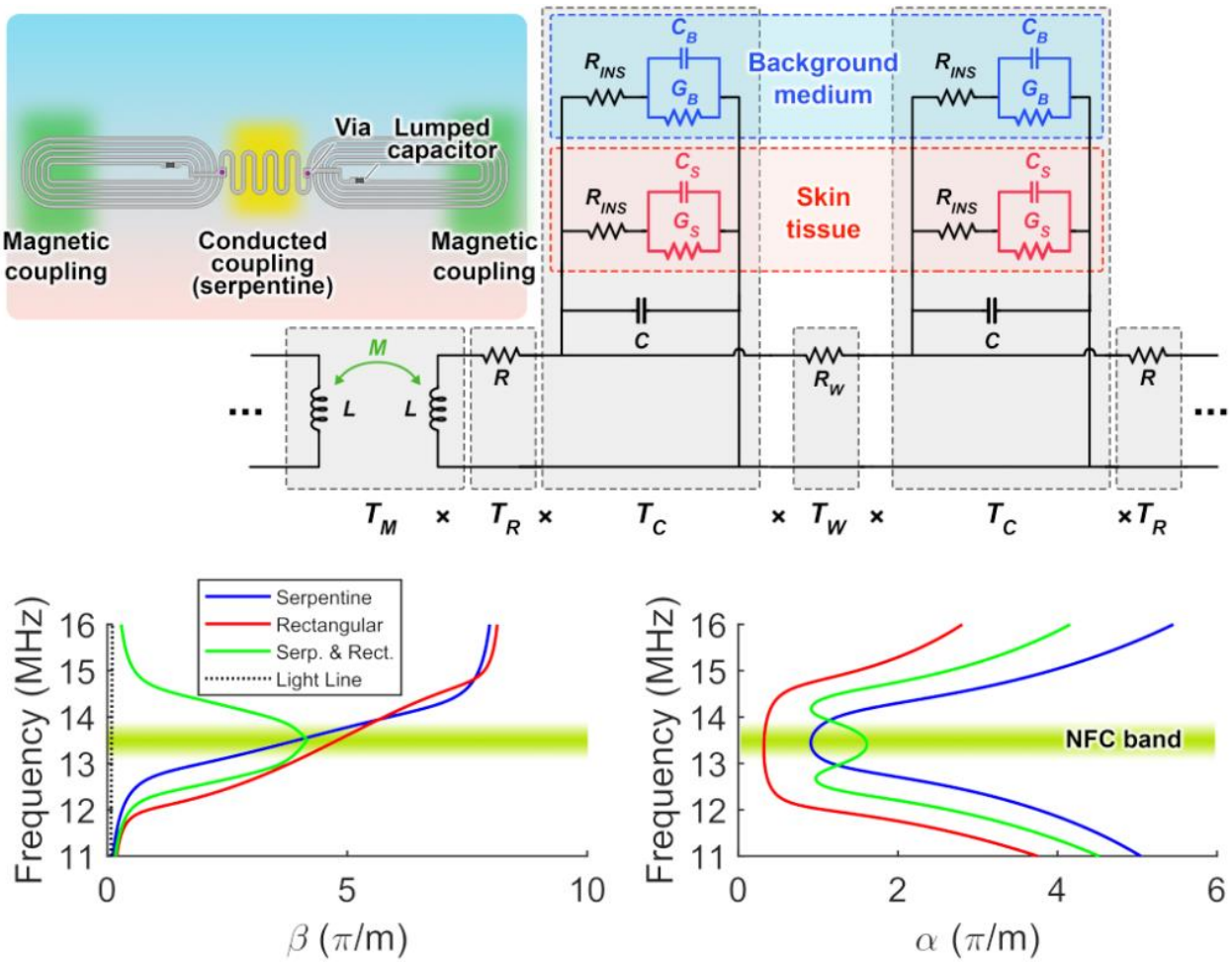

Fig. 55. The dispersion properties of the trace-coupled resonators are modeled by breaking the unit cell resonators into cascaded ABCD transfer matrices and calculating the eigenvalues to obtain the dispersion diagrams. The insulator is assumed to possess sufficient electrical resistance (R_{INS}>10 kΩ) to block the stray electric fields from leaking currents through the skin and lossy background media. This can be practically achieved by utilizing a thing encapsulation.

The coil geometries and tuning capacitors designed in this study are demonstrated in Fig. 56.

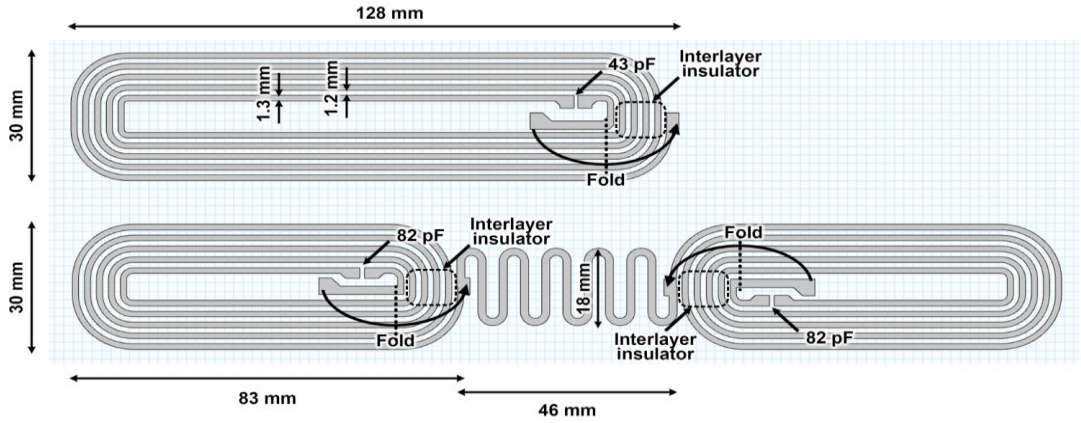

Fig. 56. The coil geometries and tuning capacitors for magnetic- and conducted-coupling structures resonating at NFC carrier frequency of 13.56 MHz.

3.2.1. Rectangular Shaped Resonators

The entire resonator's ABCD matrix is derived by cascading the sub-model matrices shown in Fig. 50. These matrices are each modeled via MATLAB's Symbolic Math Toolbox and are derived as follows:

$$T_{cell} = \begin{bmatrix} A_{cell} & B_{cell} \\ C_{cell} & D_{cell} \end{bmatrix} = T_M \times T_R \times T_C \tag{7}$$

$$T_M = \begin{bmatrix} \frac{L}{2M} & j\omega\left(\frac{L^2}{4M} - M\right) \\ \frac{1}{j\omega M} & \frac{L}{2M} \end{bmatrix}, T_R = \begin{bmatrix} 1 & R \\ 0 & 1 \end{bmatrix}, T_C = \begin{bmatrix} 1 & \left(\frac{1}{Z_S} + \frac{1}{Z_B} + j\omega C\right)^{-1} \\ 0 & 1 \end{bmatrix}, \tag{8}$$

where $Z_S = R_{INS} + (G_S + j\omega C_s)^{-1}$, and $Z_B = R_{INS} + (G_B + j\omega C_B)^{-1}$.

3.2.2. Complex Resonator Geometries

3.2.2.1. Conducted coupling of two neighbor coils

Similar to magnetically coupled resonators, the entire unit cell's transfer matrix here is calculated using the equivalent circuit shown in Fig. 55. Here, T_M is slightly different than the previous case as due to the nature of conducted coupling, each multiturn loop is entirely coupled to its neighbor loop on one side only. Here, R_W represents the Ohmic loss of the serpentine wired coupling.

$$T_{cell} = \begin{bmatrix} A_{cell} & B_{cell} \\ C_{cell} & D_{cell} \end{bmatrix} = T_M \times T_R \times T_C \times T_W \times T_C \times T_R \tag{9}$$

$$T_M = \begin{bmatrix} \frac{L}{M} & j\omega\left(\frac{L^2}{M} - M\right) \\ \frac{1}{j\omega M} & \frac{L}{M} \end{bmatrix}, \tag{10}$$

$$T_R = \begin{bmatrix} 1 & R \\ 0 & 1 \end{bmatrix}, \tag{11}$$

$$T_C = \begin{bmatrix} 1 & 0 \\ \frac{1}{Z_S} + \frac{1}{Z_B} + j\omega C & 1 \end{bmatrix}, \tag{12}$$

$$T_W = \begin{bmatrix} 1 & R_W \\ 0 & 1 \end{bmatrix}, \tag{13}$$

where Z_S and Z_B are identical to previous case.

3.2.2.2. Magneto-Capacitive Metamaterials

Similar to conducted coupling of MI arrays, we may replace the serpentine structure by appropriate series capacitances to maximize the bandwidth (Fig. 57).

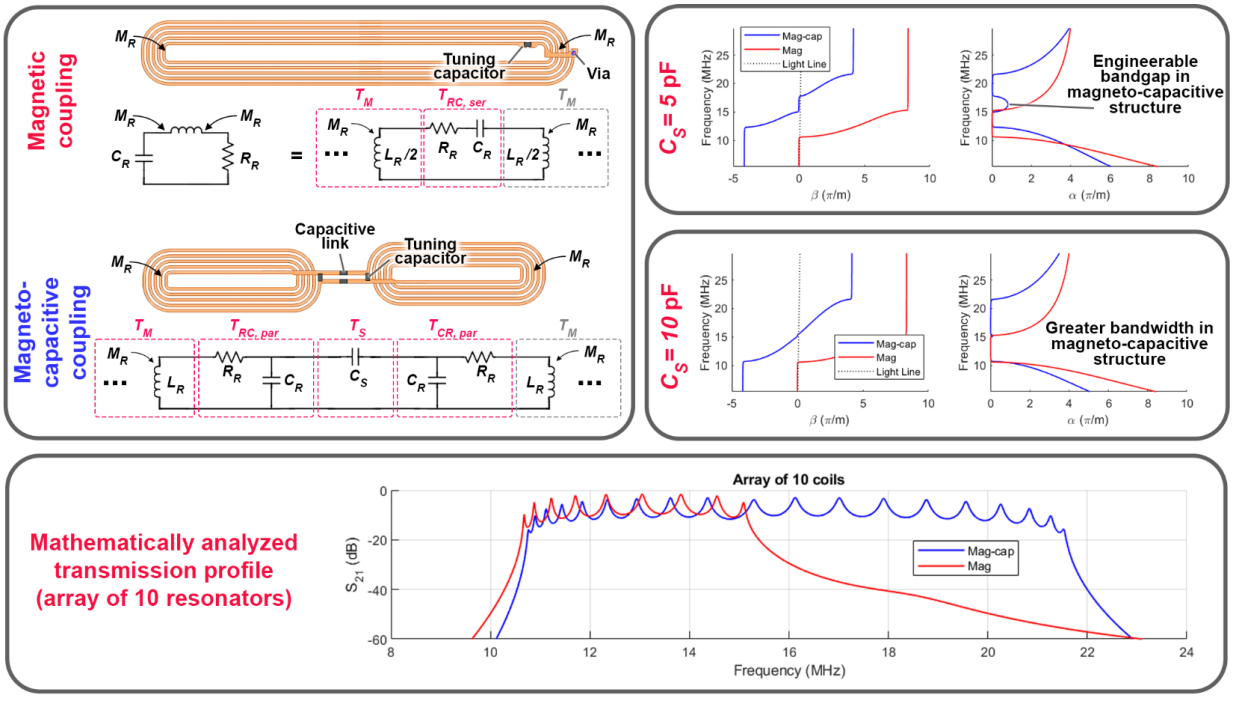

Fig. 57. Wideband magneto-capacitive resonator arrays

3.3. Stretchable Network Fabrication

Lack of stretchability in flexible copper-based printed circuit boards renders them unsuitable for biomedical applications, particularly when applied in epidermal settings. In contrast, silver conforms to various types of stretching surfaces including living tissues and/or a wide range of textiles[86]. Although conductivity of the silver-based ink can be readily enhanced by increasing concentration of silver flake, this results in a lower flexibility and weaker stretchability properties[87], [88]. Additionally, these inks are conventionally hindered by significant loss of conductivity under normal strain[89].

Traditional ink-jet printed silver inks require high temperature sintering to be conductive. Here we introduce an alternative waterborne-based silver ink formulation with low curing temperature to balance the tradeoff between conductivity and stretchability. Our stretchable conductive ink consists of commercially available multipurpose liquid glue as a matrix, silver flakes as a conductive agent, glyceryl triacetate as a plasticizer, and borax as crosslinkers sintered in low temperature. In contrast to solvent-based conductive inks, the waterborne nature of the ingredients offers biocompatibility, faster drying time, adhesion to a wide range of substances including skin and polymer substrates. Interestingly, these silver ink-based circuit traces bond with metallic pins of electronic components and eliminates the need for brittle solder connections that often fail in highly flexible settings of wearable applications. Additionally, the solder-free curing process enables use of circuit board substrates with excellent mechanical flexibility that often possess sensitive thermal characteristics[90].

Elmer's Glue-All Multi-Purpose Liquid Glue was used as a water-based polymer matrix of polyvinyl acetate (PVAc). Silver flakes (SYP-981) with a mean particle size of around 10 μm were purchased from AG PRO Technology, Taiwan. Glyceryl triacetate (GTA, 99%), sodium tetraborate decahydrate (borax, 100 %), and acetic acid were purchased from Alfa Aesar Chemicals, Honeywell Fluka Chemicals, and J.T.Baker, respectively. SYLGARD®184 based polydimethylsiloxane (PDMS) was purchased from Merck KGaA. All chemicals, solvents, and reagents were analytical grade. Deionized water (DI water) was used in all experiments.

The planar coil designs (see Fig. 56) were laser cut on a vinyl sheet which was used as a stencil placed on a thin PDMS sheet. Next, the silver ink was applied over the stencil, which was then removed to develop the coil pattern. Following this step, the surface mount tuning capacitor was placed on the dedicated area, and the coil batch was pre-cured in the oven. After the initial curing, the ends of the multiturn loop were connected by bending one of the coil ends over an insulating interlayer. The overlapping ends were then connected by an additional drop of silver ink followed by post curing (Fig. 58).

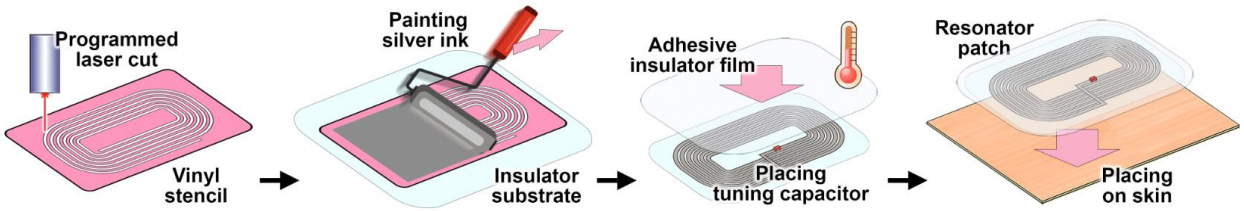

Fig. 58. Mechanical and electrical stability of the resonators. Fabrication of stretchable silver ink-based resonators and translation to skin.

For the preparation of pre-silver ink, PVAc (Glue-All= 41.3%), GTA, and acetic acid were first mixed by a mixer (THINKY MIXER AR-100) at 1000 rpm for 30 seconds. The acetic acid here provides a weak acid environment to prevent the ink from curing. Next, the silver flake powder was added into the adhesive agent with silver nanowires solution, which increases the conductivity and elongation of the ink, and then mixed for 3 minutes. For the final silver ink, borax (5% in water, 1% of PVAc + GTA) was added into the pre-silver ink and mixed for 3 minutes (see Fig. 59).

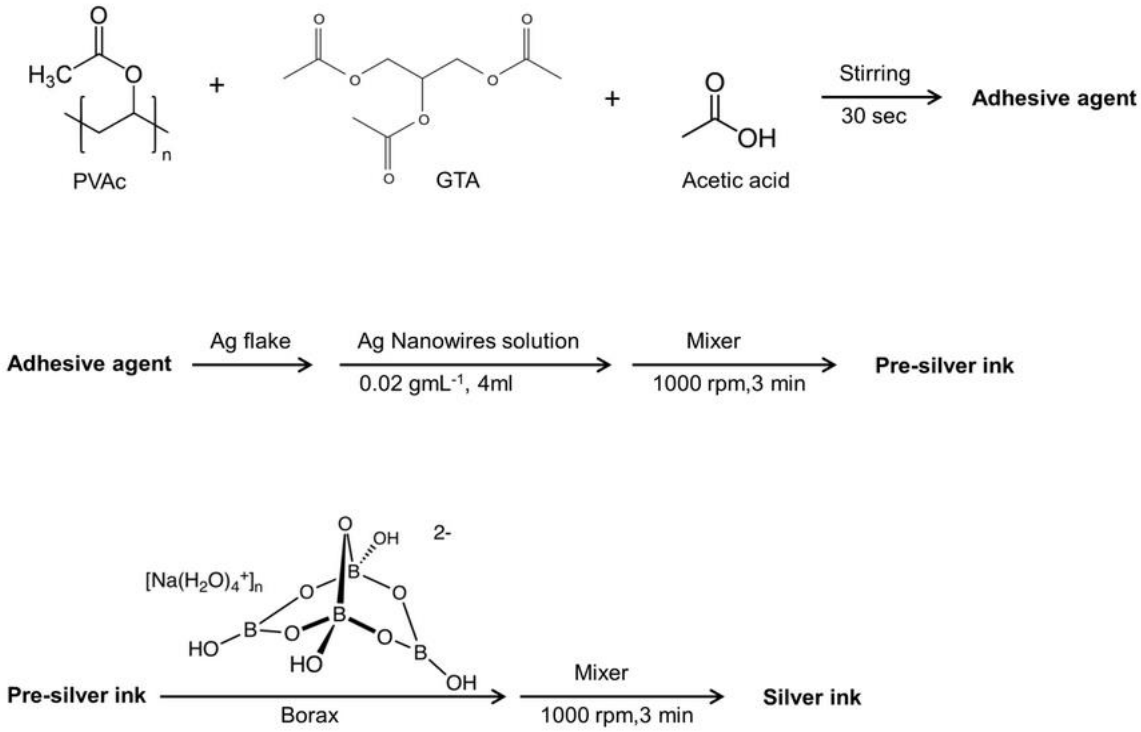

Fig. 59. The waterborne-based silver ink synthesis process.

The designed patterns were laser-cut (Versa laser, 1060 nm) onto disposable adhesive vinyl masks adhered to the desired Polydimethylsiloxane (PDMS) membrane substrate. After the conventional coating process, applying the silver ink over the stencil, the mask was then removed to reveal the coil pattern. The resonator coil traces were then developed by peeling the mask. Then, the surface mount tuning capacitor (805 package, 5% tolerance, 50V rating, Murata Electronics) was placed on the dedicated area to make contact with the uncured silver ink. Next, the coil batch was cured in an oven under 100^{o}C for 30 min. This resulted in a 9.5 cm×2 cm×0.1 cm stretchable resonator on a 0.5mm thick PDMS substrate. Finally, the stackup was sealed by transparent medical grade 3M Tegaderm film.

In order to prevent direct contact with the background medium, a thin insulating PDMS sheet was used to encapsulate the coil. The transmission profile (S_{21}) of a 90 cm long magneto-inductive array was then measured under various PDMS encapsulation thickness and background environment (lossless dry and 35 g/L NaCl to mimic ocean water salinity). The insulated array was submerged in the lossy background and transmission profiles were measured using a vector network analyzer (Fig. 60).

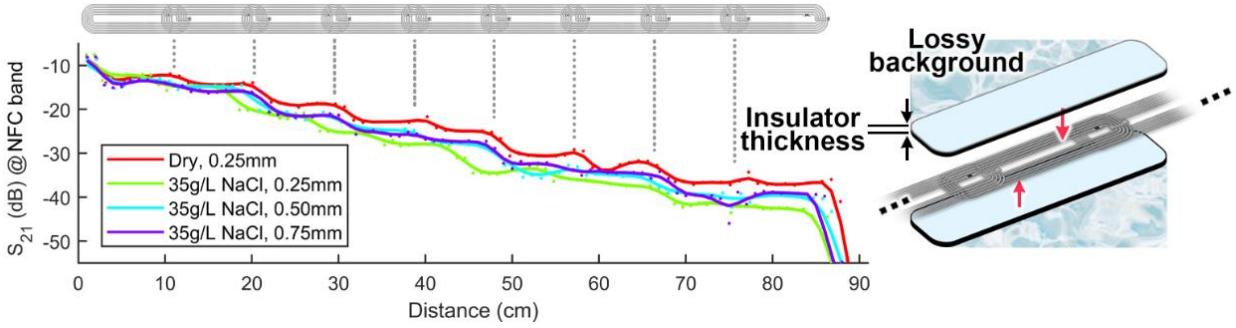

Fig. 60. Transmission profile of the MI array measured under various insulator thickness and background medium loss.

The electrical conductivity of the silver flake-based ink was measured under an increasing strain (until failure) exhibiting resistance stability under applied strain which makes it suitable for use in epidermal applications (Fig. 61).

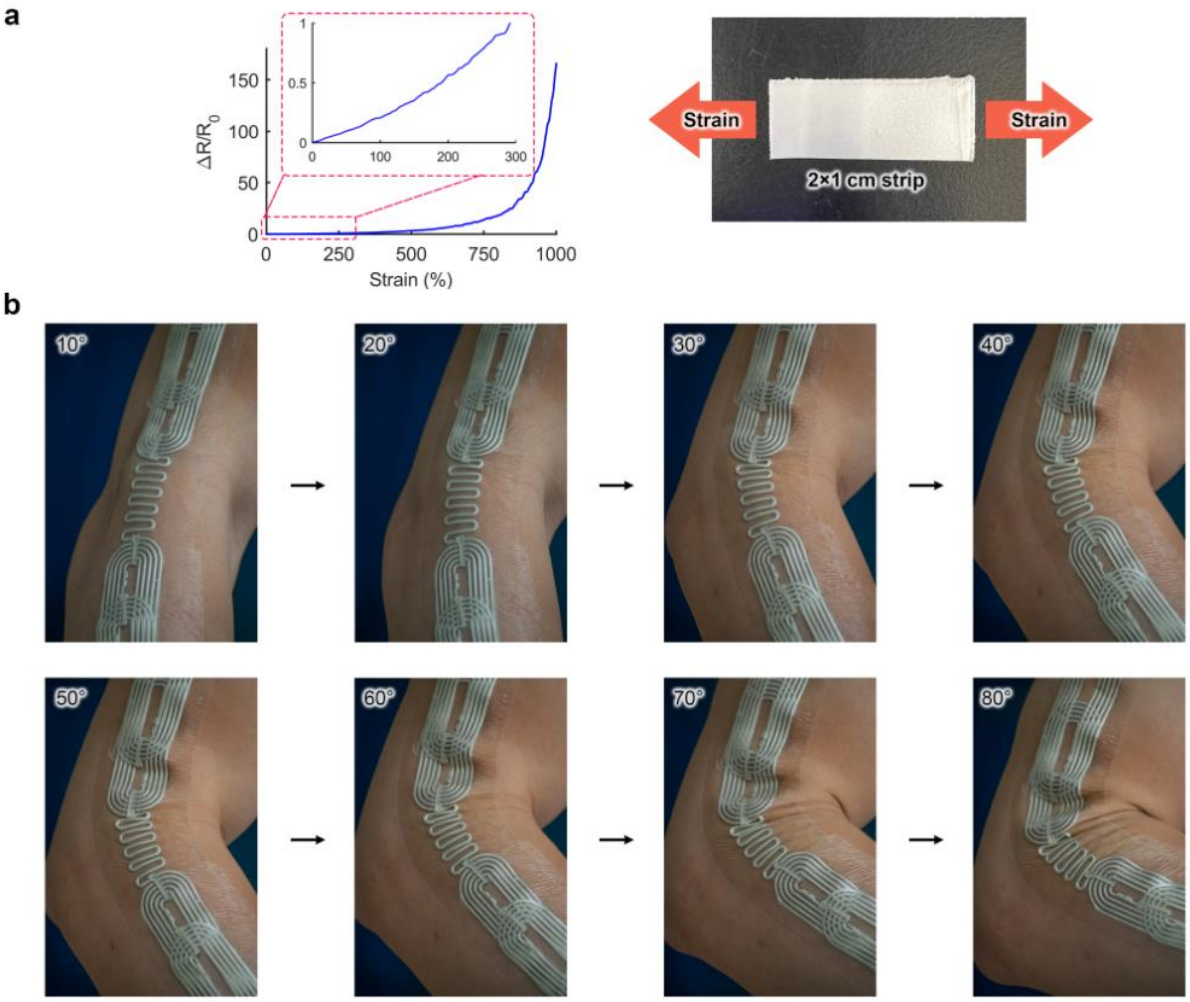

Fig. 61. Stretchability of the (a) strip-shaped and (b) resonator geometry during bending phases. Utilizing the trace-coupled resonator (through the serpentine structure) enables absorbing the bending strain and applies minor strain to the coils.

Additionally, the resonance characteristics (including the frequency and quality factor) of the designed rectangular coil was measured under normal strain (Fig. 62) which demonstrates a hysteresis-free profile under up to 15% strain to represent a normal tissue bending.

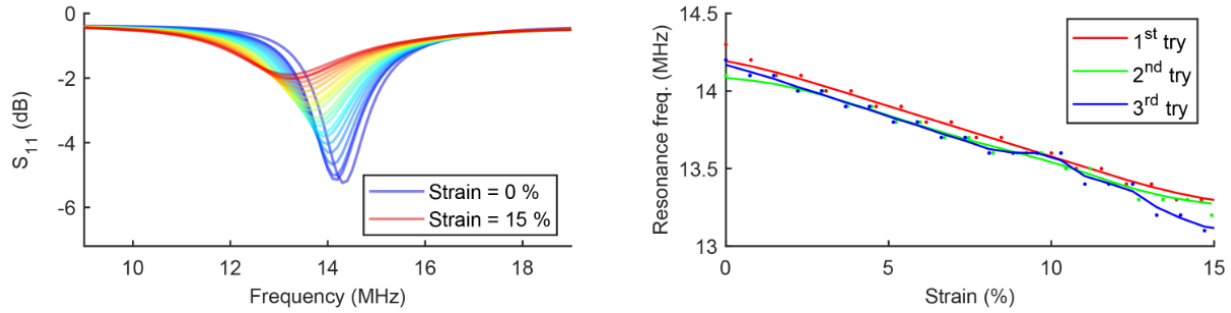

Fig. 62. Resonance properties of the silver ink-based coil under normal strain in a dry background environment on a 0.5mm thick PDMS substrate. Sensitivity and repeatability of the resonant coil under normal strain.

The coil structure failed at a breaking point near the center of its length while under 25% strain. The resonant structure, however, did not fail at the conjunction of the tuning capacitor and the coil trace for up to 100% applied strain (Fig. 63).

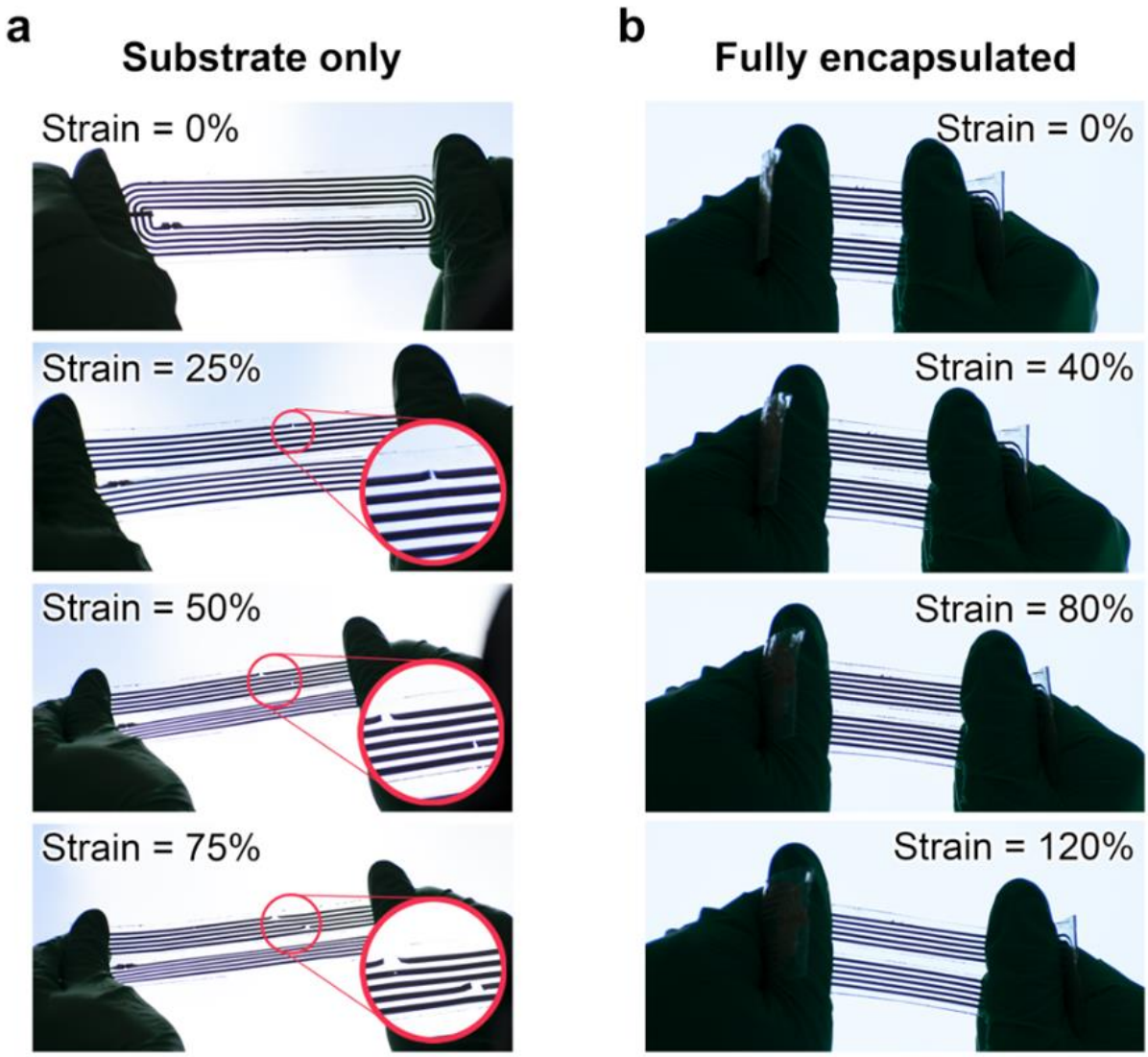

Fig. 63. Assessing the stretching durability of the ink under two conditions: (a) without PDMS encapsulation, the tuning capacitor junction did not fail for up to 100% strain. The top insulator is removed to show the failure points.; and (b) with complete PDMS encapsulation. In both cases, a 0.5 mm thick PDMS substrate was employed, along with PDMS top sealing in the fully encapsulated scenario. The comprehensive PDMS encapsulation significantly enhances the stretching threshold, increasing it from below 25% to above 120%.

For reliability purposes, flexibility of the skin patch was tested by measuring the resonance characteristics (S_{11}) under up to 10000 full bending (0 to 180°) cycles with no major changes in the central frequency (Fig. 64).

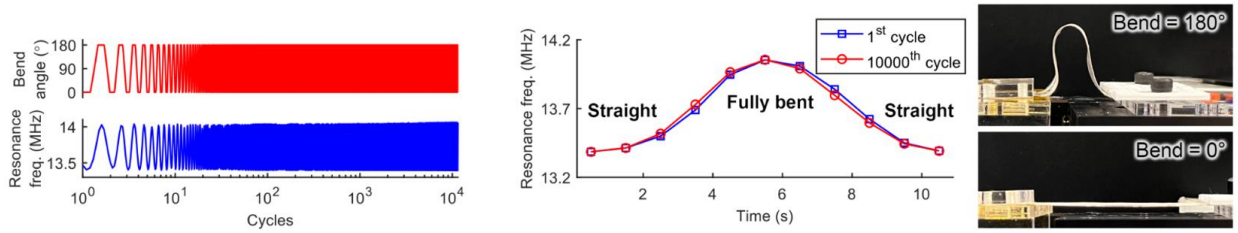

Fig. 64. The coil exhibits no major difference between the resonance frequency profile of the first and last bending cycles.

The electric conductivity of the silver ink-based strip (2 cm×1 cm on a TPU substrate) was measured by a four-point probe meter (Loresta-GP MCP-T600, Mitsubishi Chemical). Strain was applied by a motorized linear actuator (Zaber X-NA08A25-E09), and then strained at 20 $\mu m.s^{-1}$ until pasting their electrical strain-to-failure point (breaking point of up to 900% strain). During the straining process, resistance changes were continuously recorded using a precision LCR meter (Keysight Technologies E4980AL). Similar setup was used to measure S_{11} resonance properties while recording the reflection coefficient seen from an aligned reader antenna close to the coil.

The conductive ink properties of this study is compared with state-of-art in **Table 2**.

Table 2. Landscape of available conductive inks.

Method	Waterborne silver flake (this work)	Solvent based silver ink[23], [24], [91]	Solvent based copper flake[27]	Carbon nanotube ink[26]	Graphene ink[25], [92]	Conducting polymers[80]
Bio-compatibility	Yes	No	Based on solvent	No	No	Yes
Conductivity	Excellent (10^6 S/m)	Excellent (10^6 S/m)	Marginal (10^4 S/m)	Poor (10^3 S/m)	Marginal (10^4 S/m)	Poor (10^2 S/m)
Stretchability	Excellent (> 130% when fully encapsulated)	Excellent (140%)	Poor	Marginal (70%)	Marginal (74%)	Poor (30%)
Solvents	Water based (Elmer's glue/PVAc/Silver flake)	Organic solvent based (Silver-IPA complex/formic acid reductant/ethyl alcohol/PVP)	Solvent based	Organic solvent based (HPMC/SDBS/ APTES/IUPAC)	Organic solvent based (IBA/Cyr/EC/ AChE/ethanol)	Organic solvent based (P3HT/PVDF/ APTES/PEDOT/ PSS)
Synthesis technique	Easy	Difficult	Difficult	Difficult	Difficult	Difficult
Cost efficiency	Good	Good	Good	Poor	Poor	Poor

3.4. Characterization of Stretchable Metamaterials

The epidermal BAN is formed by placing the encapsulated resonant coils directly on the skin. A thin layer (<1 mm) of 1:10 PDMS was poured into a 6 inch petri dish and allowed to partially cure for approximately 20 minutes at 80°C to create a sticky base layer for the flexible printed circuit board substrate. The flexible NFC sensor was positioned centrally on top of the sticky PDMS and covered in 2 - 3 mm of 1:10 PDMS before being allowed to fully cure at 80°C.

Adjusting the overlap between the neighboring coils (via the mutual inductance M) enables engineering the passband's bandwidth. To this aim, a coil overlapping (about 2 cm on a 13 cm long coil) would induce a bandwidth greater than 848 kHz to comply with the highest data rate incorporated in the amplitude-shift keying modulation embedded in the NFC protocol. Additionally, a larger bandwidth ensures that minor shift of resonance under bending will be covered within the exhibited passband.

The insulator thickness was chosen based on the transmission profile, to ensure minimum insertion loss (per unit of length) is achieved. This includes comparison among arrays of resonators encapsulated by 0.25, 0.5, and 0.75 mm thick PDMS sheets in dry and submerged in saline solution (35 g/L mimicking ocean's salinity). Results are added as Supplementary Fig. 65. According to this comparison, the MI channel's insertion loss at 85 cm distance (between the Tx and Rx ports) is measured 37, 39, 40, and 44 dB for dry (0.25mm thick), saline (0.75mm thick), saline (0.5mm thick), and saline (0.25mm thick), respectively. According to this study, in saline setting, a significant improvement of 4 dB is observed between 0.25 and 0.5 mm PDMS thickness, however this reduces to 1 dB between 0.5 and 0.75 mm thickness. To maintain a balance between the resonator's thickness (that directly impacts flexibility thus user comfort) and channel's transmission performance, we chose 0.5 mm thick PDMS sheets for encapsulation.

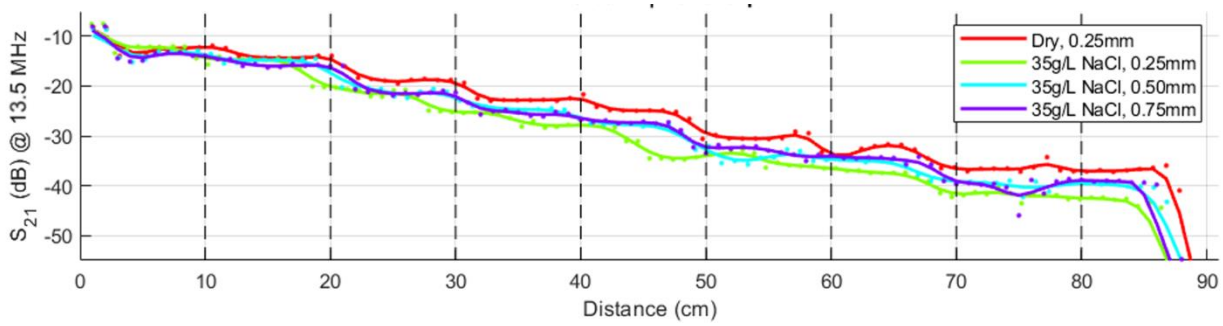

Fig. 65. Comparison between different PDMS sealing thickness on electromagentic performance of the epidermal BAN.

Here, we start forming the BAN by placing the serpentine structure on the joints (such as shoulders, elbows and knees) and continue placing the rectangular coils to create the pathway. The rectangular coils demonstrate slightly lower attenuation (as shown in Fig. 51) and thus are prioritized across the BAN. The coils were secured in place using a self-adhesive transparent film (Fig. 66). Here, the end-to-end transmission profile of a 45 cm long epidermal MI array (placed on the arm) is measured using two multiturn loop antennas (connected to a two-port vector network analyzer) under variable bending and twisting arm gestures. The passband stability during these movements warrants reliable wireless communication throughout the activity monitoring.

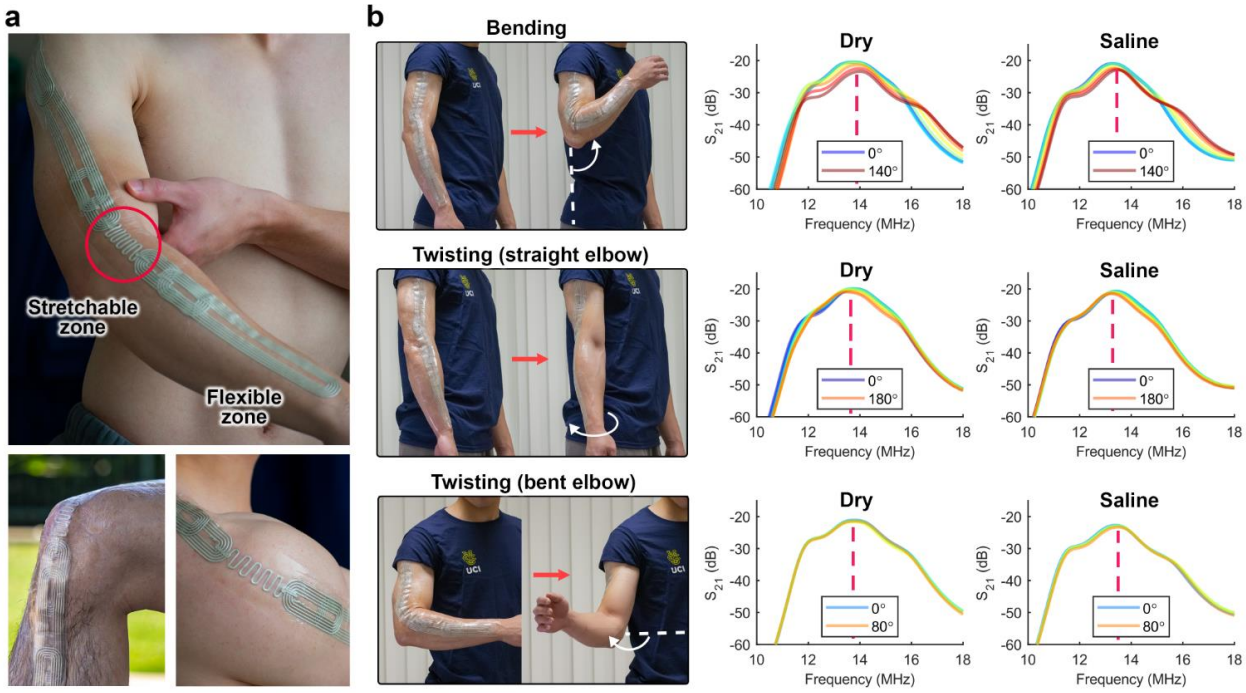

Fig. 66. Impact of body gestures on stability of the skin-integrated network. (a) MI metamaterial network transferred onto the skin with stretch-friendly serpentine structure placed on the joints. (b) Transmission characteristics of the epidermal MI BAN under various joint movements exhibit a stable electromagnetic performance under dry and saline-coated (35 g/L NaCl) background media.

3.5. Biocompatibility and Bio-Integration

The specific absorption rate (SAR) for the epidermal MI metamaterial array is simulated under lossless and lossy background media (Fig. 67). According to the NFC standard specification, the peak magnetic field emitted from the active NFC reader may not exceed 10.5 A/m. This translates to a maximum simulated SAR of 81 mW/kg averaged over the muscle volume, which is significantly lower than the industry standard of 400 mW/kg [93] at 13.5 MHz.

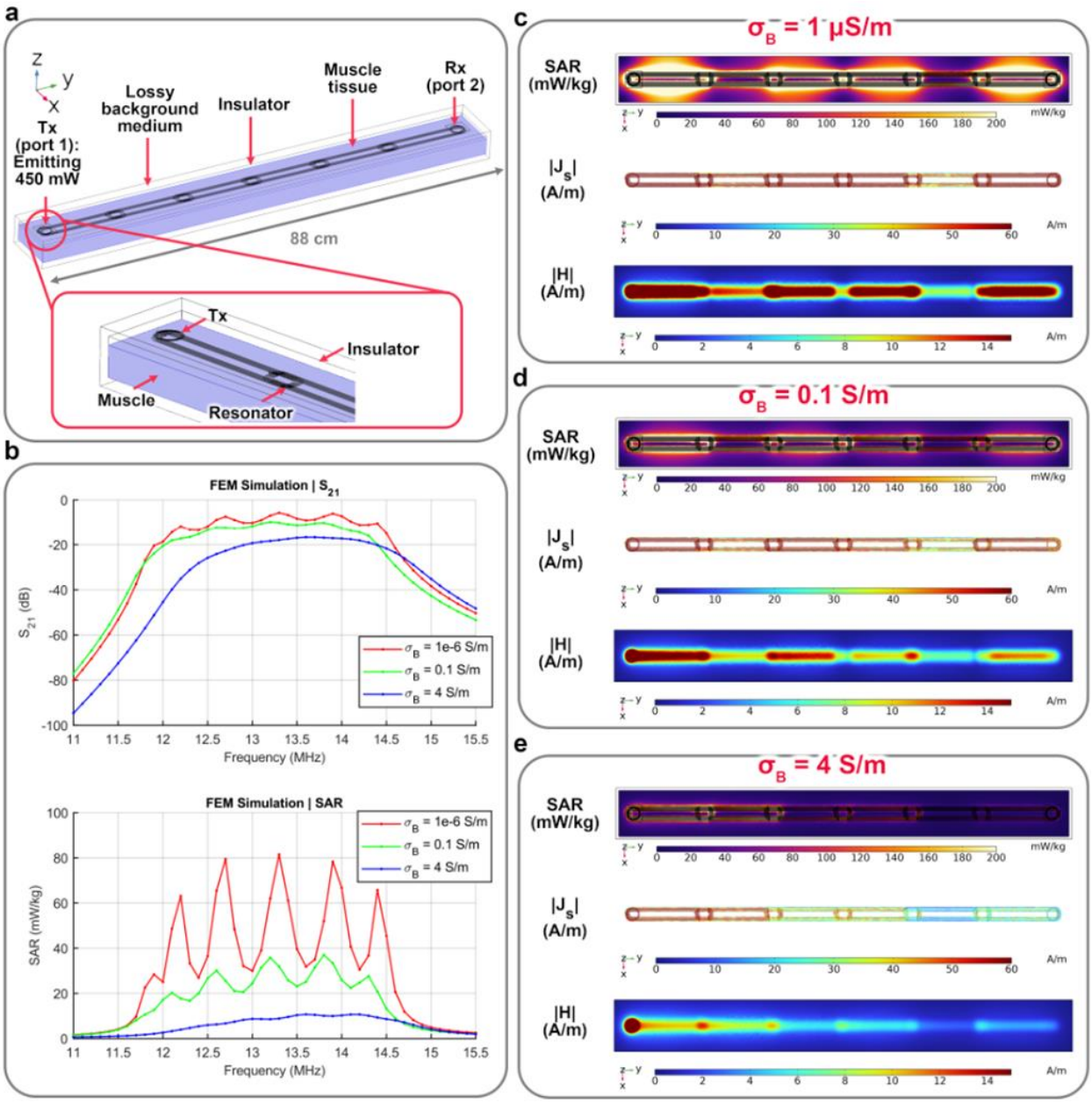

Fig. 67. Finite element method simulations demonstrating SAR and transmission in various lossy background medium settings. (a) The simulation setup includes insulated metamaterials on top of the muscle tissue and exposed to a background medium with variable conductivities (σ_B) to represent electrical loss from dry (1 μS/m) to under salty water (4 S/m) settings. The transmitter's power here is set to 560 mW to represent the maximum RF available power in the NFC reader chip here. These SAR simulations ignore NFC amplitude modulation and demonstrate the worst-case scenario because the peak emitted magnetic field of an NFC compliant device protocol may not exceed 10.5 A/m. (b) The transmission profile under various background losses demonstrates stable electrical characteristics that is significantly untied from environmental change. The SAR simulation, however, demonstrates decreased absorption rates with greater background conductivity as a larger fraction of the emitted electromagnetic power is dissipated in the lossy background medium. (c-e) Simulated SAR (shown on the skin surface), surface electric current (on the metamaterial array), and magnetic field intensity (on the skin surface) at 13.5 MHz.

3.5.1. Body Integration

Here we demonstrate the mid-range uninterrupted wireless power and data sharing mechanism through the epidermal BAN in a wide span of environments including underwater setting. We placed an array of rectangular and serpentine coils on the skin, and ultimately secured in place using transparent adhesive film. We utilized our custom designed passive sensors with integrated external strain gauges and on-board miniature loop antenna (that aligns with the BAN dimensions). Due to battery-free operation, these sensors are extremely lightweight (3 grams per board), highly flexible, and conform to the body areas, which realizes a seamless human activity monitoring without interrupting the user's normal routine. The sensors were also encapsulated for underwater usage. Additionally, the NFC reader which incorporates a miniature battery represents the only active microelectronics that supplies power to the sensors and receives sensor collected data for local or online storage. The miniature form factor of this controller enables its utilization as an NFC-enabled master node for future wearable applications such as waterproof smartwatches (Fig. 68).

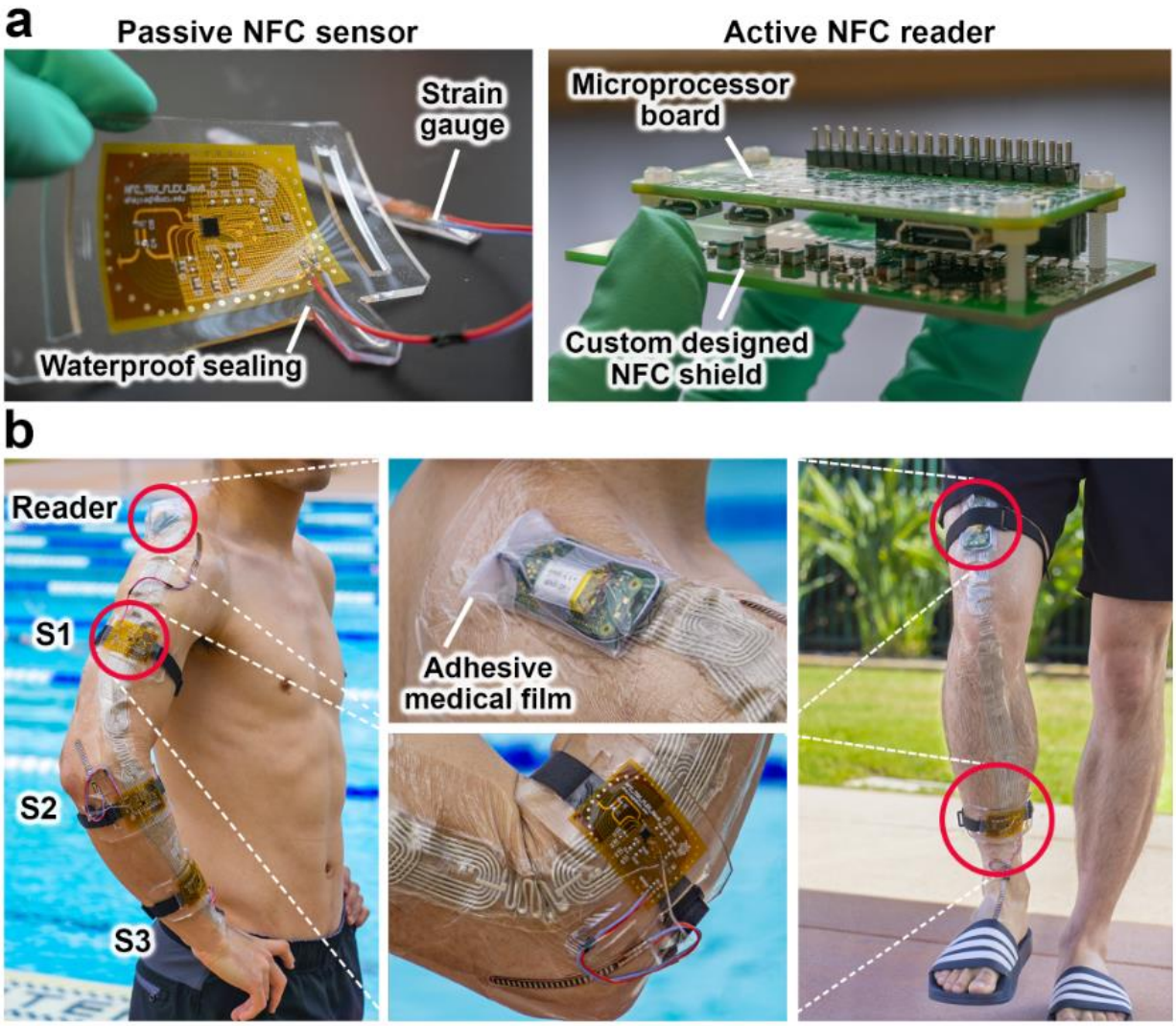

Fig. 68. Amphibius epidermal BAN functioning in a wide span of challenging environments. (a) The passive flexible sensor board with an integrated strain gauge and miniature active NFC reader. (b) Integration of epidermal skin patches on the human body to transmit wireless power from the NFC reader to the local sensors and collect motion data.

The printed circuit board layout of the custom reader and sensor boards are shown in Fig. 69.

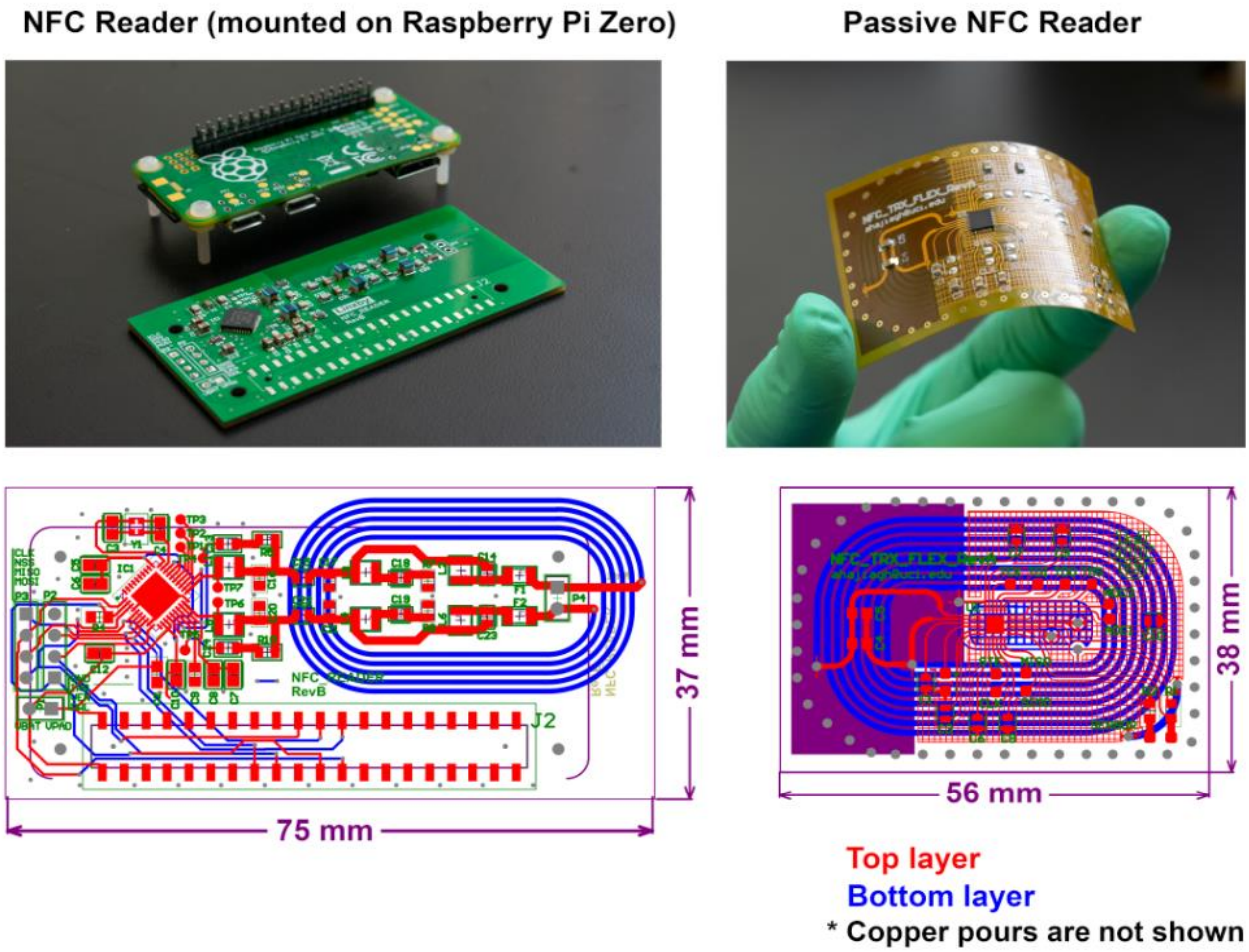

Fig. 69. Active and passive custom electronic board designs.

In addition to on-demand integration of this BAN with pre-existing NFC-enabled electronics, the nearfield propagation can be seamlessly routed along and between the epidermal and textile-integrated from factors, enabling multi-purpose applications (Fig. 70).

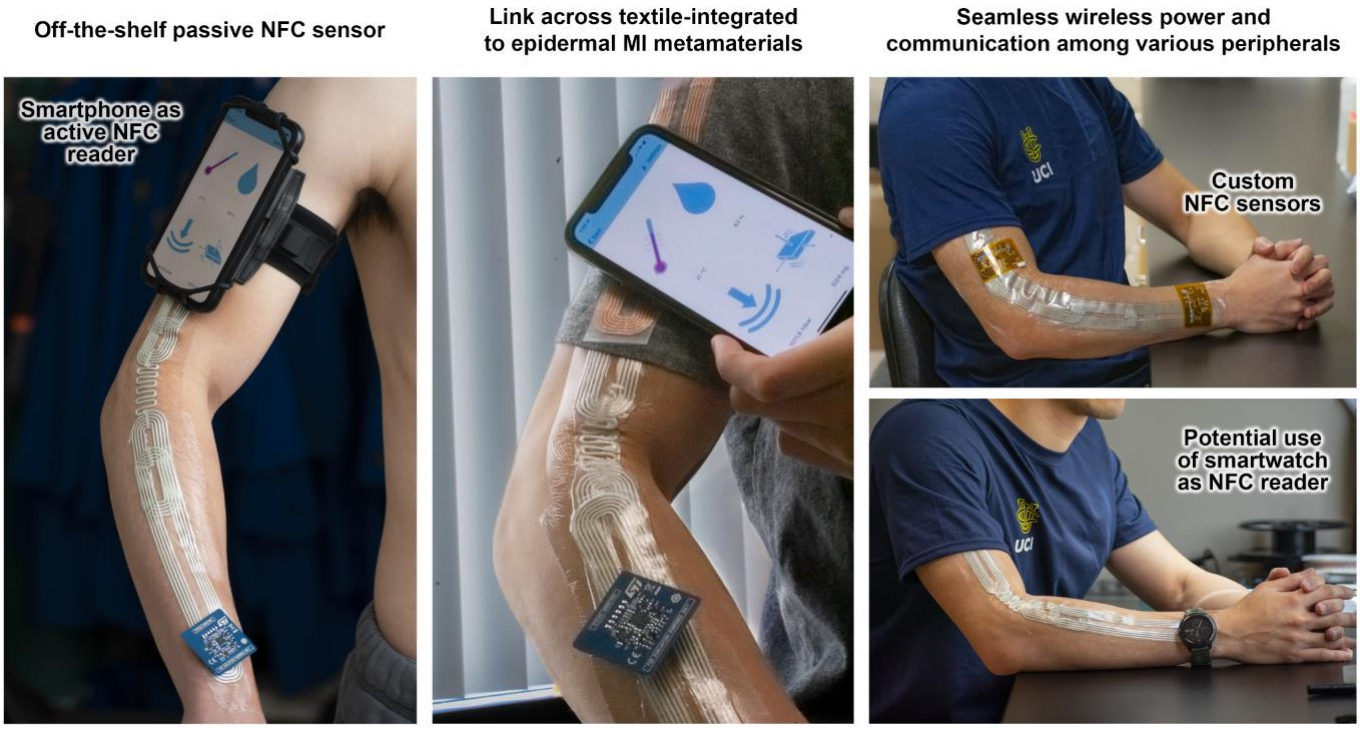

Fig. 70. The nearfield propagation can be seamlessly routed along and between the epidermal and textile-integrated from factors, enabling multi-purpose applications.

3.6. Motion Data Readout

The reader was set to collect sensor data with an overall refreshing rate of 14 Hz (equivalent to 4.66 Hz per sensor). We employed software-based time domain multiple access for seamless switching between sensing nodes. This method utilizes controlled surface propagation of magneto-inductive waves, which in contrast to wired or antenna switching schemes does not require additional multiplexing hardware. As a result, conventional NFC-enabled smartphones can operate as compatible readers. The raw digitized strain gauge values were translated to angular postures through a one-time calibration process by linearly correlating the measured sensor value to the known body angle.

The arm activity was recorded during periodic sequences of light swimming in an outdoor pool. The collected sensor data was smoothed through a real time filter and compared against video reference. To assess the wireless efficiency of the network, we measured the NFC packet reception ratio (PRR) that represents the number of successfully received packets by the reader compared to the total number of requested packets. Here, a packet contains sensor information from all transponders within the network during a single refresh (Fig. 71).

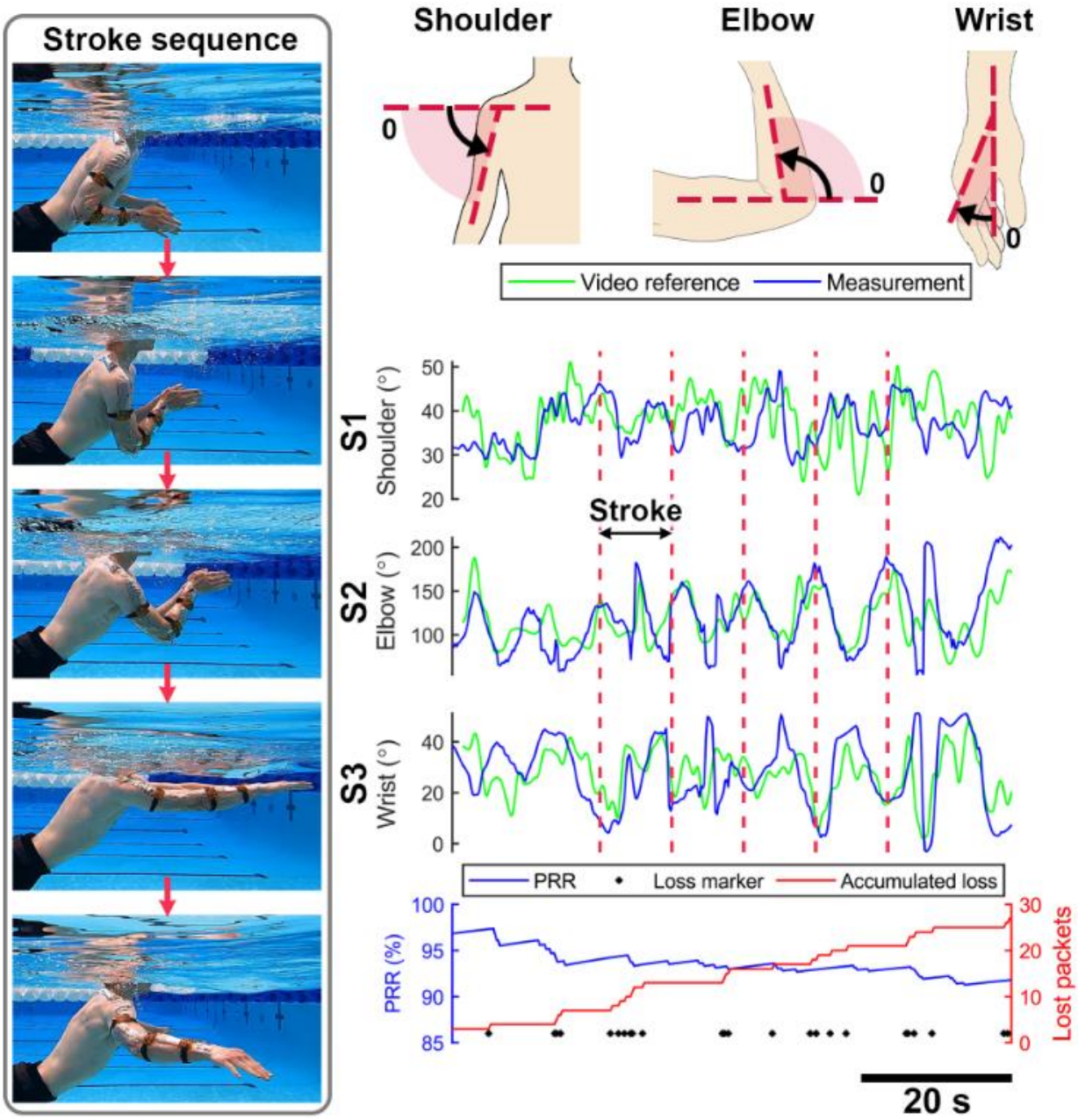

Fig. 71. Collected motion data from the strain gauges while swimming underwater.

Generally, conventional computer vision packages sporadically fail to extract the swimming posture angles particularly due to lack in mobility (causing misaligned camera position compared to the dynamically moving body), in addition to environmental artifacts such as underwater reflections that interfere with the camera sensor (Fig. 72).

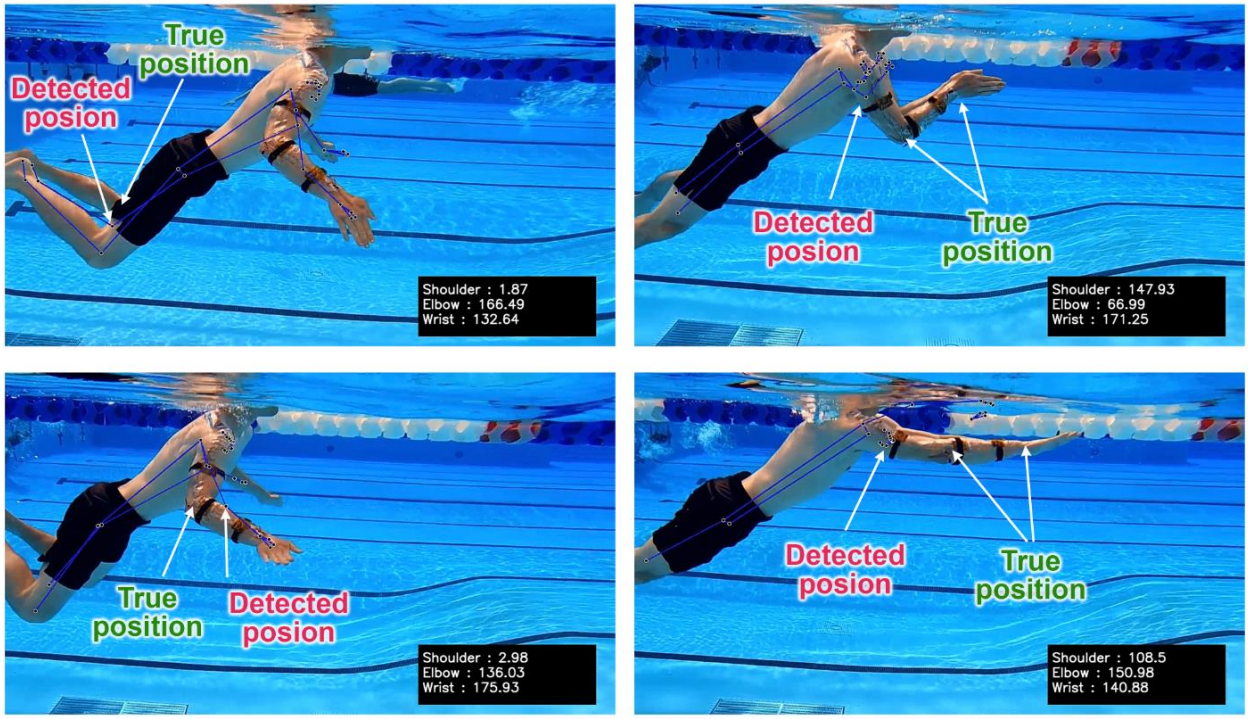

Fig. 72. Misaligned camera position (compared to the dynamically moving body), in addition to environmental artifacts such as underwater reflections that interfere with the camera sensor often result in incorrect body angle detection.

Furthermore, the smooth transition and reliable performance of this NFC-based BAN is compared with standard Bluetooth-based solution in underwater settings. While gradual wetting and full submersion of this epidermal BAN causes 3% packet loss (at 10 Hz of total refreshing rate), the received signal strength indicator (RSSI) of the Bluetooth-based communication fails instantaneously by submerging the Bluetooth beacon only. This highlights the network's robustness and adaptability to different environments with varying levels of humidity and background loss (Fig. 73).

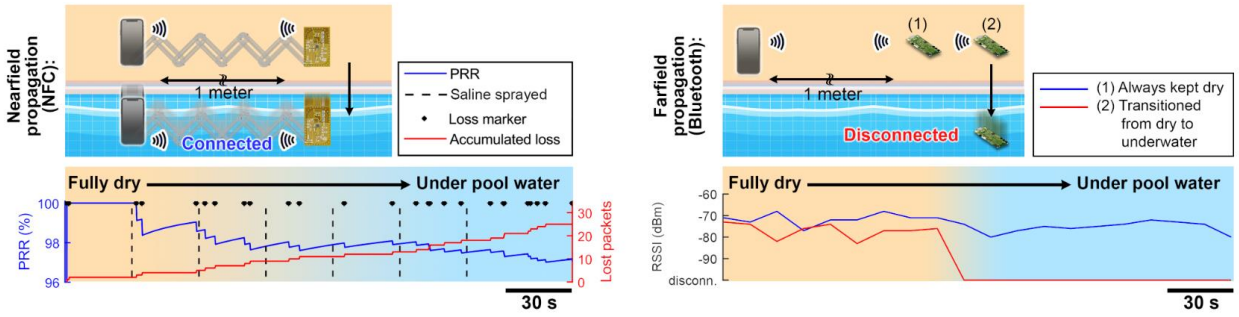

Fig. 73. The nearfield propagation of the NFC-based BAN continues to function reliably from dry to underwater environments. Bluetooth communication fails immediately after submerging any of the nodes underwater.

we utilized two identical custom beacons (based on Nordic nrf52840 Bluetooth 5.3 transceiver) with different advertising names whose RSSI was recorded regularly while connected to a hub (smartphone). The hub and one of the beacons (as a control experiment) were fixed and immobilized in dry condition, while the other beacon (as the test experiment) was submerged in water after 100 seconds. Unlike the NFC protocol, the Bluetooth RSSI is reported only when a beacon is in reach, therefore the RSSI is not collectable when communication fails underwater.

Long-term underwater network performance shows a stabilized 10.6% packet loss rate within 110 min of activity recording. For the long-time network characterization, we implemented a controlled continuous bending cycle on the strain gauge (connected to NFC sensor board) that is linked to the NFC reader through an underwater array of MI metamaterials. We stopped the bending after about an hour to ensure that the packet loss is caused by the network and not by the sensor board or strain gauge (Fig. 74).

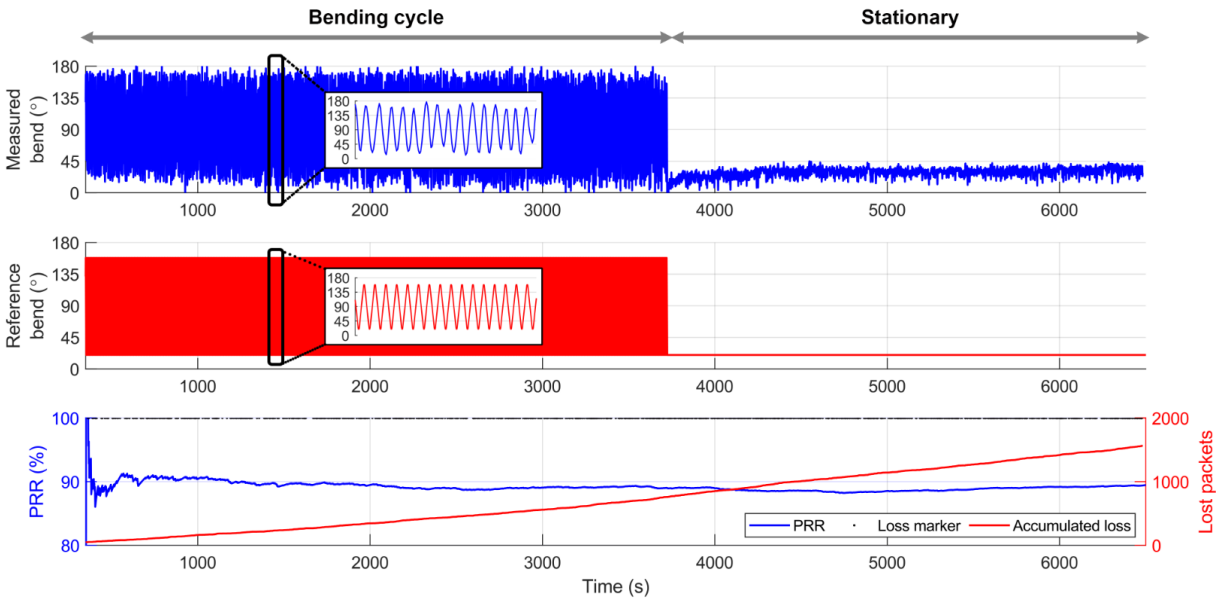

Fig. 74. Long-term reliability of encapsulated underwater link.

We induced sweating through 5 min of outdoor pushups under 86°F, which is shown to impact the packet loss. The PRR slightly drops from 97% to 93% (from start to end of intense activity) which is primarily due to sweat droplets accumulated under the coils. This is comparable to underwater setting in which the network is surrounded in lossy media. Either way, the impact is expected to last until the network is completely dried.

To study the impact of surrounding objects (such as conductive threads or metallic peripherals) on the network performance, we recorded the PRR over 4 minutes while placing a standard piece of aluminum sheet covering about 30 cm2 of the dry encapsulated skin patches (highlighted from 60 to 180 s) on dry skin patches. This suggests a loss rate of approximately 7 packets/min at a sampling rate of 2 Hz. Importantly, the sensor data demonstrates minor interferences, which may have been caused by the nature of amplitude shift key modulation employed in NFC protocol (Fig. 75).

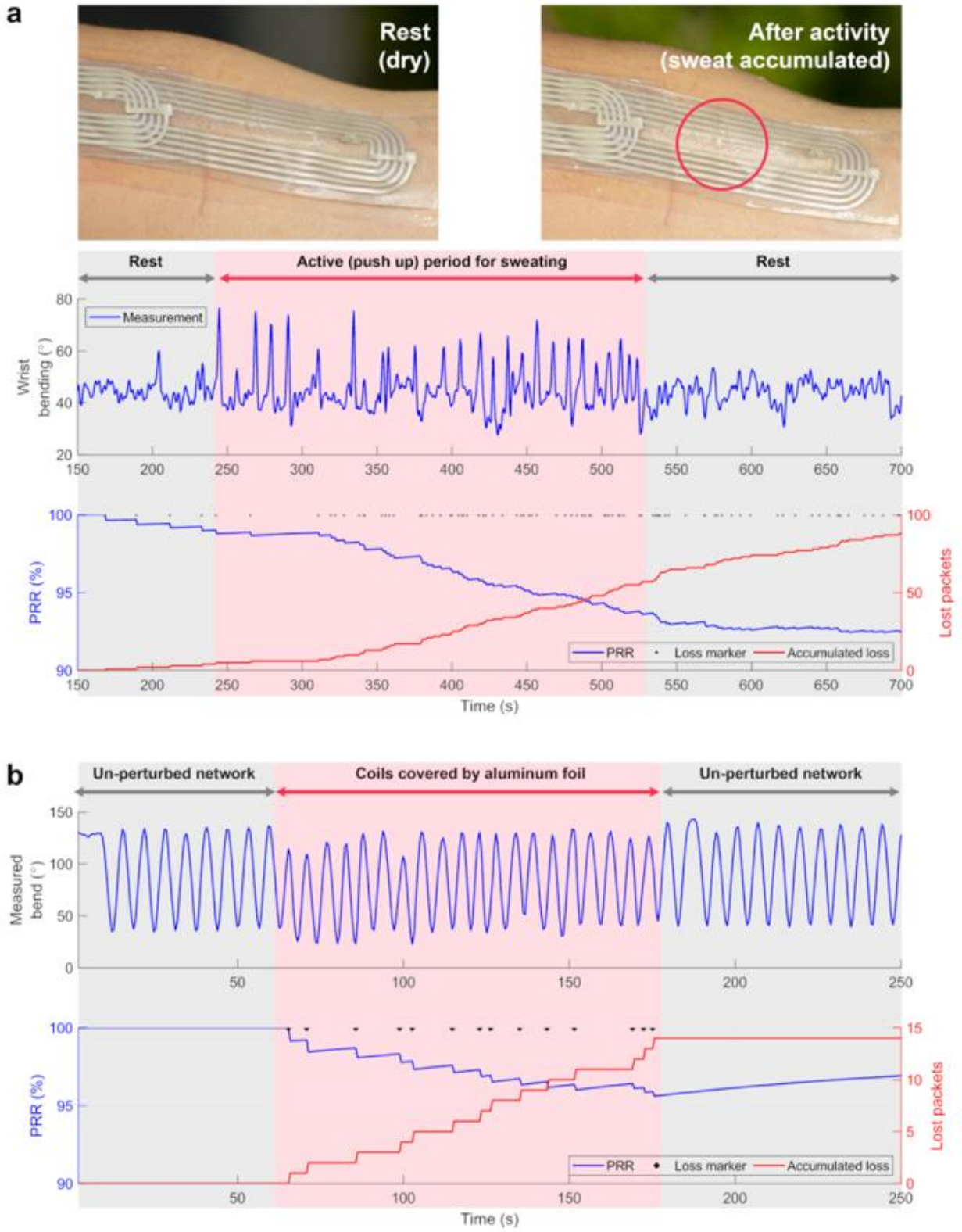

Fig. 75. Environmental impacts on PRR. (a) Network performance under sweating. (b) Effect of metallic objects in proximity of the network.

This approach enables encapsulated MI metamaterials to be utilized in a variety of hardware architectures, ultimately enabling wearable system designers to incorporate connector-free daughter boards (such as the wearable passive sensor boards in here) within a larger platform. The hardware architecture of the encapsulated MI channels is compared with common wired approaches in Fig. 76, showcasing the promising application of these units in multi-environment settings.

Method	Pro	Con	Architecture
Wired (parallel)	• Direct sensor integration	• Excessive connectors • Multiplexing required • Long wires • Sensor chaining not possible • Inadequate sensor sealing • Challenging network modification	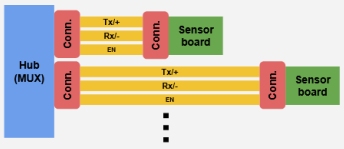
Wired (serial)	• Shorter/fewer wires • Direct sensor integration • Sensor chaining possible	• Excessive connectors • Different sensor addresses required • Inadequate sensor sealing • Challenging network modification	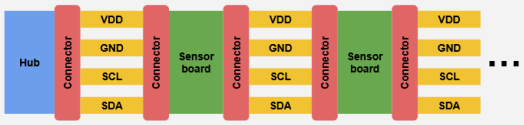
Proposed wireless (MI channel)	• No connectors • No wires • Fully encapsulated • Sensor chaining possible • Effortless network adjustment/extension	• NFC transponder required • MI channel required	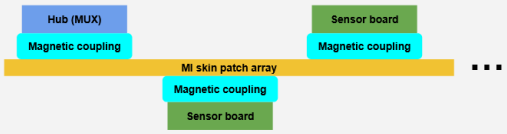

Fig. 76. Comparison of hardware system integration with traditional wired and proposed wireless mechanism based on MI metamaterials.

3.6.1. Other forms of skin integration

The versatility of magnetoinductive resonators extends to their facile integration across diverse form factors and substrates. To exemplify this adaptability, we showcased the integration of these resonators into distinct configurations. Notably, we successfully incorporated these resonators into a kinesiology tape, as well as a breathable medical grid wound patch, underscoring the broad spectrum of integration possibilities (Fig. 77).

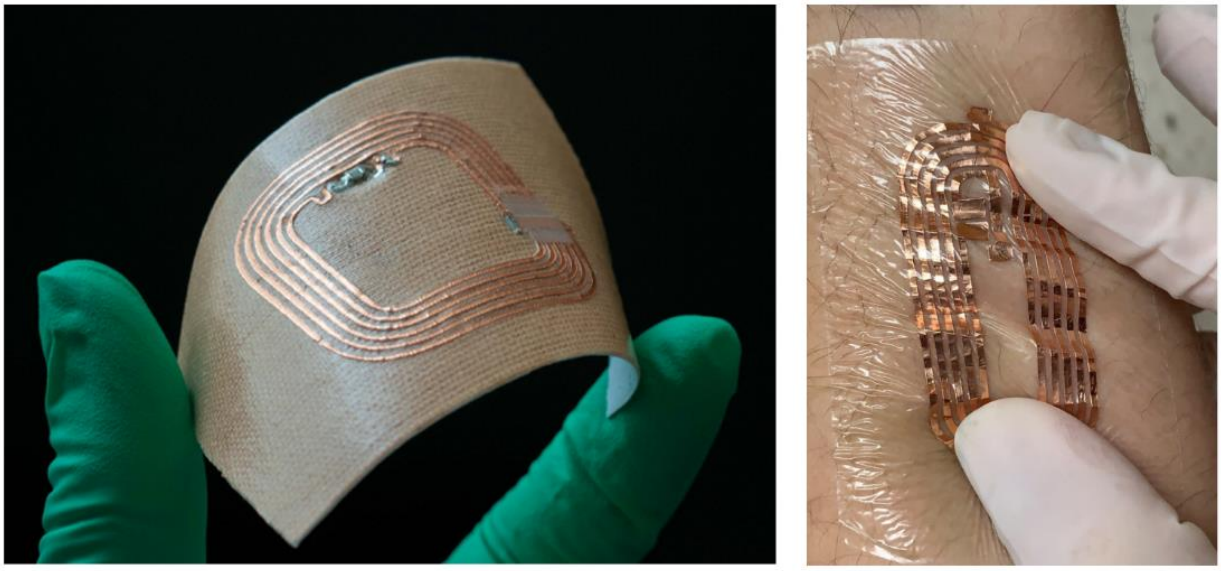

Fig. 77. Integration of MI resonators into kinesiology tape, as well as a breathable medical grid wound patch.

The proposed epidermal BAN is compared with state-of-art BAN technologies in **Table 3**.

Table 3. Landscape of available BANs.

Method	**Wired**[94]	**Body-coupled capacitive**[52], [95]	**Magnetically-dominant coupling**[96]	**Farfield radiation**[6], [97]	**Clothing-integrated nearfield propagation**[55]	**Skin-integrated Nearfield propagation (this work)**
Frequency range	100 kHz - 1 MHz	< 150 MHz	100 – 200 MHz	2.5 - 5 GHz	13.56 MHz	13.56 MHz
Pre-existing protocol compliance	Yes (various serial buses)	No	No	Yes (BLE, Wi-Fi, Cellular)	Yes (NFC)	Yes (NFC)
Power transfer capability	Yes (µW to W range)	Yes (µW range)	Yes (mW range)	No	Yes (mW range)	Yes (mW range)
On-demand network extension	Difficult	Easy	Easy	Easy	Easy	Easy
Path loss in proximity of body (dry setting)	Extremely small (< 0.3 dB/m at 10 MHz)	Large (> 60 dB/m at 10 MHz)	Small (< 30 dB/m at 100-200 MHz)	Small (about 15 dB/m at 10 MHz; about 50 dB/m at 2.4 GHz)	Very small (< 18 dB/m at 13.5 MHz)	Small (< 25 dB/m at 13.5 MHz)
Path loss in extreme (underwater) environments	Extremely small (< 0.3 dB/m at 10 MHz with sealed connectors)	Non-functional	Large (anticipated > 30 dB/m at 100-200 MHz)	Non-functional	Non-functional	Small (< 25 dB/m at 13.5 MHz)
Propagation security	Bound to wires	Bound to body surface	Prone to third party listening in proximity	Prone to third party listening in far	Bound to body surface	Bound to body surface
Versatility	Compatible with standard	Specialized reader/sensor communication	Specialized reader/sensor communication	Compatible with standard	Compatible with standard	Compatible with standard
Reader or sensor placement	Only at the hub/terminals due to connectors	Anywhere	Anywhere	Anywhere	Anywhere	Anywhere
Conformal to bodily stretches	No	Yes	Yes	Yes	No	Yes (up to 120% strain when fully sealed)

4. SPOOF MAGNETIC SKYRMIONS

4.1. Introduction

In recent years, magnetic skyrmions have emerged as intriguing topological spin textures within condensed matter physics, garnering significant attention due to their unique properties and potential applications. Skyrmions are nontrivial spin configurations characterized by localized swirling spin patterns that offer promising avenues for novel physical phenomena and technological advancements. These topological objects arise from the competition between exchange interactions, magnetic anisotropy, and the Dzyaloshinskii-Moriya interaction in chiral magnetic materials, leading to their stable formation at nanoscale dimensions [98].

The versatile properties of magnetic skyrmions have ignited considerable interest in harnessing their potential for innovative applications in various fields [99]–[105]. Of particular significance is their potential impact in the realm of optics and higher frequency regimes. The interaction between light and magnetic skyrmions has shown promise for optical manipulation and control of these nanoscale spin textures. The coupling of light with magnetic skyrmions enables the probing and modulation of their dynamic properties, offering opportunities for the development of all-optical switching devices, information storage, and signal processing [106]. Additionally, their unique excitation ability at specific frequencies renders them suitable candidates for spintronic oscillators and microwave signal generation.

The use of skyrmions has been traditionally limited to high frequencies (often above hundreds of GHz). High precision multiband performance of these physical structures, however, could significantly benefit applied physics, particularly for powering and communication purposes.

Here we demonstrate artificially induced chirality in subwavelength resonators to mimic the general behavior of a magnetic skyrmion, therefore introducing the spoof magnetic skyrmions (SMS) to realize multipurpose wireless power and data transfer channels for miniature electrical vehicles (mini EVs) for small scale robotic applications.

4.2. Spoof Magnetic Skyrmions

4.2.1. Higher Order Resonances

A multiturn loop inherently exhibits resonance at both fundamental and higher-order frequencies. In the case of fundamental resonance, the surface current's magnitude demonstrates a spatial pattern characterized by a single peak positioned at the center of the loop's electrical length, flanked by nulls at the ends. This spatial configuration corresponds to half the wavelength of the fundamental frequency. As we progress to the second order of resonance, the surface current exhibits dual peaks, and this pattern continues for subsequent orders (Fig. 78). By establishing the equivalent circuit for this multiturn loop, we can vary its complexity to effectively encompass higher-order resonances and achieve a wider bandwidth, providing a comprehensive framework to describe the behavior of these resonances.

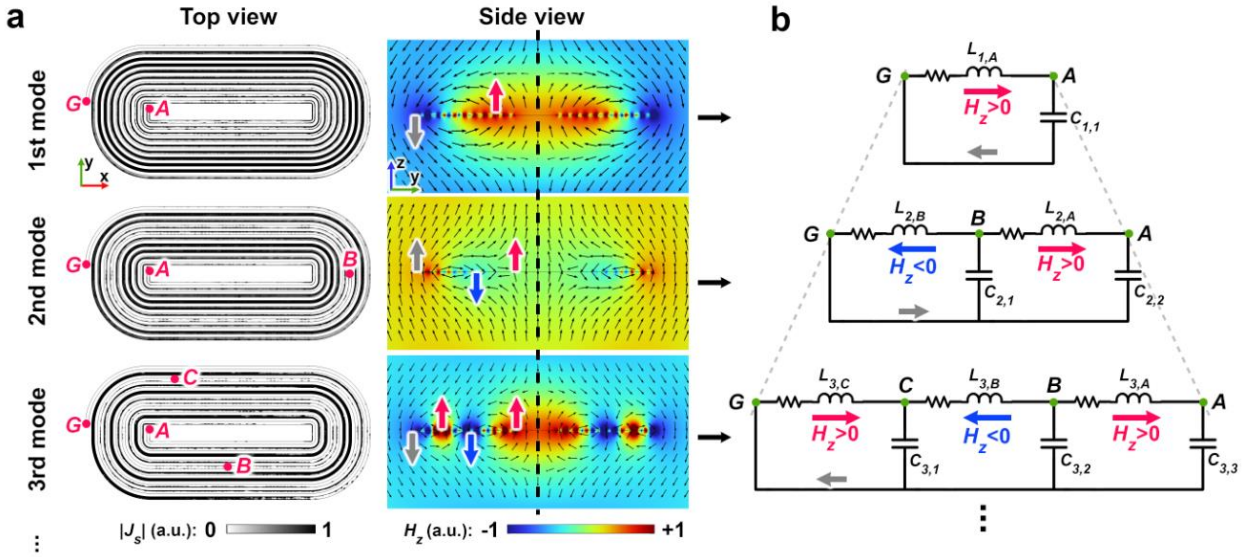

Fig. 78. Fundamental and higher order resoancens in multi-turn loops. (a) The surface current as well as the magnetic field profiles facilitate extraction of equivalent circuits at the desired bandwidth.

4.2.2. Artificial Manipulation of Resonances

Magnetic skyrmions inherently exhibit extensive higher-order resonances across a wide bandwidth. In this context, our objective is to enlarge these structures significantly while intentionally inducing resonances at specific frequencies of importance. This endeavor leads to the creation of a "spoof magnetic skyrmion", allowing us to utilize these resonances for signaling and communication purposes.

In the general equivalent circuit of a multiturn loop, the presence of stray capacitances primarily arises from lumped capacitors (Fig. 79).

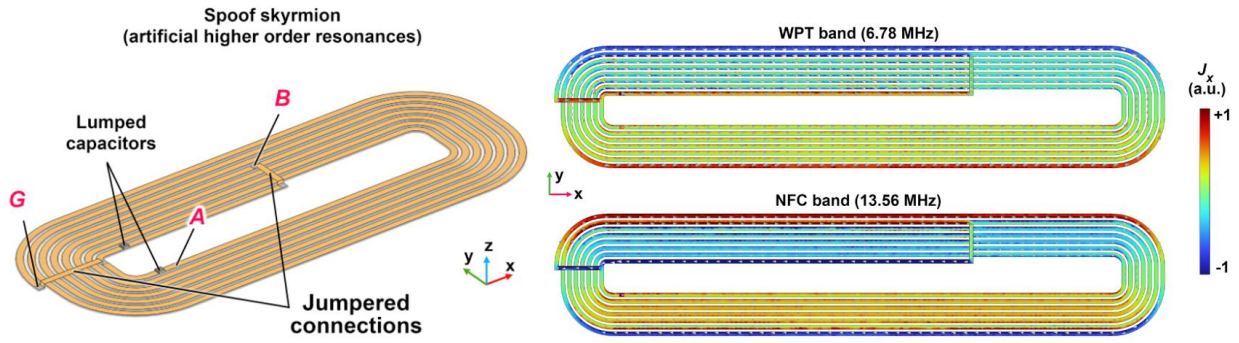

Fig. 79. Geometry and surface currents of the artificially manipulated spoof magnetic skyrmions.

This strategy allows for inducing resonances at desired frequencies that are naturally unreachable by stray capacitances; hence we name the structure spoof magnetic skyrmion (SMS).

4.2.3. Spoof Magnetic Skyrmion Array Analysis

The equivalent circuit to the array of spoof magnetic skyrmions is similar to that of the MI metamaterials. We assume that the current flowing in the n^{th} resonator has a sinusoidal time-dependency with an angular frequency of ω (shown in Fig. 80)

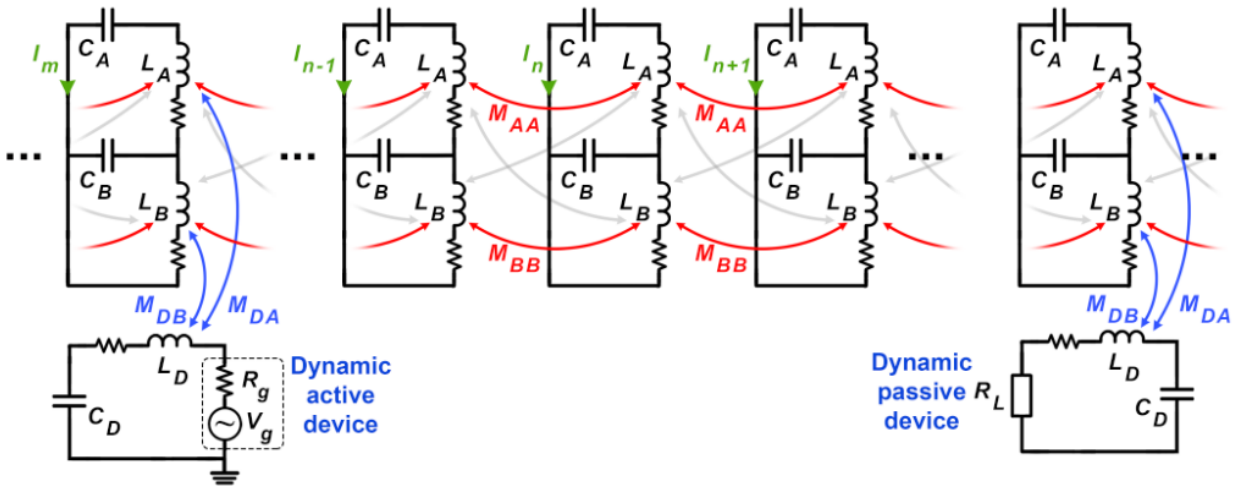

Fig. 80. General equivalent circuit of an array of spoof magnetic skyrmions is inherently similar to that of MI metamaterials.

4.2.4. Deriving the Dispersion Diagrams

First, we define the sub-loop impedances:

$$\begin{cases} Z_A = R_A + j\omega L_A + \frac{1}{j\omega C_A} \\ Z_B = R_B + j\omega L_B \end{cases} \quad (14)$$

The current running on the n^{th} resonator (flowing through the sub-loop B, with n ranging from 1 to N) in a linear array (distanced by d_c) can be represented by:

$$I_n = I_1 e^{j\phi_1}\, e^{-j\gamma(n-1)d_c} \quad (15)$$

where γ is the travelling wave's propagation constant, I_1 and ϕ_1 are the first loop's current magnitude and phase depending on the excitation (boundary conditions imposed by reader's V_g). For ease in mathematical analysis, we define F as the ratio between the currents ran on L_A to L_B:

$$F = \frac{\frac{1}{j\omega C_B}}{\frac{1}{j\omega C_B} + Z_B} \quad (16)$$

Note that each inductor is coupled to four other inductors, including the corresponding (M_{AA} and M_{BB}) and adjacent loops (M_{AB}) of two neighbor resonators, however, magnetic coupling to the adjacent loop is significantly weaker than that of the corresponding loop due to the overlapping geometry of resonators. The Kirchhoff's voltage law for the n^{th} coil follows:

$$Z_A I_n + j\omega M_{AB} F I_{n+1} + j\omega M_{AA} I_{n+1} + j\omega M_{AB} F I_{n-1} + j\omega M_{AA} I_{n-1} +$$

$$+ Z_B F I_n + j\omega M_{AB} I_{n+1} + j\omega M_{BB} F I_{n+1} + j\omega M_{AB} I_{n-1} + j\omega M_{BB} F I_{n-1} = 0 \quad (17)$$

Which can be simply rewritten as:

$$Z_A I_n + j\omega M_{AB} F(I_{n-1} + I_{n+1}) + j\omega M_{AA}(I_{n-1} + I_{n+1}) +$$

$$+ Z_B F I_n + j\omega M_{AB} F(I_{n-1} + I_{n+1}) + j\omega M_{BB} F(I_{n-1} + I_{n+1}) = 0 \quad (18)$$

Given the sinusoidal current waveform represented above, we may conclude:

$$I_{n-1} + I_{n+1} = 2I_n cos\,(\gamma d) \tag{19}$$

Applying (19) into (18) will result in the dispersion equation for the array of SMS:

$$\gamma = \frac{1}{d_c} cos^{-1}\left(-\frac{Z_A + Z_B F}{2j\omega M_{AB} F + 2j\omega M_{AA} + 2j\omega M_{BB} F + 2j\omega M_{BB}}\right) \tag{20}$$

A mathematical analysis with appropriate equivalent circuit component values results in a dispersion diagram with two passbands engineered at desired frequencies (Fig. 81)

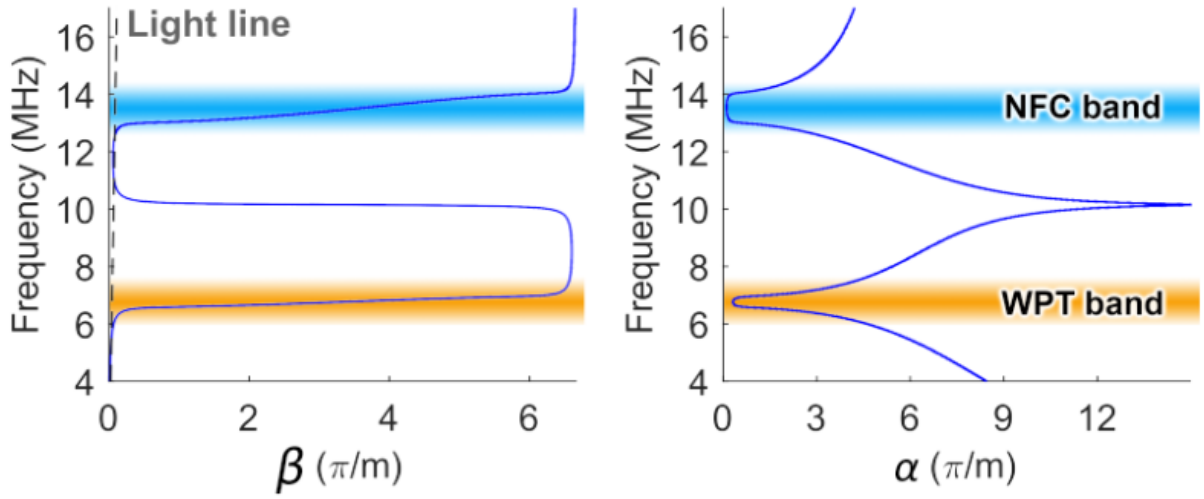

Fig. 81. Dispersion diagram of SMS arrays with two passbands engineered at desired frequencies.

Here, $u = L_A/L_B$ specifies the artificial unbalancing factor between the partial inductances and can be utilized to engineer the gap between the passbands, also known as bandgap (Fig. 82).

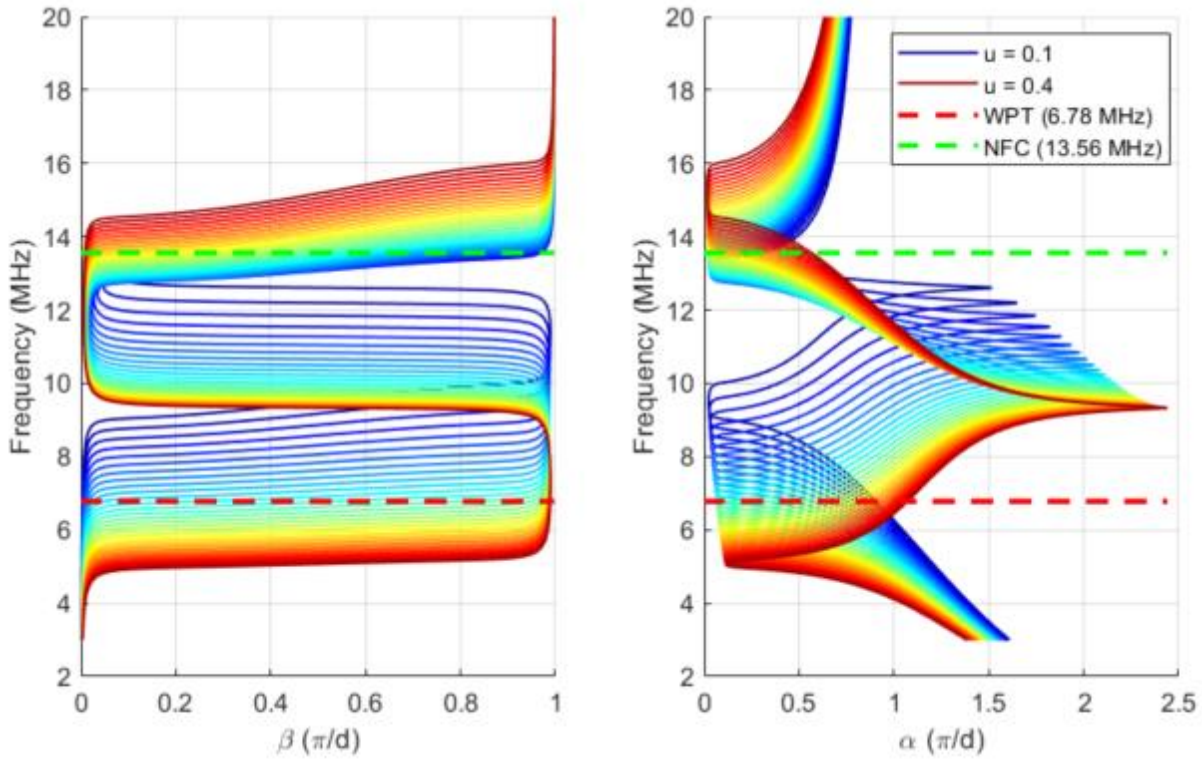

Fig. 82. Engineerign the bandgap characteristics of SMS arrays.

4.2.5. Spoof Magnetic Skyrmion Fabrication

We fabricated the SMS structure using the same method developed to produce MI resonators through programmed cut of copper sheet on a flexible vinyl adhesive substrate (Fig. 83).

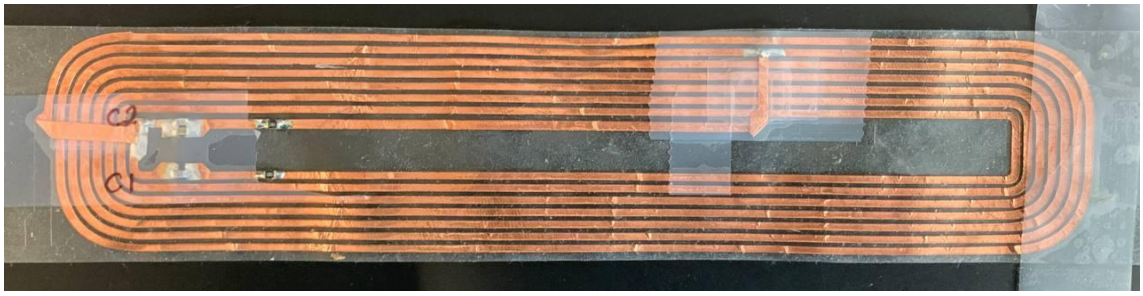

Fig. 83. Fabricated spoof magnetic skyrmions with engineered resonances at 6.78 and 13.56 MHz.

We fabricated an array of SMS resonators and evaluated their insertion loss, compared with that of a MI resonator array for various Tx and Rx distances across the array (Fig. 84).

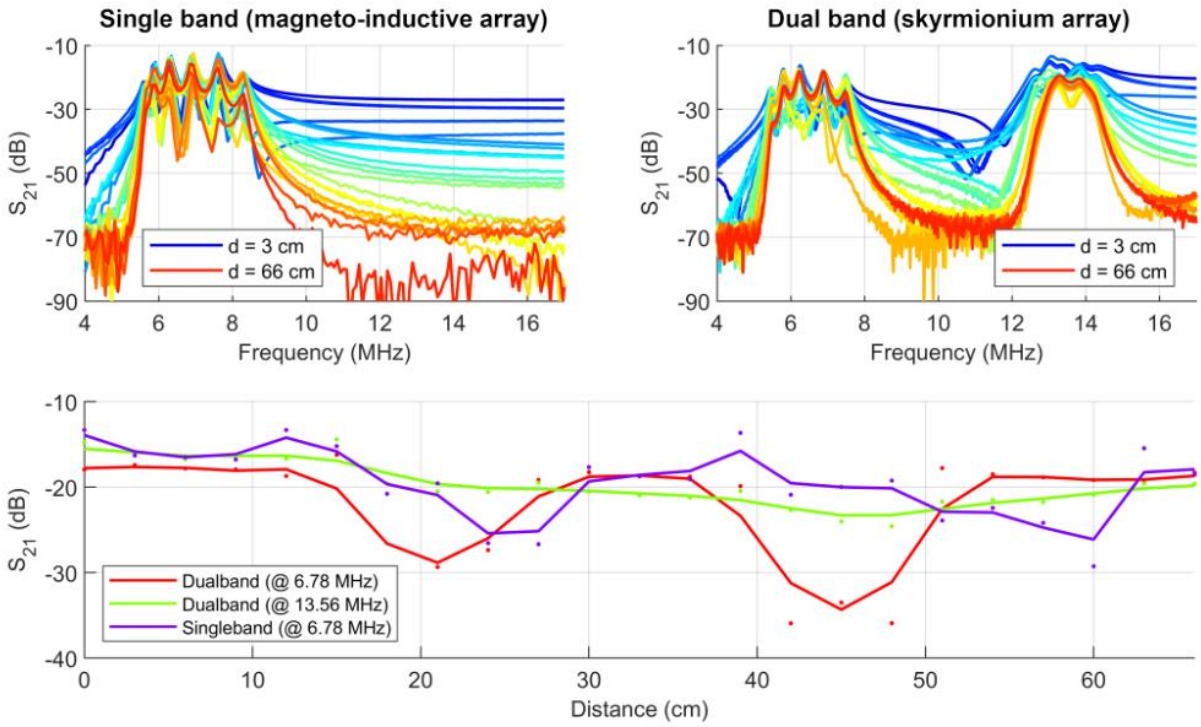

Fig. 84. Transmission profile of the introdced SMS array compared with that of the MI array tuned at 6.78 MHz (for WPT purposes).

4.3. Application in Multipurpose Local Area Networks

4.3.1. High Level Implementation

This study is centered on the investigation of dynamic wireless power and data transfer capabilities through a local array of SMS structures. To this end, our primary objective involves the engineering of second-order SMS passbands at frequencies of 6.78 and 13.56 MHz. These specific frequencies are strategically chosen to align with the AirFuel and NFC protocols, catering to wireless power and data transfer respectively. By achieving this frequency alignment, we effectively showcase the adaptability of our passband engineering approach to comply with both protocols. Additionally, we explore the advancement of WPT through the implementation of on-demand and localized power flow control. This aspect holds significant promise within the realm of WPT schemes, contributing to the progression of this field (Fig. 85).

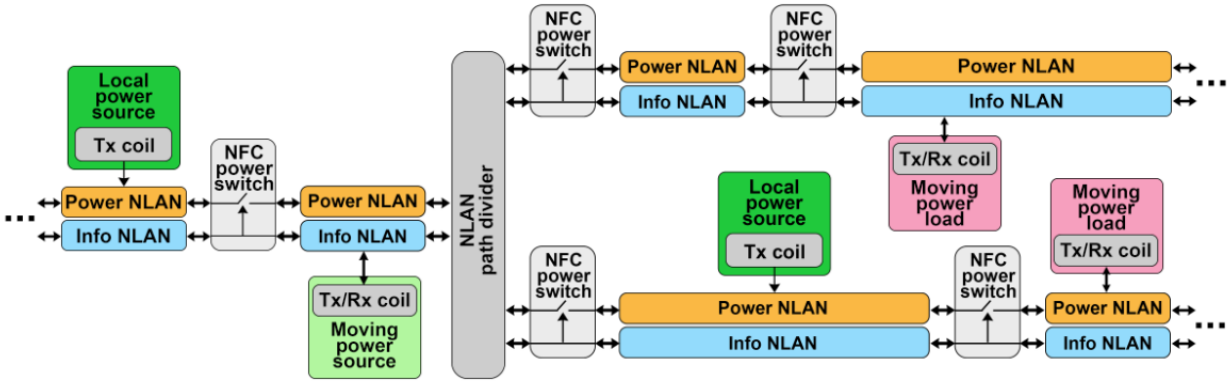

Fig. 85. High-level block diagram of the proposed controlled dynamic WPT mechanism.

4.3.2. Unique Capabilities

Due to the real-time interaction established with moving objects within proximity of the SMS array, this approach facilitates the strategic deployment of both dynamic and static power sources. These sources inject energy utilizing AirFuel-compatible inverters operating at a frequency of 6.78 MHz. Consequently, direct accessibility to dynamic power receivers, authorized for power reception, is established. The authorization process for power reception is effectuated through a handshake protocol implemented on the NFC-compatible channel, which coexists within the same SMS array.

Significantly, the inherent passive nature of the SMS array distinguishes it from conventional WPT methodologies, which typically involve the incorporation of active coils beneath the power charging infrastructure. This inherent passivity makes the SMS array highly suitable for localized power transfer scenarios, characterized by a minimal to negligible infrastructural expenditure. Furthermore, its inherent adaptability for on-demand expansion aligns harmoniously with the principles of scalability and flexibility (Fig. 86).

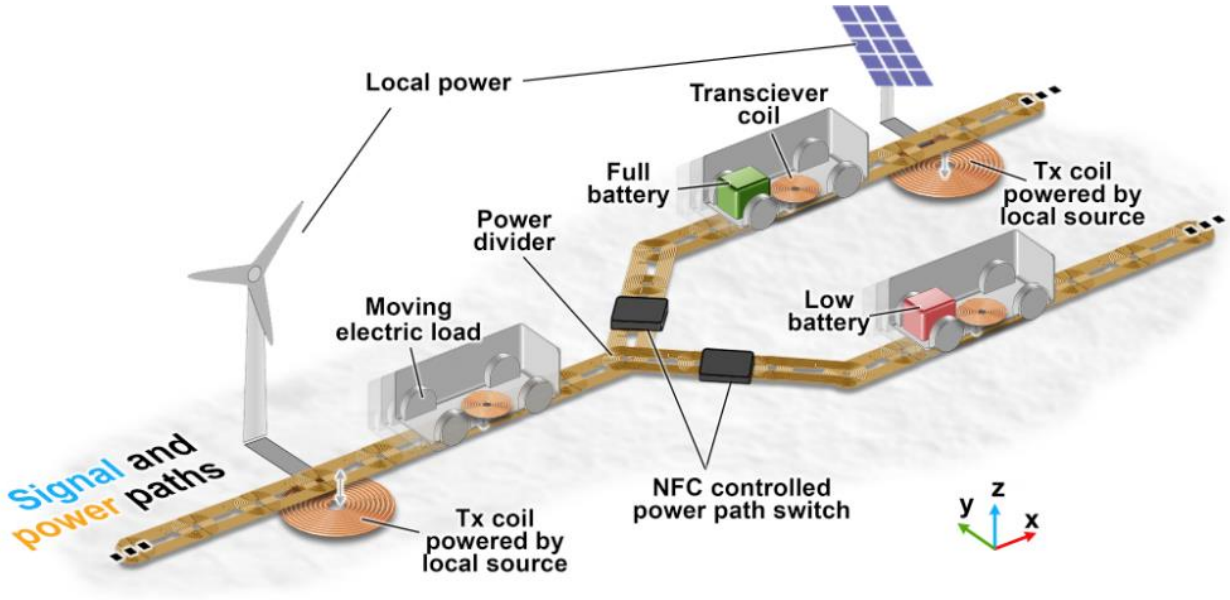

Fig. 86. Example implementation and application of the proposed SMS array in dynamic WPT.

4.3.3. Significance of Bandwidth in WPT

Traditionally, the mechanism employed for WPT entails magnetic coupling between two coils, either resonant or non-resonant in nature. As a result, frequency perturbations naturally arise due to impedance variations within the transmitter and receiver coils. This phenomenon similarly manifests within our SMS structure. Although adherence to the air-fuel WPT protocol mandates that the transmitter channel delivers power through a precisely tuned inverter calibrated at 6.78 MHz, inherent variations in the channel can induce subtle frequency deviations. To effectively counteract this potential discrepancy, a viable approach involves the broadening of the passband bandwidth specific to the WPT frequency. By implementing this strategy, the transmission of power can be maximized, leveraging the complete available power capacity. Consequently, maintaining a defined minimum bandwidth assumes pivotal importance in the context of WPT objectives. It's noteworthy that the WPT operation does not encompass intentional frequency modulation components.

To achieve this objective, we illustrate the transmission profile of the SMS array using both transmitter (Tx) and receiver (Rx) elements positioned at different locations. This demonstration serves to showcase the establishment of the WPT link in scenarios involving dynamically moving objects (Fig. 87).

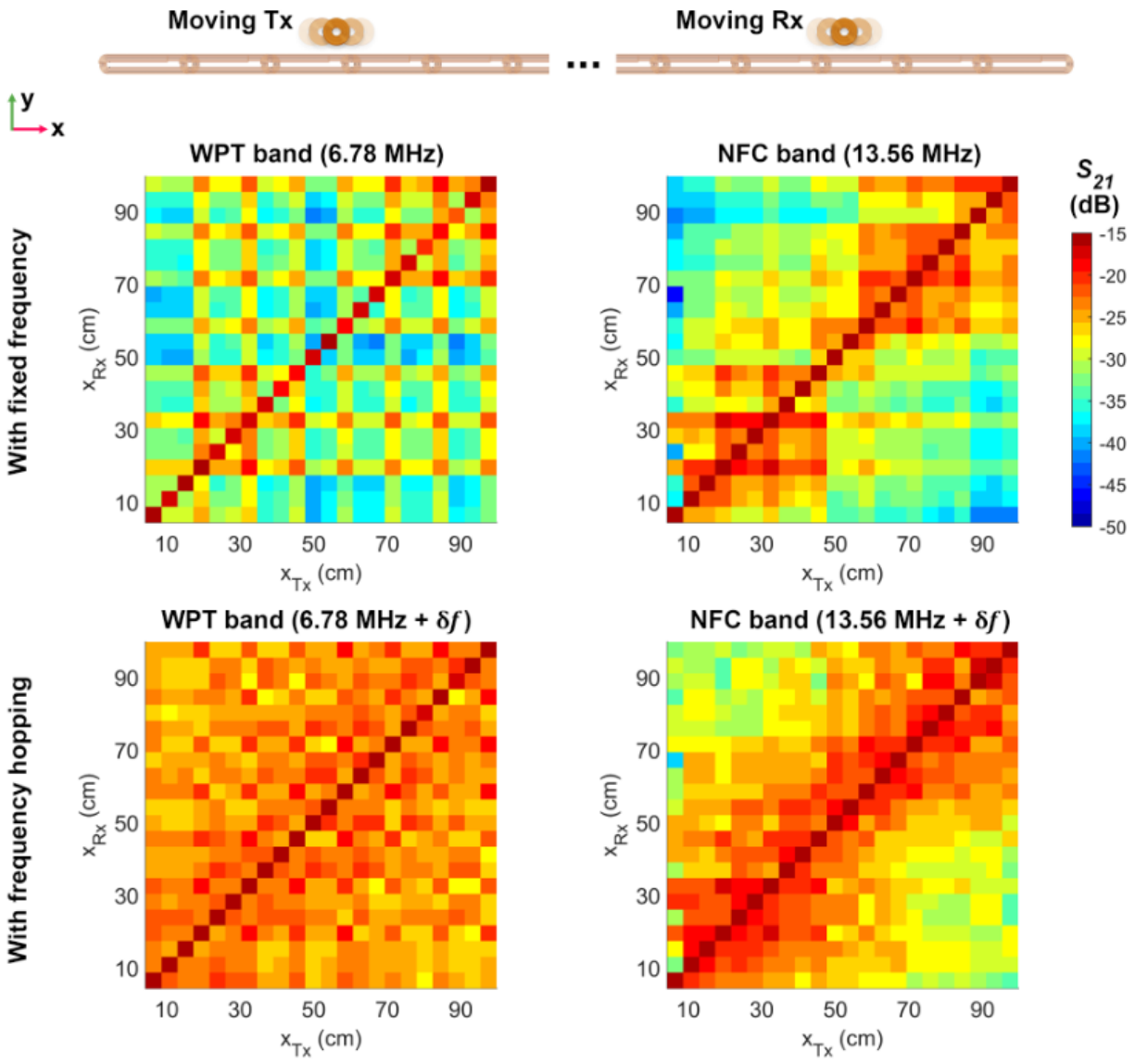

Fig. 87. Comparison of the SMS tranmission profiles with disabled (fixed) and enabled frequency hopping.

4.3.4. Implementation of Quiet Zones

In the context of dynamic WPT applications, where the power receiver undergoes dynamic movement in the vicinity of a road housing transmitter coils beneath its surface, there is often a necessity to strategically design the road trajectory. This design is contingent upon landmarks and the intricate topographical features of the terrain. This entails the possibility of routing the road even through moving structures. Furthermore, the need may arise to delineate specific zones along this power-transmitting road that operate as what can be termed as "blind spots." These zones are characterized by the absence of emitted magnetic fields. This configuration is motivated by considerations such as safety requirements (for instance, in underwater settings) or the imperative to mitigate electromagnetic interference within specific sections of the road. This concept, known as a "quiet zone," is an essential aspect of our investigation. Our efforts are focused on implementing such blind spots and seamlessly integrating them within the proposed SMS structure, thereby augmenting the versatility and adaptability of the system (Fig. 88 and Fig. 89).

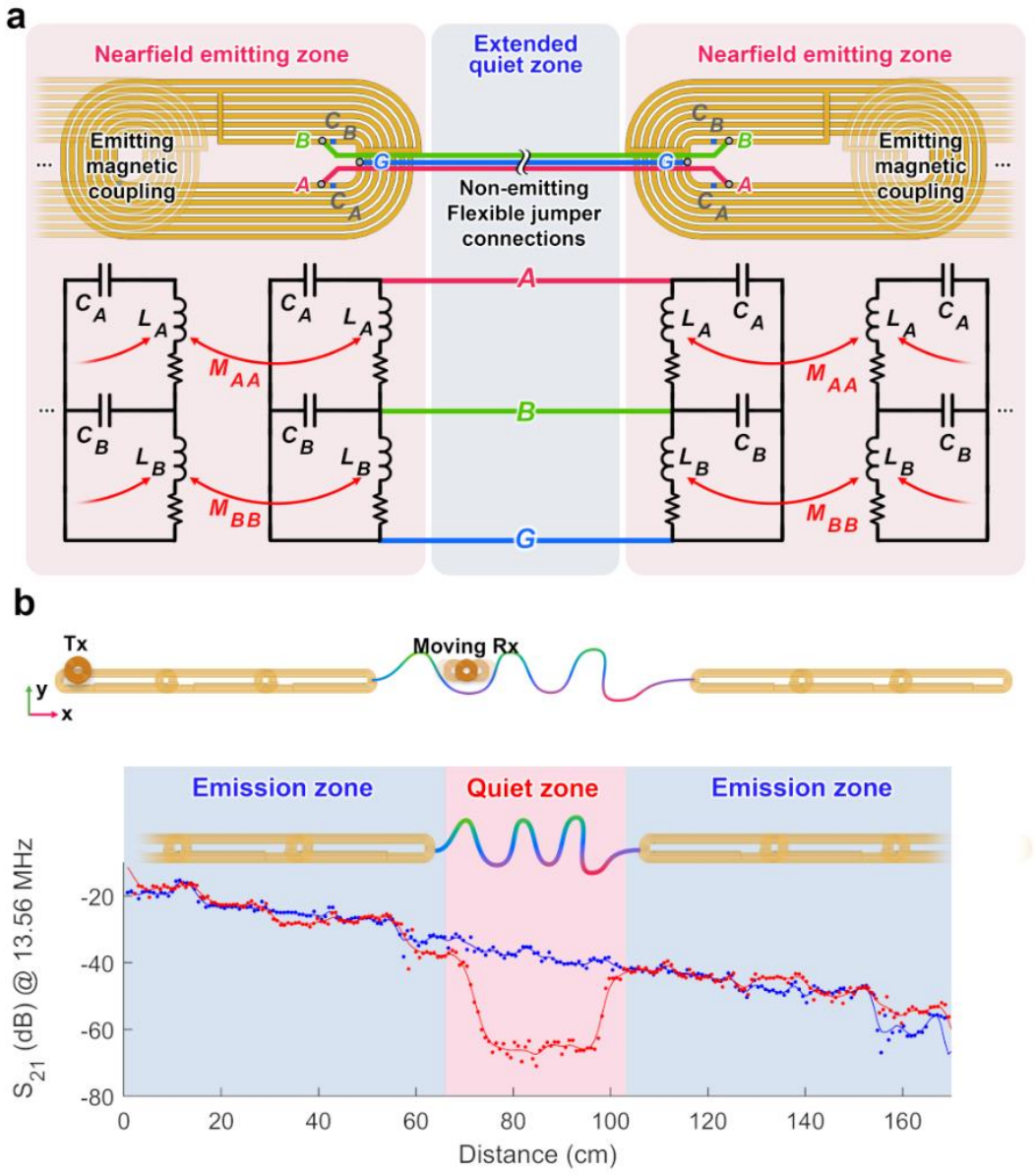

Fig. 88. Inducing quiet zones for maximal mechanical flexibility and improved electromagnetic interference performance.

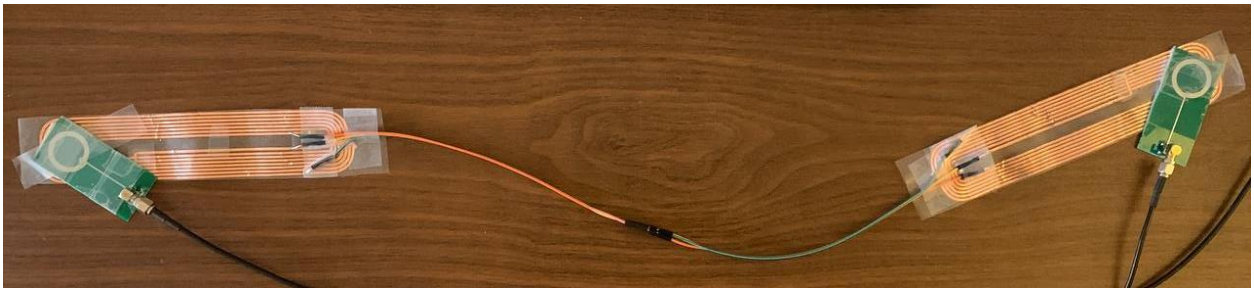

Fig. 89. Linked SMS resonators for quiet zone realization.

4.3.5. Power Flow Control

Our objective within this study is to showcase the effective power flow control achievable through the utilization of the SMS structure. We intend to fully capitalize on the concurrent power and data transmission capabilities inherent to the proposed structure. To this end, we leverage the NFC band, optimizing it as a conduit for the transfer of vital state-of-charge information between a power transmitter and its corresponding receiver. This strategic employment of the NFC band serves as a cornerstone for achieving precise power flow control.

Furthermore, our study encompasses the practical implementation of an NFC-compatible passive board. This board assumes the pivotal function of modulating the frequency characteristics inherent to the SMS structure. Through this modulation process, the ability to activate or deactivate the WPT band is conferred. This dynamic modulation is accomplished via the information exchanged through the NFC channel embedded within the same SMS link. This intricate integration stands as a testament to our endeavor to manipulate the frequency domain for effective power control, harnessing the interconnected potential of the NFC and WPT functionalities (Fig. 90, Fig. 91, and Fig. 92).

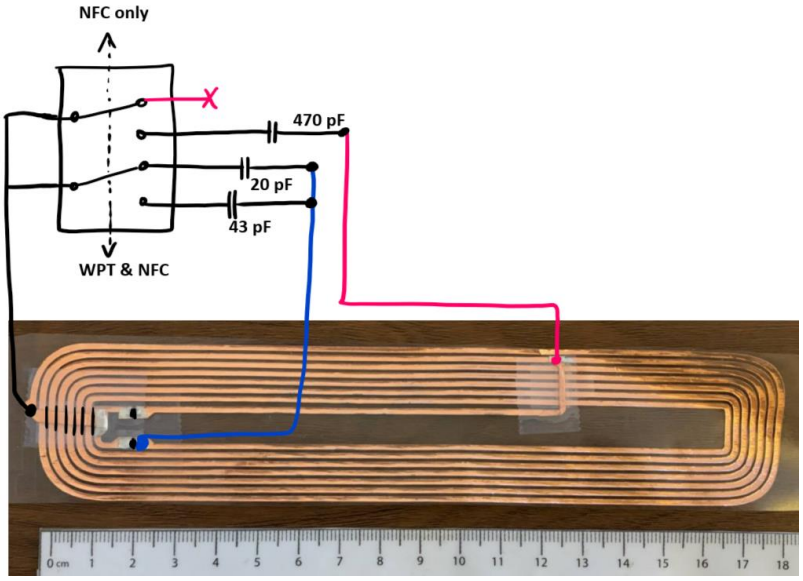

Fig. 90. Utilization of a relay for switching the resoance characteristics of an SMS.

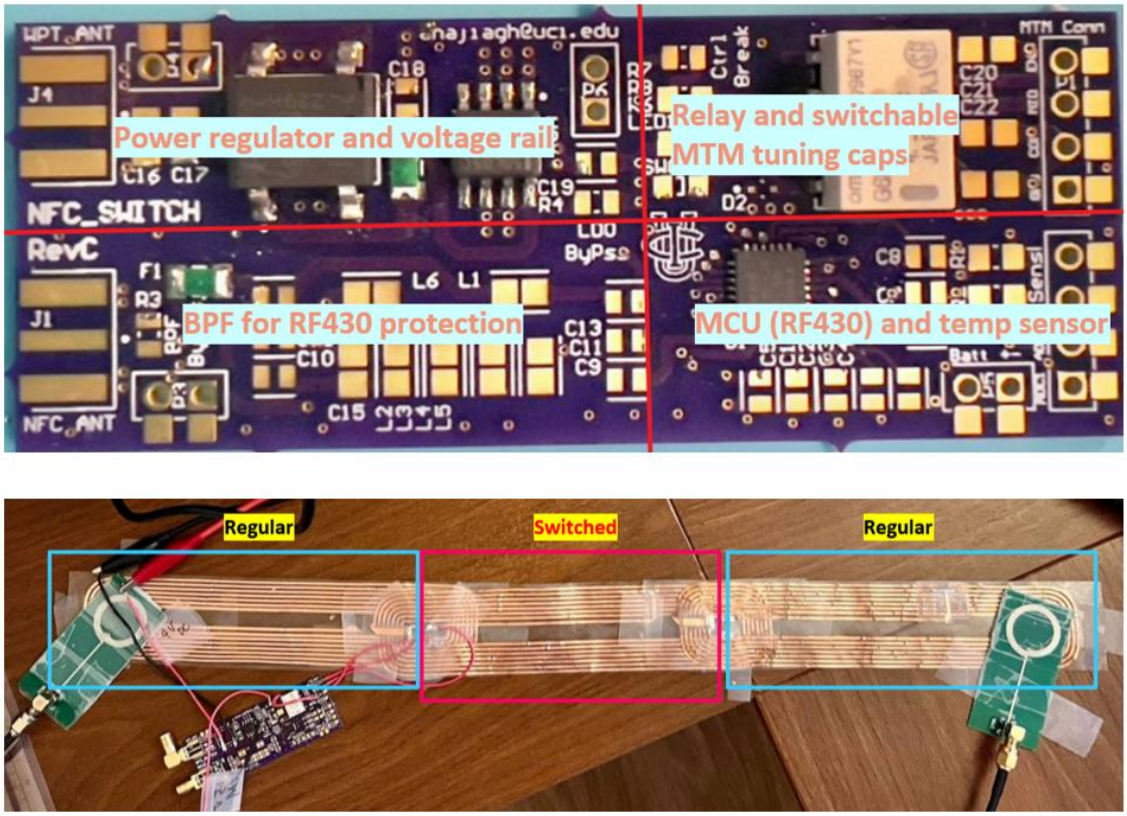

Fig. 91. NFC-controlled passive switch to enable/disable the WPT passband based on the received NFC message from the power source.

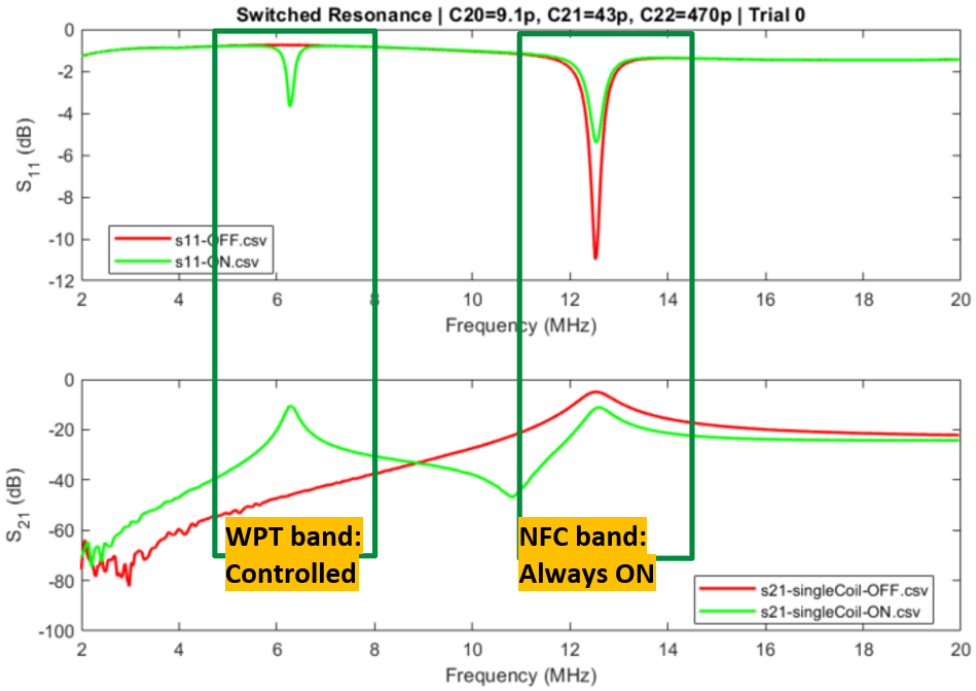

Fig. 92. Resultant passband characteristics of the switched SMS structure.

4.4. Hardware System Design

4.4.1. Active NFC Circuitry Protection

Within the framework of the active NFC readers, a meticulously designed architecture is realized. This includes the integration of a matching network, alongside an Electromagnetic Interference (EMI) filter, the latter functioning as a low-pass filter. This configuration is interposed between the loop antenna and the chip. Notably, in our implementation, a bandpass filter is introduced to mitigate the potential for power signals induced within the shared NFC and power receiver coil to adversely affect the integrity of the NFC signal.

To accommodate the specificities of the chip employed, an imperative voltage threshold is established. For the chip under consideration, the antenna pins have been configured with a maximum voltage rating of 10 volts peak-to-peak. Addressing this concern, a comprehensive solution is devised through the incorporation of a bandpass filter. This filter is realized using a third-order Legendre filter topology, seamlessly integrated onto our custom NFC reader board. This strategic implementation further ensures that the NFC and power signals coexist harmoniously, safeguarding the fidelity of the NFC communication while upholding the specified voltage constraints (Fig. 93).

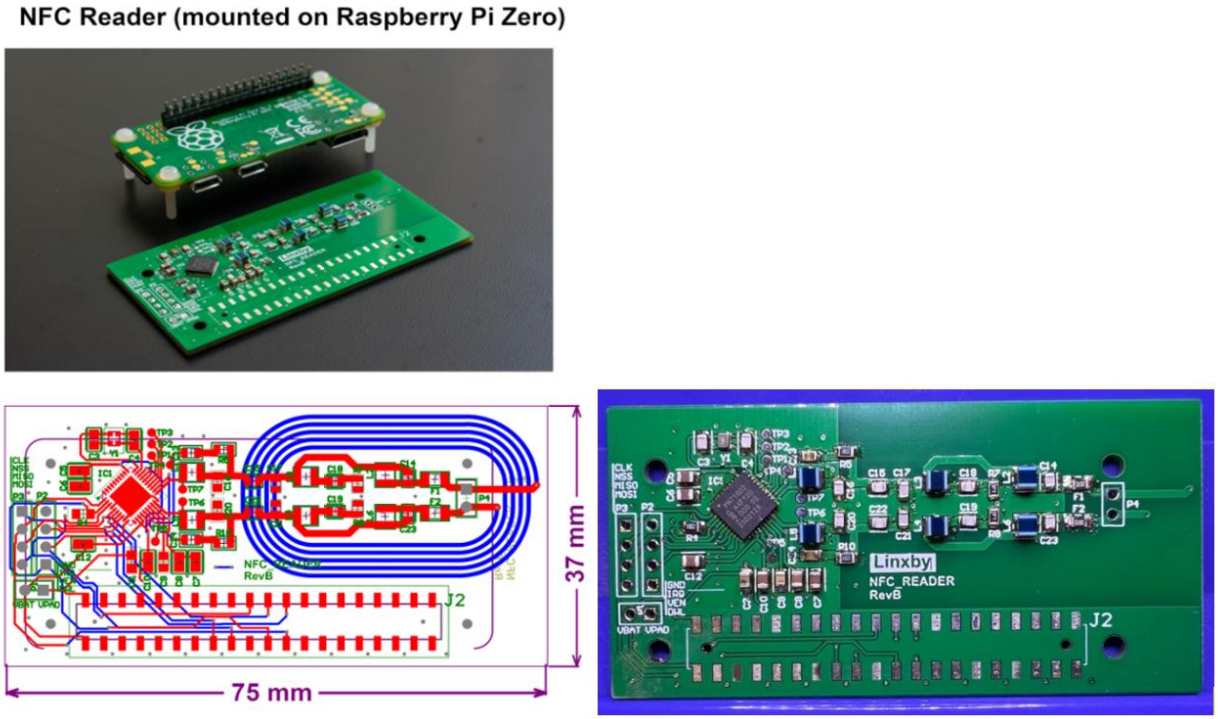

Fig. 93. Custom harsware for NFC reader incorporating the onboard matched coil and bandpass filter.

The custom bandstop (notch) filter design of this board is shown in Fig. 94.

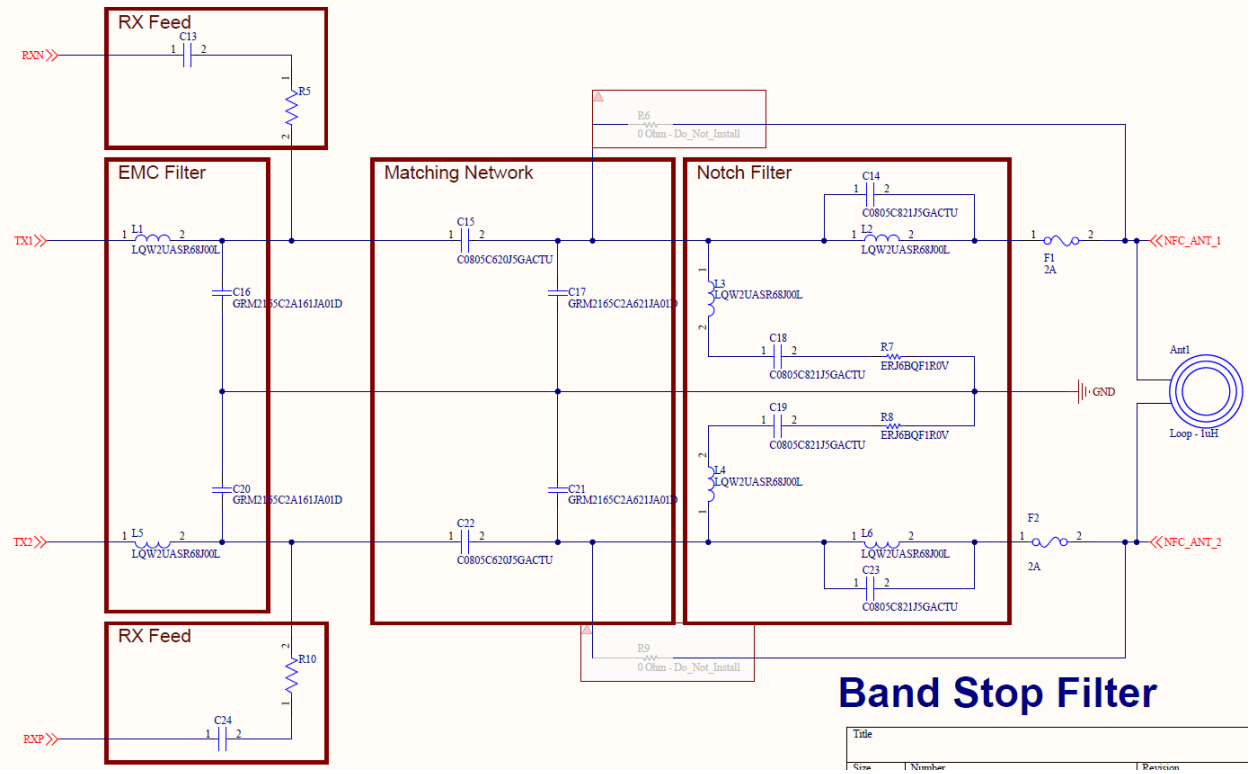

Fig. 94. RF front end design of the NFC reader board.

4.4.2. Passive NFC Reader Protection

The NFC circuitry is protected from the high power signal through a 3rd order external Legendre filter with on-board Rx coils (Fig. 95). This board utilizes a bandstop filter similar to the notch filter of the custom NFC reader board.

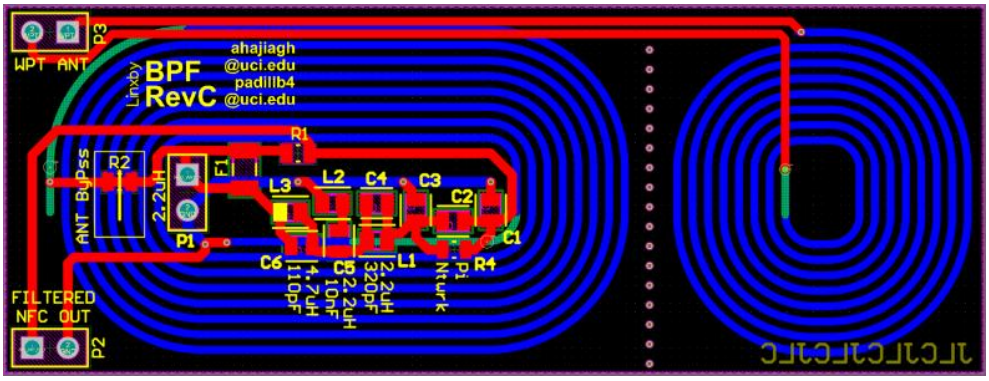

Fig. 95. Passive NFC circuitry protection using a coil-embedded band pass filter

4.4.3. Power Delivery Network

The power delivery Network (PDN), operates in this mechanism through the conversion of DC power using an inverter into an AC signal centered at 6.78 MHz. The inverter, sourced off-the-shelf for this project, holds the capacity to inject up to 300 watts of power. Alternatively, a custom-designed Class-E amplifier, implemented by high-switching frequency capabilities, can be employed to align with the air-fuel protocol. Following this conversion, the AC power signal is subsequently conveyed to a loop antenna, establishing magnetic coupling with the SMS array.

The propagated power signal traverses the length of the path within the SMS array, thus becoming accessible through power receiver coils integrated onto a mini-EV for the purpose of demonstration. The power receiver coil captures the AC power signal at 6.78 MHz, followed by its rectification via a Schottky diode. This diode effectively filters the AC power to minimize repels. Subsequently, the signal is channeled into a buck converter. The utilization of the buck converter is necessitated by the broad spectrum of input voltages received by the power receiver coil. The SMS array's insertion loss characteristic, contingent upon the relative distance between the power transmitter and receiver, contributes to this diverse input voltage range.

Buck converters, renowned for their efficiency as DC-DC converters, are adopted due to their capacity to accommodate a broad array of input voltages through an internal feedback loop (see Fig. 96). The buck converter is calibrated to yield a 6 V voltage output, further regulated to 5.5 V via a low dropout regulator (LDO). The incorporation of the LDO, despite its comparatively modest efficiency, serves to guarantee a repel-free power rail. This consideration arises due to potential limitations in the ability of buck converter inductors to entirely suppress repels, owing to form factor constraints. The LDO rectifies this by ensuring a repel-free power rail, albeit at the expense of minimal losses.

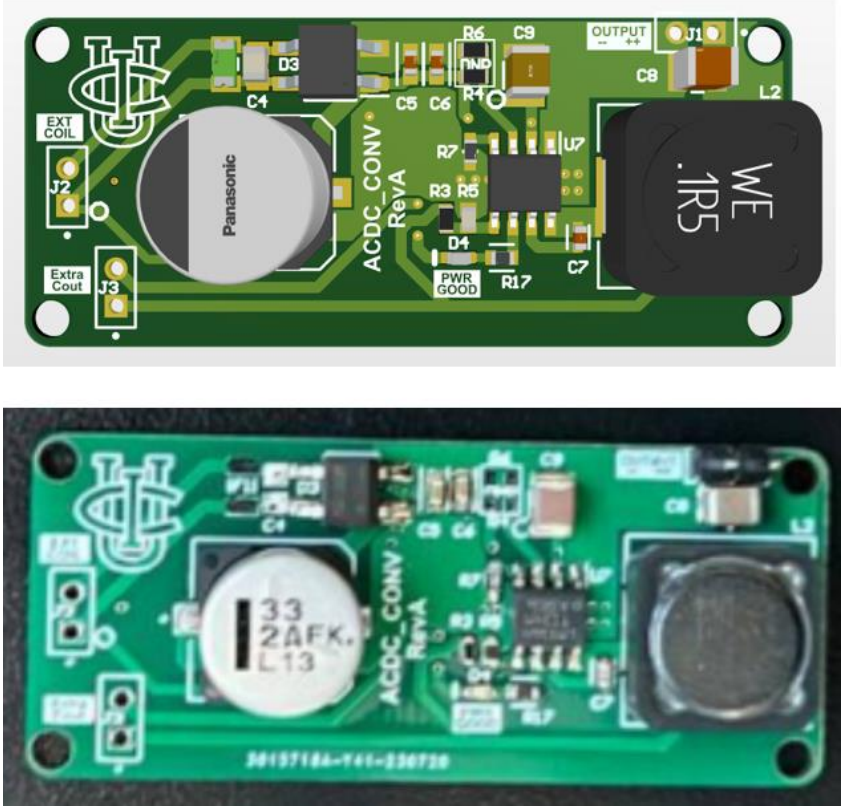

Fig. 96. Designed Buck converter with onboard power receiver coil and wide input voltage (7-100 V) and fixed output voltage (6 V).

The resultant 5.5 V output is directed to a battery charger governed by a microcontroller, which subsequently supplies 4.8 V to a Lithium Polymer (LiPo) battery characterized by a nominal voltage of 4.7 V (Fig. 97).

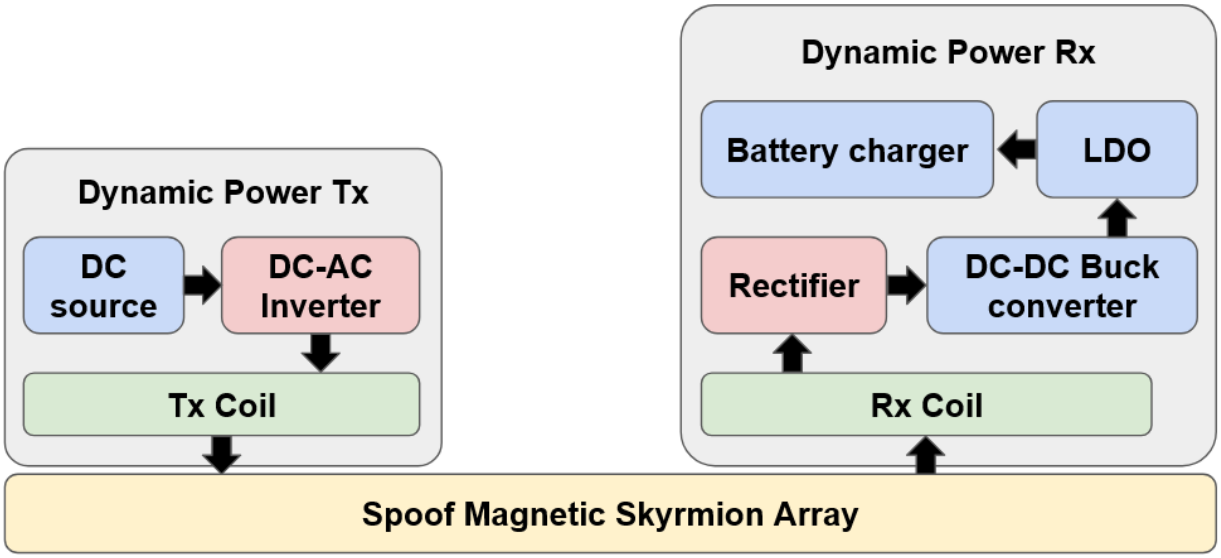

Fig. 97. The mini-EV power delivery network.

To assess the functionality of the power delivery network, a comprehensive testing procedure was executed. Firstly, the power components were integrated, and the power flow through the network was intentionally halted while the mini-EV remained disengaged from drawing any load current. Following this, the DC motors were activated, simulating load current draw, in the absence of active power injection into the network. During this phase, diligent monitoring of the state of charge of the onboard miniature battery was carried out.

4.4.4. Mini Electrical Vehicle Test

The high-level mini-EV hardware system is compromised of a microcontroller unit that is digitally communicating with a BLE and an NFC module. The NFC module is connected to a receiver coil through a bandpass filter in order to protect the NFC circuitry from high-power WPT signal. In addition, the MCU communicates with a battery gauge sensor that continuously measures the state of charge in the on-board miniature battery. And as soon as the battery charge drops from a certain desired level, it will enable a battery charger regulator that is itself communicating to the MCU on the I2C bus. The power delivery network here takes care of the power transmission from the active source through the SMS structure to the mini-EV. We used a pair of miniature DC motors as loads to this mini-EV. The microcontroller can switch these DC motors on or off through a dedicated relay (Fig. 98).

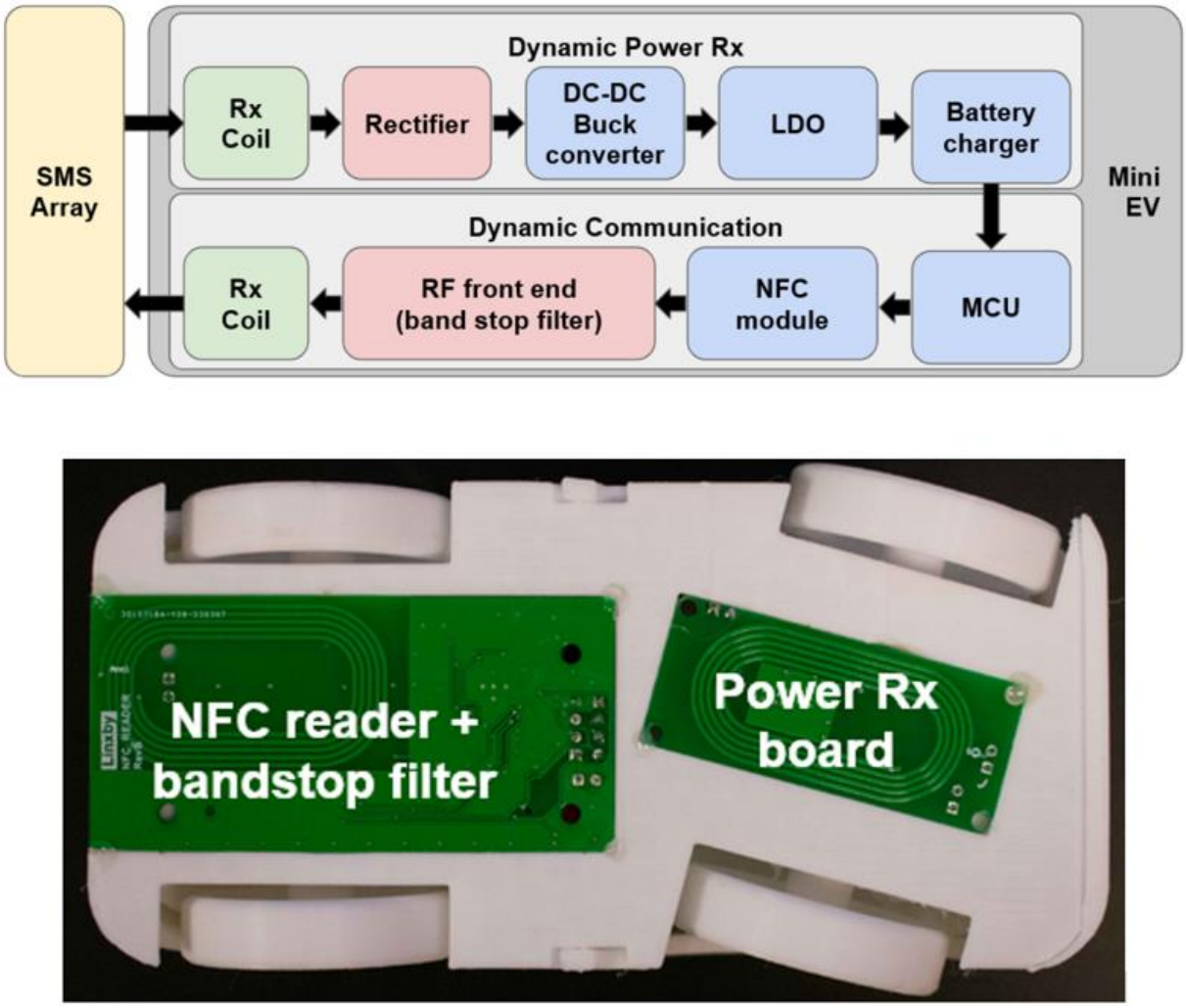

Fig. 98. The high-level mini-EV hardware system.

To assess the performance of the power delivery network, we conducted a series of tests and observations. Initially, we integrated the power components and halted the power flow throughout the network while the mini-EV remained inactive, drawing no load current. Subsequently, we activated the DC motors to draw load current without injecting active power into the network. During this phase, we closely monitored the state of charge of the onboard miniature battery placed on a circular track (Fig. 99).

Fig. 99. Mini-EV 410cm-long circular track.

This circular track (along with a smaller track with 220cm-long path) demonstrated two passbands at WPT and NFC bands (Fig. 100).

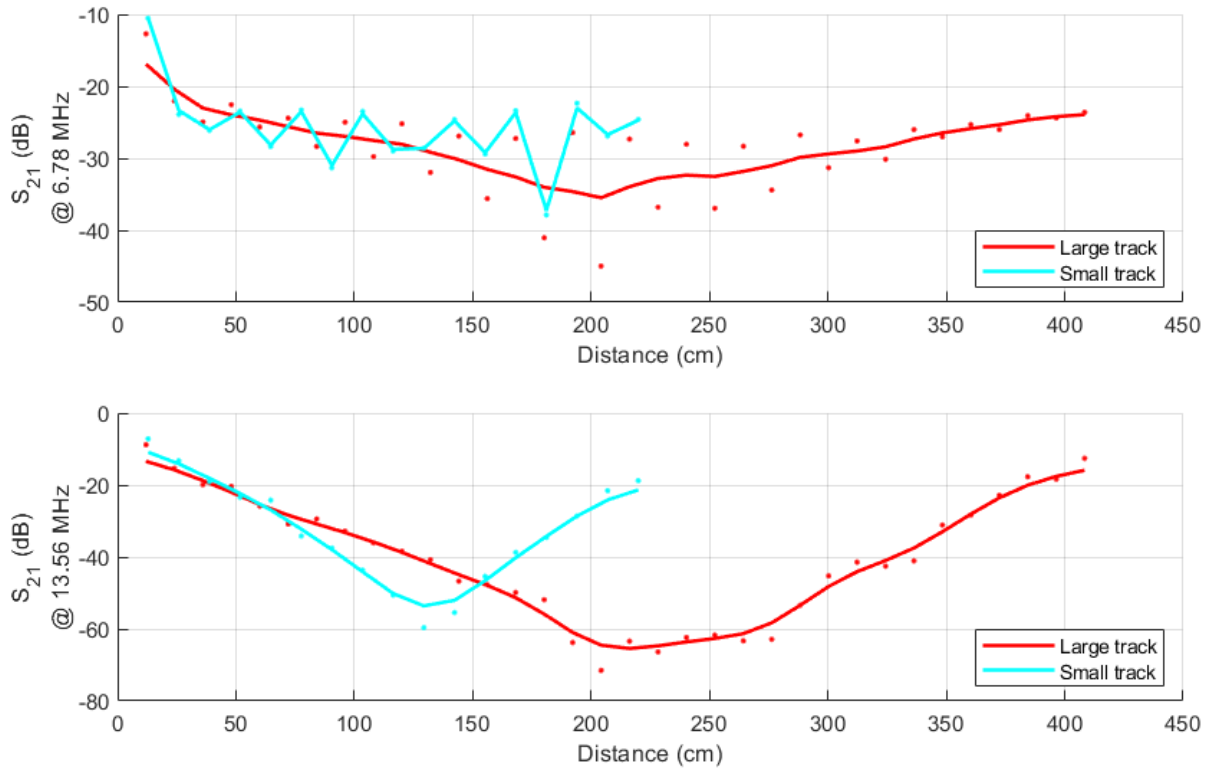

Fig. 100. Transmission profile of circular loops.

Following this, we initiated the power transmitter (a 6.78MHz Class EF power inverter) to inject power through the network. Our observations revealed that the state of charge remained relatively stable. This stability was attributed to the balance between the load's withdrawal from the battery and the charge received by the battery from the network. In the subsequent phase, we deactivated the DC motors, eliminating any current draw from the battery while maintaining power transmission. During this period, we observed a noticeable increase in the state of charge within the battery. This highlights the network's ability to replenish the battery's charge in the absence of load current, underscoring its efficiency in managing power distribution and storage.

These experimental phases collectively contributed to a comprehensive validation of the power delivery network's dynamics, elucidating its capacity to regulate and maintain the state of charge of the onboard battery amidst varying operational scenarios (Fig. 101).

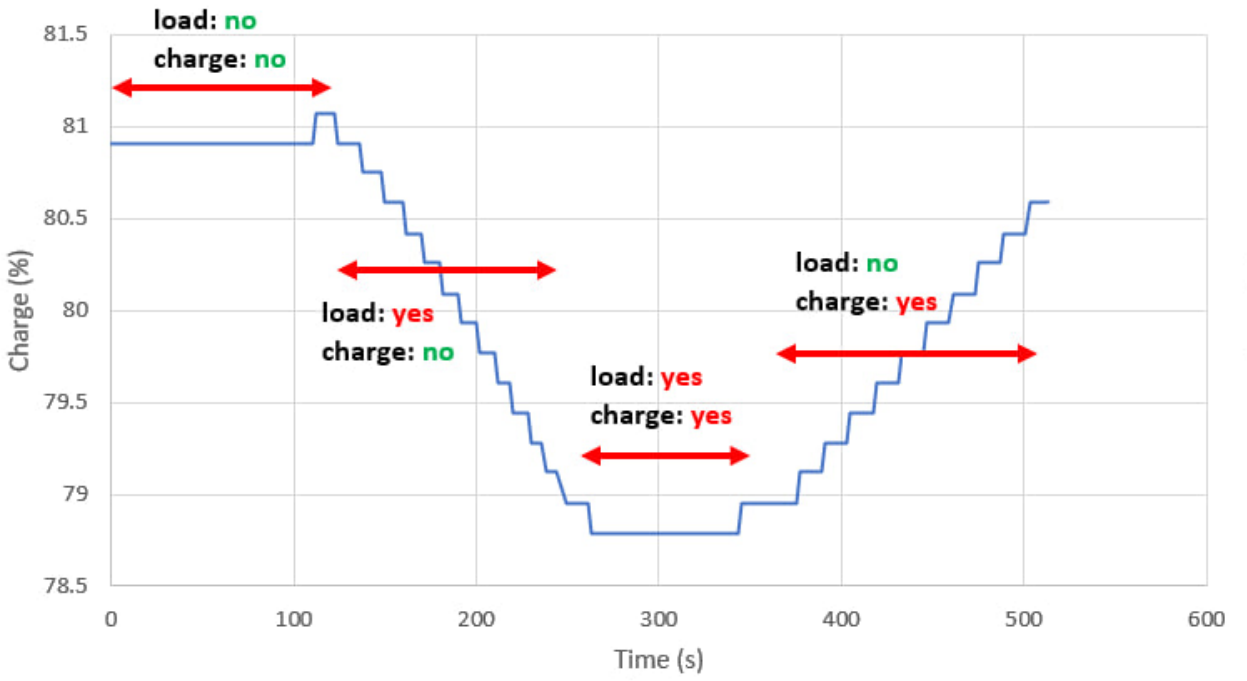

Fig. 101. The mini-EV state of charge under load/no-load and enabled/disabled charging.

4.4.5. Potential Application in Autonomous Steering

The concept of employing power charging roads for miniature robotics, exemplified by the Mini EV showcased in this project, holds promise for diverse applications. Beyond its current use case, this concept presents potential for other practical implementations. A notable example involves the potential for relatively detecting the Mini EV's spatial positioning with respect to the power charging lane. This can be accomplished through the utilization of a pair of specialized coils, referred to as sniffer coils. These coils generate a differential signal, which can be effectively correlated to the extent of misalignment existing between the Mini EV's center and the central axis of the SMS road. This approach opens avenues for enhanced precision in location detection and alignment assessment, broadening the utility and versatility of the proposed power charging road concept (Fig. 102).

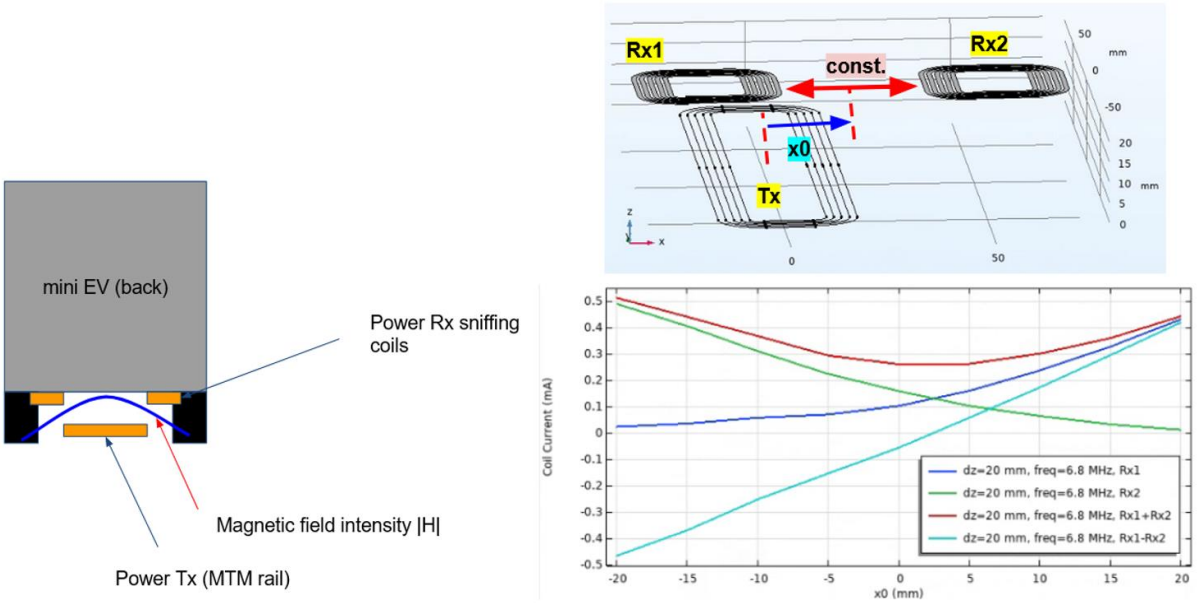

Fig. 102. Potential autonomous mini-EV steering applications.

4.4.6. Communication Between Active NFC Readers

The NFC communication protocol inherently facilitates the linkage between an active master NFC controller and one or more passive NFC-enabled tags. These tags can effectively convey information pertaining to the state of charge. However, given scenarios where multiple mini-EVs might simultaneously operate on the road, the necessity arises for establishing a handshake mechanism amongst several active readers, all within the framework of the NFC protocol.

To address this, a passive NFC-enabled tag is seamlessly integrated within each individual mini-EV. This tag assumes the role of an intermediary, facilitating communication between two distinct active NFC readers. Through this architecture, pivotal information, such as the state of charge for each mini-EV, is securely stored within the appropriate register of this passive tag. Subsequently, this information can be accessed via the active NFC reader situated on the power transmitter side.

Alternatively, supplementary communication methods such as BLE, cellular networks, or Wi-Fi can be leveraged for transmitting state-of-charge data to the power transmitter. An intrinsic facet of this communication network involves its potential for power receiver authorization. By harnessing passive NFC tags, this authorization mechanism can be actively employed, granting power receivers access to available power resources.

Moreover, the deployment of passive NFC tags affords the capacity to regulate power flow via NFC switches, a cornerstone aspect of the project's design. This inclusive approach serves to enhance the overall management and functionality of the power delivery network, while effectively accommodating the nuanced demands posed by multiple mini-EVs operating concurrently (Fig. 103).

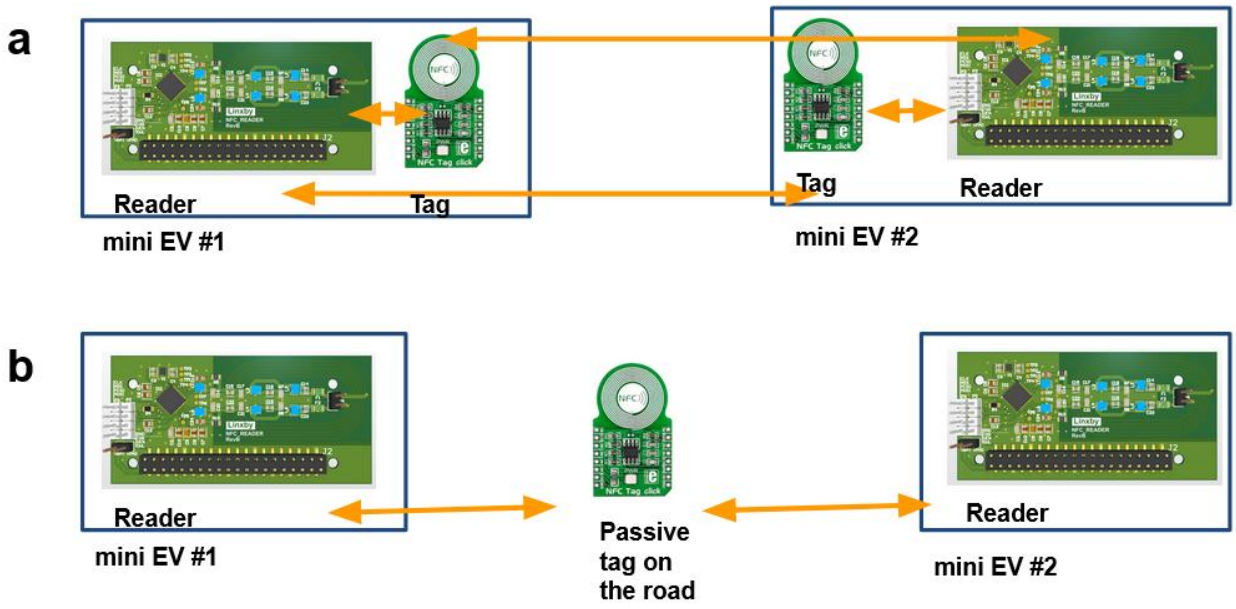

Fig. 103. Indirect NFC reader communication scenarios.

4.4.7. Passband Compatibility with Qi Protocol

The significant bandgap here between the NFC (13.56 MHz) and Qi band (100-150 kHz) results in a near zero unbalancing factor, which is impractical. Alternatively, this multi-band MI array can be realized through nested resonators each tuned separately at the corresponding band (Fig. 104).

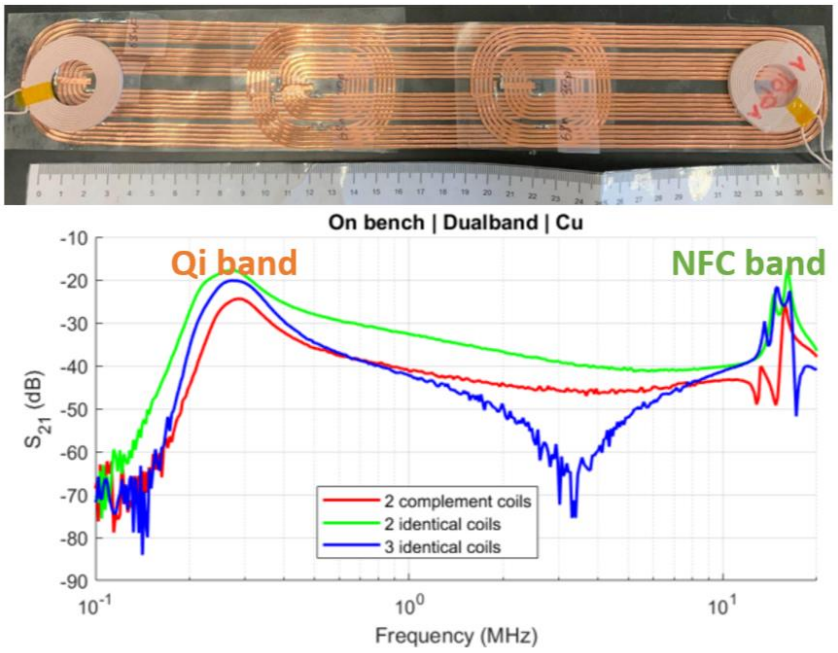

Fig. 104. Potential nested coil geometries for SMS dualband performance with large bandgap.

5. REFERENCES

[1] M. R. Yuce, “Wearable sensors get connected with plasmons,” *Nat. Electron.*, vol. 2, no. 6, pp. 217–218, 2019, doi: 10.1038/s41928-019-0265-7.

[2] J. Kim, A. S. Campbell, B. E. F. de Ávila, and J. Wang, “Wearable biosensors for healthcare monitoring,” *Nat. Biotechnol.*, vol. 37, no. April, 2019, doi: 10.1038/s41587-019-0045-y.

[3] M. R. Yuce, “Implementation of wireless body area networks for healthcare systems,” *Sensors Actuators, A Phys.*, vol. 162, no. 1, pp. 116–129, 2010, doi: 10.1016/j.sna.2010.06.004.

[4] H. Kim, H. Hirayama, S. Kim, R. Zhang, and J. Choi, “Review of near-field wireless power and communication for biomedical applications,” *IEEE Access*, vol. 5, pp. 21264–21285, 2017.

[5] A. Ghosh, A. Halder, and A. S. Dhar, “A Variable RF Carrier Modulation Scheme for Ultralow Power Wireless Body-Area Network,” *IEEE Syst. J.*, vol. 6, no. 2, pp. 305–316, 2012.

[6] S. Niu *et al.*, “A wireless body area sensor network based on stretchable passive tags,” *Nat. Electron.*, vol. 2, no. 8, pp. 361–368, 2019, doi: 10.1038/s41928-019-0286-2.

[7] T. Wu, F. Wu, J. M. Redoute, and M. R. Yuce, “An Autonomous Wireless Body Area Network Implementation Towards IoT Connected Healthcare Applications,” *IEEE Access*, vol. 5, pp. 11413–11422, 2017, doi: 10.1109/ACCESS.2017.2716344.

[8] X. Tian *et al.*, “Wireless body sensor networks based on metamaterial textiles,” *Nat. Electron.*, vol. 2, no. 6, pp. 243–251, 2019, doi: 10.1038/s41928-019-0257-7.

[9] E. Jovanov and A. Milenkovic, “Body area networks for ubiquitous healthcare applications: Opportunities and challenges,” *J. Med. Syst.*, vol. 35, no. 5, pp. 1245–1254, 2011, doi: 10.1007/s10916-011-9661-x.

[10] J. R. Sempionatto *et al.*, “An epidermal patch for the simultaneous monitoring of haemodynamic and metabolic biomarkers,” *Nat. Biomed. Eng.*, vol. 5, no. 7, pp. 737–748, 2021, doi: 10.1038/s41551-021-00685-1.

[11] N. Golestani and M. Moghaddam, “Human activity recognition using magnetic induction-based motion signals and deep recurrent neural networks,” *Nat.*

Commun., vol. 11, no. 1, 2020, doi: 10.1038/s41467-020-15086-2.

[12] A. Al-Ali, E. K. Kinast, and B. Muhsin, “Medical monitoring hub, US Patent US9436645B2,” US9436645B2, 2018.

[13] M. C. Domingo, “Overview of channel models for underwater wireless communication networks,” *Phys. Commun.*, 2008.

[14] Z. Zheng, Y. Fu, K. Liu, R. Xiao, X. Wang, and H. Shi, “Three-stage vertical distribution of seawater conductivity,” *Sci. Rep.*, vol. 8, no. 1, 2018, doi: 10.1038/s41598-018-27931-y.

[15] M. A. Bin Yusof and S. Kabir, “An overview of sonar and electromagnetic waves for underwater communication,” *IETE Tech. Rev. (Institution Electron. Telecommun. Eng. India)*, vol. 29, no. 4, pp. 307–317, 2012, doi: 10.4103/0256-4602.101312.

[16] C. M. G. Gussen, P. S. R. Diniz, M. L. R. Campos, W. A. Martins, F. M. Costa, and J. N. Gois, “A Survey of Underwater Wireless Communication Technologies,” *J. Commun. Inf. Syst.*, vol. 31, no. 1, p. 242, 2016.

[17] M. C. Domingo, “Securing Underwater Wireless Communication Networks,” *IEEE Wirel. Commun.*, vol. 18, no. 1, pp. 22–28, doi: 10.14419/ijet.v7i2.23.15344.

[18] S. A. Mohammad Furqan Ali, Dushantha Nalin K. Jayakody, Yury Alexandrovich Chursin and S. Dmitry, *Recent Advances and Future Directions on Underwater Wireless Communications*, vol. 27, no. 5. Springer Netherlands, 2020.

[19] X. Tian, X. Yang, and J. S. Ho, “Energy-efficient and Secure Wireless Body Sensor Networks with Metamaterial Textiles,” *BioCAS 2019 - Biomed. Circuits Syst. Conf. Proc.*, pp. 38–41, 2019, doi: 10.1109/BIOCAS.2019.8919179.

[20] Q. D. La, D. Nguyen-nam, M. V Ngo, S. Member, H. T. Hoang, and T. Q. S. Quek, “Dense Deployment of BLE-Based Body Area Networks : A Coexistence Study,” *IEEE Trans. GREEN Commun. Netw.*, vol. 2, no. 4, pp. 972–981, 2018.

[21] A. Kianinejad, Z. N. Chen, and C. Qiu, “Low-Loss Spoof Surface Plasmon Slow-Wave Transmission Lines With Compact Transition and High Isolation,” *IEEE Trans. Microw. Theory Tech.*, vol. 64, no. 10, pp. 3078–3086, 2016.

[22] K. Pan *et al.*, “Sustainable production of highly conductive multilayer graphene ink for wireless connectivity and IoT applications,” *Nat. Commun.*, vol. 9, no. 1, 2018, doi: 10.1038/s41467-018-07632-w.

[23] Y. Mou *et al.*, “Facile preparation of stable reactive silver ink for highly conductive and flexible electrodes,” *Appl. Surf. Sci.*, vol. 475, pp. 75–82, 2019, doi: 10.1016/j.apsusc.2018.12.261.

[24] Y. Dong *et al.*, “Optimizing formulations of silver organic decomposition ink for producing highly-conductive features on flexible substrates: The case study of amines,” *Thin Solid Films*, vol. 616, pp. 635–642, 2016, doi: 10.1016/j.tsf.2016.09.024.

[25] L. Gamba *et al.*, “Systematic Design of a Graphene Ink Formulation for Aerosol Jet Printing,” *ACS Appl. Mater. Interfaces*, 2022, doi: 10.1021/acsami.2c18838.

[26] Q. Duan, B. Lan, and Y. Lv, “Highly Dispersed, Adhesive Carbon Nanotube Ink for Strain and Pressure Sensors,” *ACS Appl. Mater. Interfaces*, vol. 14, no. 1, pp. 1973–1982, 2022, doi: 10.1021/acsami.1c20133.

[27] Y. Rosen, R. Marrach, V. Gutkin, and S. Magdassi, “Thin Copper Flakes for Conductive Inks Prepared by Decomposition of Copper Formate and Ultrafine Wet Milling,” *Adv. Mater. Technol.*, vol. 4, no. 1, 2019, doi: 10.1002/admt.201800426.

[28] J. Kim, Z. Wang, and W. S. Kim, “Stretchable RFID for wireless strain sensing with silver nano ink,” *IEEE Sens. J.*, vol. 14, no. 12, pp. 4395–4401, 2014, doi: 10.1109/JSEN.2014.2335743.

[29] A. Chrysler, C. Furse, and Y. Chung, “Biocompatible, implantable UHF RFID antenna made from conductive ink,” *2016 IEEE Antennas Propag. Soc. Int. Symp. APSURSI 2016 - Proc.*, pp. 467–468, 2016, doi: 10.1109/APS.2016.7695942.

[30] X. Wang *et al.*, “Printed Conformable Liquid Metal e-Skin-Enabled Spatiotemporally Controlled Bioelectromagnetics for Wireless Multisite Tumor Therapy,” *Adv. Funct. Mater.*, vol. 29, no. 51, pp. 1–13, 2019, doi: 10.1002/adfm.201907063.

[31] V. Le, P. Moser, U. Lemmer, and E. MacKensen, “A comparison of printed flexible RFID/NFC antennas for a microelectronic measurement system,” *2019 IEEE Int. Conf. RFID Technol. Appl. RFID-TA 2019*, pp. 49–54, 2019, doi: 10.1109/RFID-TA.2019.8892040.

[32] A. A. Mohammed, “Development of a New Stretchable and Screen Printable Conductive Ink,” 2017.

[33] R. Lin *et al.*, “Wireless battery-free body sensor networks using near-field-enabled clothing,” *Nat. Commun.*, vol. 11, no. 1, pp. 1–10, 2020, doi: 10.1038/s41467-020-14311-2.

[34] M. Dautta, A. Jimenez, K. K. H. Dia, N. Rashid, M. A. Al Faruque, and P. Tseng, “Wireless Qi-powered, Multinodal and Multisensory Body Area Network for Mobile Health,” *IEEE Internet Things J.*, 2020, doi: 10.1109/JIOT.2020.3040713.

[35] L. Xu *et al.*, “Characterization and Modeling of Embroidered NFC Coil Antennas for Wearable Applications,” *IEEE Sens. J.*, vol. XX, no. XX, pp. 1–1, 2020, doi:

10.1109/jsen.2020.3008594.

[36] Y. Masuda, A. Noda, and H. Shinoda, “Body Sensor Networks Powered by an NFC-Coupled Smartphone in the Pocket,” *Conf. Proc. ... Annu. Int. Conf. IEEE Eng. Med. Biol. Soc. IEEE Eng. Med. Biol. Soc. Annu. Conf.*, vol. 2018, pp. 5394–5397, 2018, doi: 10.1109/EMBC.2018.8513567.

[37] V. Mishra and A. Kiourti, “Wearable Magnetoinductive Waveguide for Low-Loss Wireless Body Area Networks,” *IEEE Trans. Antennas Propag.*, vol. 69, no. 5, pp. 2864–2876, 2021, doi: 10.1109/TAP.2020.3030987.

[38] P. S. W Huang, “NFC antenna for wearable application,” US Patent 9,998,182, 2018.

[39] F. Koshiji, Y. Fujita, and K. Koshiji, “Wireless body area network using magnetically-coupled wearable coils,” *IEEE CPMT Symp. Japan 2015 Packag. is Everywhere, ICSJ 2015*, pp. 208–211, 2015, doi: 10.1109/ICSJ.2015.7357399.

[40] D. Das, S. Maity, B. Chatterjee, and S. Sen, *Enabling Covert Body Area Network using Electro-Quasistatic Human Body Communication*, vol. 9, no. 1. Springer US, 2019.

[41] S. Gong *et al.*, “A wearable and highly sensitive pressure sensor with ultrathin gold nanowires,” *Nat. Commun.*, vol. 5, 2014, doi: 10.1038/ncomms4132.

[42] X. Xiao, J. Yin, G. Chen, S. Shen, A. Nashalian, and J. Chen, “Bioinspired acoustic textiles with nanoscale vibrations for wearable biomonitoring,” *Matter*, vol. 5, no. 5, pp. 1342–1345, 2022, doi: 10.1016/j.matt.2022.03.014.

[43] Z. Lin *et al.*, “A Personalized Acoustic Interface for Wearable Human–Machine Interaction,” *Adv. Funct. Mater.*, vol. 32, no. 9, 2022, doi: 10.1002/adfm.202109430.

[44] B. Bube, H. Klocke, A. M. Lara-Palma, and B. B. Zanon, “Wearable Freedive Computer with Acoustic Communication,” *IEEE Consum. Electron. Mag.*, vol. 11, no. 5, pp. 94–100, 2022, doi: 10.1109/MCE.2021.3096795.

[45] P. P. Mercier and A. P. Chandrakasan, *Ultra-Low-Power Short-Range Radios*. 2015.

[46] K. Weise, M. Ziolkowski, M. Carlstedt, H. Brauer, and H. Toepfer, “Oscillatory Motion of Permanent Magnets above a Conducting Slab,” *IEEE Trans. Magn.*, vol. 51, no. 10, 2015, doi: 10.1109/TMAG.2015.2448519.

[47] L. Yin *et al.*, “A self-sustainable wearable multi-modular E-textile bioenergy microgrid system,” *Nat. Commun.*, vol. 12, no. 1, pp. 1–12, 2021, doi: 10.1038/s41467-021-21701-7.

[48] L. Yin *et al.*, “A stretchable epidermal sweat sensing platform with an integrated printed battery and electrochromic display,” *Nat. Electron.*, vol. 5, no. 10, pp. 694–705, 2022, doi: 10.1038/s41928-022-00843-6.

[49] A. J. Bandodkar *et al.*, “Sweat-activated biocompatible batteries for epidermal electronic and microfluidic systems,” *Nat. Electron.*, vol. 3, no. 9, pp. 554–562, 2020, doi: 10.1038/s41928-020-0443-7.

[50] Y. Song *et al.*, “Wireless battery-free wearable sweat sensor powered by human motion,” *Sci. Adv.*, vol. 6, no. 40, pp. 1–11, 2020, doi: 10.1126/sciadv.aay9842.

[51] J. Gummeson, “A body area power network,” *Nat. Electron.*, vol. 4, no. 7, pp. 462–463, 2021, doi: 10.1038/s41928-021-00617-6.

[52] J. Li, Y. Dong, J. H. Park, and J. Yoo, “Body-coupled power transmission and energy harvesting,” *Nat. Electron.*, vol. 4, no. 7, pp. 530–538, 2021, doi: 10.1038/s41928-021-00592-y.

[53] Y. Zhang *et al.*, “High precision epidermal radio frequency antenna via nanofiber network for wireless stretchable multifunction electronics,” *Nat. Commun.*, vol. 11, no. 1, pp. 1–10, 2020, doi: 10.1038/s41467-020-19367-8.

[54] R. Lin *et al.*, “Digitally-embroidered liquid metal electronic textiles for wearable wireless systems,” *Nat. Commun.*, vol. 13, no. 1, pp. 1–10, 2022, doi: 10.1038/s41467-022-29859-4.

[55] A. Hajiaghajani, A. H. Afandizadeh Zargari, M. Dautta, A. Jimenez, F. Kurdahi, and P. Tseng, “Textile-integrated metamaterials for near-field multibody area networks,” *Nat. Electron.*, vol. 4, no. 11, pp. 808–817, 2021, doi: 10.1038/s41928-021-00663-0.

[56] J. H. Koo *et al.*, “A vacuum-deposited polymer dielectric for wafer-scale stretchable electronics,” vol. 6, no. February, pp. 137–145, 2023, doi: 10.1038/s41928-023-00918-y.

[57] Y. Ohm, C. Pan, M. J. Ford, X. Huang, J. Liao, and C. Majidi, “An electrically conductive silver-polyacrylamide-alginate hydrogel composite for soft electronics,” *Nat. Electron.*, vol. 4, no. March, 2021, doi: 10.1038/s41928-021-00545-5.

[58] F. Olenik, S., Lee, H.S. & Güder, “The future of near-field communication-based wireless sensing,” *Nat. Rev. Mater.*, 2021, doi: 10.1038/s41578-021-00299-8.

[59] G. Atanasova and N. Atanasov, “Small antennas for wearable sensor networks: Impact of the electromagnetic properties of the textiles on antenna performance,” *Sensors (Switzerland)*, vol. 20, no. 18, pp. 1–21, 2020, doi: 10.3390/s20185157.

[60] A. Taparugssanagorn, C. Pomalaza-Ráez, R. Tesi, M. Hamalainen, and J. Iinatti, “Effect of body motion and the type of antenna on the measured UWB channel characteristics in medical applications of wireless body area networks,” *Proc. - 2009 IEEE Int. Conf. Ultra-Wideband, ICUWB 2009*, vol. 2009, pp. 332–336, 2009, doi: 10.1109/ICUWB.2009.5288764.

[61] G. Fortino, R. Giannantonio, R. Gravina, P. Kuryloski, and R. Jafari, “Enabling effective programming and flexible management of efficient body sensor network applications,” *IEEE Trans. Human-Machine Syst.*, vol. 43, no. 1, pp. 115–133, 2013, doi: 10.1109/TSMCC.2012.2215852.

[62] R. Gravina, P. Alinia, H. Ghasemzadeh, and G. Fortino, “Multi-sensor fusion in body sensor networks: State-of-the-art and research challenges,” *Inf. Fusion*, vol. 35, pp. 1339–1351, 2017, doi: 10.1016/j.inffus.2016.09.005.

[63] F. Arab Hassani *et al.*, “Smart materials for smart healthcare– moving from sensors and actuators to self-sustained nanoenergy nanosystems,” *Smart Mater. Med.*, vol. 1, no. June, pp. 92–124, 2020, doi: 10.1016/j.smaim.2020.07.005.

[64] W. Zhong, C. K. Lee, and S. Y. Ron Hui, “General analysis on the use of tesla’s resonators in domino forms for wireless power transfer,” *IEEE Trans. Ind. Electron.*, vol. 60, no. 1, pp. 261–270, 2013, doi: 10.1109/TIE.2011.2171176.

[65] B. Wang, W. Yerazunis, and K. H. Teo, “Wireless power transfer: Metamaterials and array of coupled resonators,” *Proc. IEEE*, vol. 101, no. 6, pp. 1359–1368, 2013, doi: 10.1109/JPROC.2013.2245611.

[66] C. J. Stevens, C. W. T. Chan, K. Stamatis, and D. J. Edwards, “Magnetic metamaterials as 1-D data transfer channels: An application for magneto-inductive waves,” *IEEE Trans. Microw. Theory Tech.*, vol. 58, no. 5 PART 1, pp. 1248–1256, 2010, doi: 10.1109/TMTT.2010.2045562.

[67] E. S. Laszlo Solymar, *Waves in Metamaterials*. OUP Oxford, 2009.

[68] O. Sydoruk, O. Zhuromskyy, E. Shamonina, and L. Solymar, “Phonon-like dispersion curves of magnetoinductive waves,” *Appl. Phys. Lett.*, vol. 87, no. 7, pp. 4–6, 2005, doi: 10.1063/1.2011789.

[69] R. R. A. Syms, E. Shamonina, V. Kalinin, and L. Solymar, “A theory of metamaterials based on periodically loaded transmission lines: Interaction between magnetoinductive and electromagnetic waves,” *J. Appl. Phys.*, vol. 97, no. 6, pp. 1–6, 2005, doi: 10.1063/1.1850182.

[70] Z. Xu, J. Shi, R. J. Davis, X. Yin, and D. F. Sievenpiper, “Rainbow trapping with long oscillation lifetimes in gradient magnetoinductive metasurfaces,” *Phys. Rev. Appl.*, vol. 12, no. 2, p. 1, 2019, doi: 10.1103/PhysRevApplied.12.024043.

[71] C. J. Stevens, “Magnetoinductive waves and wireless power transfer,” *IEEE Trans. Power Electron.*, vol. 30, no. 11, pp. 6182–6190, 2015, doi: 10.1109/TPEL.2014.2369811.

[72] S. D. Huang, Z. Q. Li, and Y. Li, “Transfer efficiency analysis of magnetic resonance wireless power transfer with intermediate resonant coil,” *J. Appl. Phys.*, vol. 115, no. 17, 2014, doi: 10.1063/1.4867125.

[73] F. Zhang, S. A. Hackworth, W. Fu, C. Li, Z. Mao, and M. Sun, “Relay effect of wireless power transfer using strongly coupled magnetic resonances,” *IEEE Trans. Magn.*, vol. 47, no. 5, pp. 1478–1481, 2011, doi: 10.1109/TMAG.2010.2087010.

[74] W. X. Zhong, C. K. Lee, and S. Y. R. Hui, “Wireless power domino-resonator systems with noncoaxial axes and circular structures,” *IEEE Trans. Power Electron.*, vol. 27, no. 11, pp. 4750–4762, 2012, doi: 10.1109/TPEL.2011.2174655.

[75] G. Puccetti, U. Reggiani, and L. Sandrolini, “Experimental analysis of wireless power transmission with spiral resonators,” *Energies*, vol. 6, no. 11, pp. 5887–5896, 2013, doi: 10.3390/en6115887.

[76] E. Shamonina, V. A. Kalinin, K. H. Ringhofer, and L. Solymar, “Magnetoinductive waves in one, two, three dimensions,” *J. Appl. Phys.*, vol. 92, no. 10, pp. 6252–6261, 2002, doi: 10.1063/1.1510945.

[77] C. P. Yue and S. S. Wong, “On-chip spiral inductors with patterned ground shields for si-based RF IC’s,” *Phase-Locking High-Performance Syst. From Devices to Archit.*, vol. 33, no. 5, pp. 118–126, 2003, doi: 10.1109/9780470545492.ch12.

[78] K. Aslanidis and V. Needhan Gunasegaran, “TRF7970A NFC Reader Antenna Multiplexing,” 2016.

[79] J. Wyatt, “TRF7960A RFID Multiplexer Example System,” 2012.

[80] F. Ershad *et al.*, “Ultra-conformal drawn-on-skin electronics for multifunctional motion artifact-free sensing and point-of-care treatment,” *Nat. Commun.*, vol. 11, no. 1, 2020, doi: 10.1038/s41467-020-17619-1.

[81] L. Lin, M. Dautta, A. Hajiaghajani, A. R. Escobar, P. Tseng, and M. Khine, “Paint-On Epidermal Electronics for On-Demand Sensors and Circuits,” *Adv. Electron. Mater.*, vol. 2000765, pp. 1–8, 2020, doi: 10.1002/aelm.202000765.

[82] R. R. A. Syms, E. Shamonina, and L. Solymar, “Magneto-inductive waveguide devices,” *IEE Proc. Microwaves, Antennas Propag.*, vol. 153, no. 2, pp. 111–121, 2006, doi: 10.1049/ip-map:20050119.

[83] M. C. K. Wiltshire, E. Solymar, I. R. Shamonina, and L. Young, “Dispersion

characteristics of magneto-inductive waves: comparison between theory and experiment," *Electron. Lett.*, vol. 39, no. 2, pp. 215–217, 2005, doi: 10.1049/el.

[84] C. Caloz and T. Itoh, *Electromagnetic Metamaterials: Transmission Line Theory and Microwave Applications: The Engineering Approach*. 2005.

[85] C. A. Balanis, *Antenna Theory: Analysis and Design*. John Wiley & Sons, 2012.

[86] A. Boumeganane, A. Nadi, O. Cherkaoui, and M. Tahiri, "Inkjet printing of silver conductive ink on textiles for wearable electronic applications," *Mater. Today Proc.*, vol. 58, pp. 1235–1241, 2022, doi: 10.1016/j.matpr.2022.01.469.

[87] L. Mo *et al.*, "Nano-Silver Ink of High Conductivity and Low Sintering Temperature for Paper Electronics," *Nanoscale Res. Lett.*, vol. 14, 2019, doi: 10.1186/s11671-019-3011-1.

[88] W. Zu, Y. Ohm, M. R. Carneiro, M. Vinciguerra, M. Tavakoli, and C. Majidi, "A Comparative Study of Silver Microflakes in Digitally Printable Liquid Metal Embedded Elastomer Inks for Stretchable Electronics," *Adv. Mater. Technol.*, vol. 7, no. 12, 2022, doi: 10.1002/admt.202200534.

[89] M. Tavakoli *et al.*, "EGaIn-Assisted Room-Temperature Sintering of Silver Nanoparticles for Stretchable, Inkjet-Printed, Thin-Film Electronics," *Adv. Mater.*, vol. 30, no. 29, 2018, doi: 10.1002/adma.201801852.

[90] S. Cheng, C. M. Huang, and M. Pecht, "A review of lead-free solders for electronics applications," *Microelectron. Reliab.*, vol. 75, pp. 77–95, 2017, doi: 10.1016/j.microrel.2017.06.016.

[91] Y. Liu, J. Hao, X. Zheng, C. Shi, and H. Yang, "Screen printing of stretchable silver nanomaterial inks for a stable human-machine interface," *J. Mater. Chem. C*, vol. 11, no. 15, pp. 5009–5017, 2023, doi: 10.1039/d3tc00388d.

[92] Y. Z. N. Htwe and M. Mariatti, "Printed graphene and hybrid conductive inks for flexible, stretchable, and wearable electronics: Progress, opportunities, and challenges," *J. Sci. Adv. Mater. Devices*, vol. 7, no. 2, 2022, doi: 10.1016/j.jsamd.2022.100435.

[93] IEEE-SA Standards Board, "IEEE Standard for Safety Levels With Respect to Human Exposure to Radio Frequency Electromagnetic Fields, 3 kHz to 300 GHz," *IEEE Std C95.1-2005*, 2005, doi: 10.1109/IEEESTD.2006.99501.

[94] M. Rapin, J. Wacker, and O. Chételat, "Two-wire bus combining full duplex body-sensor network and multilead biopotential measurements," *IEEE Trans. Biomed. Eng.*, vol. 65, no. 1, pp. 113–122, 2018, doi: 10.1109/TBME.2017.2696051.

[95] N. Cho, J. Yoo, S. J. Song, J. Lee, S. Jeon, and H. J. Yoo, “The human body characteristics as a signal transmission medium for intrabody communication,” *IEEE Trans. Microw. Theory Tech.*, vol. 55, no. 5, pp. 1080–1085, 2007, doi: 10.1109/TMTT.2007.895640.

[96] E. Wen, D. Sievenpiper, and P. Mercier, “Channel Characterization of Magnetic Human Body Communication,” *IEEE Trans. Biomed. Eng.*, vol. 69, no. 2, pp. 569–579, 2022, doi: 10.1109/TBME.2021.3101766.

[97] Y. Khan, A. E. Ostfeld, C. M. Lochner, A. Pierre, A. C. Arias, and and A. C. A. Yasser Khan , Aminy E. Ostfeld , Claire M. Lochner , Adrien Pierre, “Monitoring of Vital Signs with Flexible and Wearable Medical Devices,” *Adv. Mater.*, vol. 28, no. 22, pp. 4373–4395, 2016, doi: 10.1002/adma.201504366.

[98] N. Nagaosa and Y. Tokura, “Topological properties and dynamics of magnetic skyrmions,” *Nat. Nanotechnol.*, vol. 8, no. 12, pp. 899–911, 2013, doi: 10.1038/nnano.2013.243.

[99] A. Casiraghi *et al.*, “Individual skyrmion manipulation by local magnetic field gradients,” *Commun. Phys.*, vol. 2, no. 1, pp. 1–9, 2019, doi: 10.1038/s42005-019-0242-5.

[100] Y. Guang *et al.*, “Creating zero-field skyrmions in exchange-biased multilayers through X-ray illumination,” *Nat. Commun.*, vol. 11, no. 1, pp. 1–6, 2020, doi: 10.1038/s41467-020-14769-0.

[101] D. Wolf *et al.*, “Unveiling the three-dimensional magnetic texture of skyrmion tubes,” *Nat. Nanotechnol.*, vol. 17, no. 3, pp. 250–255, 2022, doi: 10.1038/s41565-021-01031-x.

[102] L. Du, A. Yang, A. V Zayats, and X. Yuan, “Deep-subwavelength features of photonic skyrmions in a confined electromagnetic field with orbital angular momentum,” *Nature Physics*, vol. 15, no. 7. Springer US, pp. 650–654, 2019, doi: 10.1038/s41567-019-0487-7.

[103] Y. Miyazaki, T. Yokouchi, and Y. Shiomi, “Trapping and manipulating skyrmions in two-dimensional films by surface acoustic waves,” *Sci. Rep.*, vol. 13, no. 1, pp. 1–9, 2023, doi: 10.1038/s41598-023-29022-z.

[104] X. R. Wang, X. C. Hu, and H. T. Wu, “Stripe skyrmions and skyrmion crystals,” *Commun. Phys.*, vol. 4, no. 1, pp. 1–7, 2021, doi: 10.1038/s42005-021-00646-9.

[105] T. Yokouchi *et al.*, “Creation of magnetic skyrmions by surface acoustic waves,” *Nat. Nanotechnol.*, vol. 15, no. 5, pp. 361–366, 2020, doi: 10.1038/s41565-020-0661-1.

[106] S. Li, X. Wang, and T. Rasing, “Magnetic skyrmions: Basic properties and potential applications,” *Interdiscip. Mater.*, vol. 2, no. 2, pp. 260–289, 2023, doi: 10.1002/idm2.12072.